



A11107 226762

NIST
PUBLICATIONS**NIST****National Institute of
Standards and Technology**
U.S. Department of Commerce***NIST Technical Note 1558*****An Electromagnetic Evaluation of the
NASA Space Power Facility at
Plum Brook Station**

Galen Koepke
John Ladbury
Dennis Camell
Jason Coder
Chriss Hammerschmidt
Randall Direeen
Jeff Guerrieri

QC
100
.U5753
NO.1558
2011

NIST Technical Note 1558

**An Electromagnetic Evaluation of the NASA
Space Power Facility at Plum Brook Station**

Galen Koepke
John Ladbury
Dennis Camell
Jason Coder
Chriss Hammerschmidt*
Randall Direeen
Jeff Guerrieri

Electromagnetics Division
National Institute of Standards and Technology
325 Broadway
Boulder, CO 80305

*Chris Hammerschmidt now with
Institute for Telecommunications Science
325 Broadway
Boulder, CO 80305

July 2011



U.S. Department of Commerce

Gary Locke, Secretary

National Institute of Standards and Technology

Patrick D. Gallagher, Director

Certain commercial entities, equipment, or materials may be identified in this document in order to describe an experimental procedure or concept adequately. Such identification is not intended to imply recommendation or endorsement by the National Institute of Standards and Technology, nor is it intended to imply that the entities, materials, or equipment are necessarily the best available for the purpose.

National Institute of Standards and Technology Technical Note 1558
Natl. Inst. Stand. Technol. Tech. Note 1558, 125 pages (July 2011)
CODEN: NTNOEF

U.S. Government Printing Office
Washington: 2005

For sale by the Superintendent of Documents, U.S. Government Printing Office
Internet bookstore: gpo.gov Phone: 202-512-1800 Fax: 202-512-2250
Mail: Stop SSOP, Washington, DC 20402-0001

Table of Contents

Abstract	1
1. Introduction	2
2. Unique Challenges in the SPF	3
3. Theoretical relationships for large complex cavities.....	6
4. Numerical Modeling and Predictions	9
4.1. Field levels predicted for ideal chamber	9
4.2. Simple Low-Frequency Numerical Simulations for the SPF.....	13
4.2.1. SPF Model at 30 MHz	14
4.2.2. SPF Model at 50 MHz	17
4.2.3. SPF Model at 80 MHz	25
4.2.4. 50 MHz model with the space vehicle installed inside cryoshroud.....	28
4.2.5. 80 MHz model with the space vehicle installed inside cryoshroud.....	35
4.2.6. Summary of Modelling Results	37
5. Instrumentation and Experiments.....	37
5.1. Measurement Systems.....	37
5.1.1. Vector Network Analyzer (VNA) System.....	37
5.1.2. Isotropic Electric Field Probe System.....	40
5.1.3. Ambient Signal Monitoring System	47
5.2. Measurement Objectives	47
5.2.1. Ground Level Test points in the Empty Chamber	48
5.2.2. Ground Level test points with Cryoshroud Floor	56
5.2.3. Tests along the vertical axis by use of the VNA and Probe Systems	62
6. Experimental Data	63
6.1. Basic VNA Measurement Approach.....	65
6.1.1. Low-band Results	69
6.1.2. Mid-band Results and Anomalies.....	71
6.1.3. High Frequency Results and Anomalies	73
6.1.4. Overall Summary.....	76
6.1.5. Derived Quantities.....	80

6.1.6. Electric Fields	83
6.2. Basic Probe System Measurement Results	87
6.3. Chamber Shielding.....	102
6.4. Ambient Signals	107
7. Uncertainty Considerations	116
7.1 Uncertainty due to Random Nature of Mode-Stirred Chamber Measurements.....	117
7.2 Estimation of the Standard Uniformity	117
8. Conclusions and Recommendations.....	118
9. Acknowledgements	120
10. References.....	120

An Electromagnetic Evaluation of the NASA Space Power Facility at Plum Brook Station

Galen Koepke, John Ladbury, Dennis Camell,
Jason Coder, Chriss Hammerschmidt*, Randall Direen, Jeff Guerrieri

Electromagnetics Division
Radio Frequency Fields Group
National Institute of Standards and Technology
Boulder, Colorado 80305

*Chriss Hammerschmidt is now with the
Spectrum and Propagation Measurements Division

Institute for Telecommunications Science
Boulder, Colorado 80305

Abstract

We describe in this report (Technical Note) an extensive electromagnetic evaluation of a unique test facility designed and built by the National Aeronautics and Space Administration (NASA). The Space Power Facility is presumed to be the world's largest high-vacuum test chamber and is designed to qualify vehicles and equipment for outer-space conditions. The interior of the aluminum chamber measures 30.5 meters (100 feet) in diameter and 37.2 meters (122 feet) from floor to the top of the dome. The facility is located at the NASA Plum Brook Station near Sandusky, Ohio and is managed by the NASA John H. Glenn Research Center in Cleveland, Ohio.

This set of evaluation measurements and analysis were intended to quantify the electromagnetic characteristics of this chamber while empty. The experimental data that we collected include an extensive set of point-to-point signal-propagation and attenuation (insertion-loss) measurements, direct measurements of electric fields generated in the chamber by a high power radio frequency source, shielding effectiveness of the aluminum shell, and environmental ambient radio frequency signals. These measurements spanned the frequency spectrum from below 100 MHz to 40 GHz. We are able to estimate several important chamber characteristics by analyzing these data. These include attenuation, decay time, mode bandwidth, quality factor (Q), electric field related to input power, and field uniformity.

1. Introduction

The Space Power Facility (SPF) houses a unique and impressively sophisticated vacuum test chamber inside the large dome shown at the center of the building in Figure 1. This facility, located at the Plum Brook Station near Sandusky, Ohio, is part of the NASA John H. Glenn Research Center in Cleveland, Ohio. The SPF is currently being upgraded for use as the primary site for flight qualification tests on the planned Orion space vehicle as part of the National Aeronautics and Space Administration (NASA) Constellation Program. The SPF is designed to qualify vehicles and equipment in outer-space conditions. The interior of the aluminum inner chamber measures 30.5 meters (100 feet) in diameter and 37.2 meters (122 feet) from floor to the top of the dome. This large chamber has the distinction of having the most volume of any known vacuum chamber, at approximately 23,426 cubic meters. If we compare this to other large electromagnetic test chambers (non vacuum) then the SPF is dwarfed only by the Benefield Anechoic Facility at Edwards Air Force Base in California. That massive chamber contains about 130,825 cubic meters of volume [1] and is lined completely with radar-absorbing material. The volume of a large reverberation facility in Australia capable of enclosing a fighter-sized aircraft [2] is approximately 1362.3 cubic meters in comparison. A chamber described in [3] was evaluated as an empty reverberation chamber prior to being lined with radar-absorbing material and used as a semi-anechoic (no absorber on the floor) room. This chamber had a volume of about 2354 cubic meters.

NASA intends to perform all preflight environmental tests (vibration, vacuum, thermal, electromagnetic) on the new space vehicle at the SPF location. Fortunately, all the electromagnetic tests will be done at normal atmospheric conditions and will not require that test equipment be capable of space conditions

The NIST role in this program is to investigate the viability of adapting the aluminum vacuum chamber to an electromagnetic test chamber. The major part of this effort was to perform a series of tests in the chamber to evaluate how to execute these tests by use of reverberation, direct illumination, or some other technique. This set of evaluation measurements and analysis was intended to quantify the electromagnetic characteristics of this chamber while empty. The experimental data that we collected include an extensive set of point-to-point signal-propagation and attenuation (insertion-loss) measurements, direct measurements of electric fields generated in the chamber by a high-power radio-frequency source, shielding effectiveness of the aluminum shell, and environmental ambient radio frequency signals. These measurements spanned the frequency spectrum from below 100 MHz to 40 GHz.



Figure 1. Aerial view of NASA Space Power Facility located at the Plum Brook Station near Sandusky, Ohio. (Photo courtesy of NASA)

We first discuss some of the characteristics of large conductive cavities that are pertinent to the evaluation of this unique chamber and a few predictions based on relatively simple models in sections 2, 3, and 4. The test methods and analysis of the measurement data are described in sections 5 –7. Finally, based on the measurement data and analysis, we summarize the key findings in section 8.

2. Unique Challenges in the SPF

The most obvious features of the SPF aluminum inner chamber, from the viewpoint of electromagnetic fields, are the highly conductive surfaces (aluminum), vast surface area, and symmetric geometry (cylinder and hemisphere). The big question for this project is how best to use this chamber as an electromagnetic environmental effect (E3) test chamber, given these features. Most electromagnetic vulnerability (EMV) tests (RTCA/DO-160 [4], MIL-STD 461 [5], IEC 61000-4-21 [6], etc.) presume that the radiated field intensity in the test environment can be established. The most common techniques to establish known field intensity within the

confines of a metallic enclosure are: (1) suppress all reflections (anechoic) and use direct illumination from a characterized antenna; (2) maintain a highly reflective environment and utilize complex cavity theory (reverberation); (3) use some absorbing material and determine field by use of probes or sensors; or (4) use very short impulsive signals (time-domain) or transforming finely-sampled frequency domain data (synthetic-time-domain) to illuminate the test object and remove reflections by time-gating (time-domain). There are also some practical variations on these three (e.g., semi-anechoic) depending on what test environment one is trying to emulate.

The first technique (anechoic) requires that all conductive (reflective) surfaces be covered with radar-absorbing material in order to suppress the reflections. This approach would make the chamber appear similar to outer space for the radio signals, in keeping with the overall theme of the facility. There are several advantages to this approach, such as clearly defined intensity, polarization, and incident angle of the test signal by use of a well characterized transmit antenna. However, there are also disadvantages, primarily cost, manipulating the transmit antenna to expose all parts of the spacecraft, and the daunting logistics of reconfiguring the chamber for the thermal vacuum and other tests (removing absorber and associated adhesives).

The second technique (reverberation) would require little or no modification to the surfaces in the chamber (a big advantage), no mechanical scanning of the test object by the source antenna (a time saver), and would provide a more complete exposure of the spacecraft to the test fields. However, there may also be some disadvantages. The reverberation technique utilizes the multi-mode nature of large cavities to generate a statistically uniform field. The chosen geometry for reverberation chambers is usually rectangular, as that shape performs well and is economical to construct. However, the SPF is cylindrical with a hemispherical cap. This geometry would tend to produce undesired mode structures such as whispering-gallery modes and modes that focus energy in specific locations. These can cause problems when one is trying to establish a uniform statistical field structure. Placement of the tall cylindrical spacecraft assembly near the center of the chamber will introduce even more symmetry (a coaxial structure) that may add to this problem. Then there is the question of the mode density at the low frequencies (10 MHz or so); will the modes be sufficient at these frequencies to enable a uniform field? This concern is valid for all techniques, including anechoic, because typical anechoic material has poor performance at low frequency, and the chamber behaves like a loaded shielded room. If ferrite tiles are added to improve the low-frequency anechoic performance, the cost would become astronomical. The reverberation technique requires a reasonable mode density. The large volume of the SPF chamber is helpful but still may be insufficient at 10 MHz. The large volume may be helpful to enable low-frequency operation, but the volume also raises another issue. One virtue of the reverberation technique is the fact that energy is uniformly distributed throughout the volume, but in a very large chamber that also means that the transmitted power is dispersed over this large volume and thus results in a lower power density at any given point. This intuitive result is

evident in the following relationship between the transmitted power and the average power received by any impedance-matched, lossless antenna (eq. 94,[7])

$$\langle P_R \rangle = \frac{\lambda^3 Q}{16\pi^2 V} P_t, \quad (1)$$

where P_t is transmitted power, λ is the wavelength, Q is the chamber quality factor, and V is the chamber volume. We can see that a large volume may be offset somewhat by a higher Q ; in other words, if less power is absorbed or lost in the chamber (higher Q) then more is available at the receiving antenna. Fortunately, the aluminum surfaces in the SPF chamber are highly conductive and help to reduce power lost to the walls. However, the overall chamber Q is a function of all loss mechanisms in the chamber: lossy objects, aperture leakage, and power dissipated in the antenna terminations, in addition to power dissipated in the walls [8]. While we can estimate a value for Q based on assumptions about an empty chamber with no leakage or lossy objects, we cannot predict the effects of the large door seams, other apertures, and the introduction of lossy objects (e.g., cryogenic shroud panels and Orion spacecraft). Hence, the only way to know how much power is available at a test location from a given transmitting source is by measurement.

The very high Q of a chamber may be beneficial for enhancing signal strength of a continuous wave signal. But there is a downside to a high Q chamber; the modulated and impulsive signals tend to ring for a long time ($\tau = Q/\omega$, where τ is the time constant and ω is the radian frequency), causing difficulties in testing these signals. The long signal decay times make it problematic to remove the reflections by time-gating. This brings us to the subject of how to test impulsive signals (radar pulses, etc.) in this environment. The effects of the chamber on the pulsed signals are documented in several reports [9], [10], and [11]. The two pulse signal parameters usually considered are the risetime and the amplitude. The objective for most tests appears to be reaching a steady-state condition by loading the chamber with absorbing material or using pulses longer than the time constant of the chamber in order to reach a given field strength. This would provide a correlation to the more typical CW testing but does not address the issue of the effects on the risetime or what to do with shorter pulses that do not reach steady-state. The authors of a NASA technical report [12] demonstrated that it is possible to obtain meaningful immunity threshold information on an actual risetime-sensitive equipment under test (EUT), “even if the chamber time constant exceeds the region of EUT risetime sensitivity.” In other words, the chamber time constant (usually derived from an average of many realizations of the pulse envelope) may not adequately quantify the instantaneous pulse characteristics impinging on the EUT. Also, the early time statistics of the pulsed rf signal have been studied [13]. Clearly, this is an area that needs more research and testing before a realistic EMC test method can be validated. However, it may be possible that even high- Q chambers such as the SPF could be used for pulsed rf testing, provided that the interaction of the chamber, signal and test device parameters are better understood.

3. Theoretical relationships for large complex cavities

Theoretical descriptions of large complex cavities are available from multiple sources, but we have relied on three principal sources [7][14][15]. A detailed analysis is beyond the scope of this report, so instead we present a few of the theoretical relationships between various electromagnetic parameters in an ideal reverberation chamber, and then use these results as a baseline for comparison while evaluating the SPF. For most reverberation-chamber measurements, there is a requirement for some type of change of the electromagnetic configuration of the chamber (generally caused by a change of boundary condition by moving a large conductive surface, such as a paddle or a wall boundary, change of frequency, or changing the location of an electromagnetic source inside the chamber). Similarly, a sensor can be moved to multiple locations in the chamber. Although this generally does not have the same effect as a configuration change (a configuration change should change the electromagnetic configuration of the chamber throughout the volume of the chamber, but a sensor-location change would, ideally, have no effect on a separate stationary sensor). By taking measurements for different configurations or sensor locations, we are able to “sample” the characteristics of the chamber. With enough samples, it should be possible to generate a statistical description for any electromagnetic parameter in the chamber. For an ideal chamber, the statistical descriptions should be independent of location and orientation of any sensor throughout a large portion (known as the working volume) of the chamber.

Unfortunately, most electromagnetic parameters such as received power, Cartesian electric field (which we define here as an arbitrary rectangular component of the electric field assuming an arbitrary Cartesian coordinate system), or total electric field, change dramatically from configuration to configuration. Changes of 20 dB are common (a factor of 10 different for a Cartesian field, or a factor of 100 for received power) and changes of 60 dB were observed during this investigation. This large variation implies that many samples may be required before reliable comparisons can be made. Fortunately, statistical models are available for ideal chambers [7][14][15] that allow us to predict the variation we might expect under ideal circumstances. For this analysis we will focus on the average of each parameter, which should be the best behaved parameter.

For simplicity, we will start with received power, which ideally has an exponential distribution. This distribution has a standard deviation that is equal to its mean, which in some sense implies 100% uncertainty (e.g. 1 ± 1 W, or $1 \text{ W} \pm 100\%$). Expressing a standard deviation on a dB scale is somewhat complicated if the standard deviation is large (on the order of the mean). For example, 1 ± 1 W implies that we expect a value of 1 W, but the “true” answer could be as high as 2 W or as low as 0 W. On a dB scale, this implies that we expect a value of 0 dB relative to 1 W, but the true answer could be 3 dB higher or ∞ dB lower, which we can summarize as $0 +3/-\infty$ dB relative to W.

By averaging over N samples, we can reduce the standard deviation of the mean (SDOM) by a factor of \sqrt{N} , so 4 samples will reduce the SDOM by a factor of 2, 16 samples will reduce the SDOM by a factor of 4, and so on. For both practicality and simplicity, all measurements reported here were based on either 12 samples (as recommended as a lower limit by reverberation chamber standards [4][6]) or 141 samples (a convenient number which relates to a rough averaging bandwidth of 10 MHz using our VNA measurement system, described in section 5.1.1). These give reduce the SDOM by a factor of 3.5 for 12 samples and by a factor of 12 for 141 samples. Similar approaches can be used for the Cartesian field (which ideally has a Rayleigh or chi or χ distribution with 2 DOF (degrees of freedom) and a standard deviation that is 52 % of the mean) or the total electric field (which ideally has a χ distribution with 6 DOF and a standard deviation that is 29 % of the mean) and results are summarized in Table 1 below.

Table 1. SDOM for various parameters and number of samples.

Quantity	1 sample	SDOM	
		12 samples	141 samples
Received power	100 % or +3.0/-∞ dB	29 % or +1.1/-1.5 dB	8 % or ±0.4 dB
Cartesian electric field	52 % or +3.7/-6.4 dB	15 % or +1.2/-1.4 dB	4 % or ±0.4 dB
Total electric field	29 % or +2.2/-3.0 dB	8 % or +0.7/-0.8 dB	2 % or ±0.2 dB

Once the average response is known, it is possible to predict the peak response for a given number of samples as well. The idea here is to perform some test with N samples and determine the peak response. Repeat multiple times for different configurations (different paddle positions, similar but not identical frequencies, different source or sensor locations, etc.) and then evaluate the characteristics (mean, standard deviation, etc.) of the measured peak signal. The expected peak will be a function of the number of samples, and will gradually increase as the number of samples increases. If the underlying distributions are known, then the characteristics of the peaks can be predicted as well. The general procedure is to determine the average response, then multiply by a scale factor that is determined for each parameter and number of samples. Since most parameters are related to either power, Cartesian or rectangular field components, or total field, we have developed tables of scale factors for these parameters, and refer to these as $P(N)$ for power, $R(N)$ for Cartesian (or rectangular) field, and $T(N)$ for total field. This process must be used with caution, however, because low losses combined with large values of N can result in predicted received powers that are larger than the power transmitted into the chamber. Details can be found in [14].

Many of our measurements are related to receive power normalized to incident power. This can be represented as either the ratio of the received power to the incident power P_{rec}/P_{inc} , or $|S_{21}|^2$ in terms of S parameters. Once we have an estimate of the average normalized received power, we can predict most other parameters. We summarize the relationships in Table 2 for average and peak received power, average and peak Cartesian field, average and peak total field, and the quality factor Q . In this table, “normalized” values are normalized to an incident transmitted power of 1 W. Derivation of other parameters is discussed later.

Table 2. Equations for estimating the descriptive characteristics of a chamber.

Parameter	Constant incident power
Average normalized received power	$\langle S_{21} ^2 \rangle$
Average received power	$P_{inc} \langle S_{21} ^2 \rangle$
Maximum normalized received power	$\langle S_{21} ^2 \rangle [P(N)]$
Maximum received power	$P_{inc} \langle S_{21} ^2 \rangle [P(N)]$
Average Cartesian field	$\sqrt{\frac{80\pi^3 \langle S_{21} ^2 \rangle P_{inc}}{\lambda^2}}$
Maximum Cartesian field	$\sqrt{\frac{80\pi^3 \langle S_{21} ^2 \rangle P_{inc} [R(N)]^2}{\lambda^2}}$
Average total field	$\sqrt{\frac{1125\pi^3 \langle S_{21} ^2 \rangle P_{inc}}{4\lambda^2}}$
Maximum total field	$\sqrt{\frac{1125\pi^3 \langle S_{21} ^2 \rangle P_{inc} [T(N)]^2}{4\lambda^2}}$
Quality factor Q	$\frac{16\pi^2 V \langle S_{21} ^2 \rangle}{\lambda^3}$

4. Numerical Modeling and Predictions

In this section we examine the SPF chamber by use of statistical relationships developed for ideal reverberation chambers and by use of a commercial electromagnetic modeling code. This analysis was completed prior to performing measurements in the chamber in an effort to understand some of the characteristics and assist in developing a sensible test plan, not to provide a complete analysis of the chamber. Additionally, the numerical modeling effort examined a few configurations with objects such as the cryogenic shroud panels (we will also use the shorthand term cryo-panels) and a spacecraft inserted in the volume, which were not part of the experimental evaluation. The numerical analysis was limited to the lower frequencies, due to the size of the volume and computer limitations.

4.1. Field levels predicted for ideal chamber

For an empty chamber, there are two principal power sinks: the chamber walls and the antennas placed in the chamber. From NIST Technical Note 1508, eq. 26 [14] and assuming steady-state conditions, the average power dissipated $\langle P_D \rangle$ in the chamber is equal to the average transmitted power $\langle P_T \rangle$, and we have

$$\langle P_T \rangle = \langle P_D \rangle = \frac{2\omega\delta(\omega)A\langle W \rangle}{3} + N \frac{c^3\pi\langle W \rangle}{2\omega^2}, \quad (2)$$

where ω is the radian frequency, $\delta(\omega)$ is the skin depth of the metal walls of the chamber, A is the surface area of the chamber walls, $\langle W \rangle$ is the average energy density in the chamber, N is approximately the number of antennas in the chamber, and c is the speed of light. It is useful to express the above equations in terms of wavelength λ rather than ω , and it is also useful to write the equations in terms of total electric field E_T rather than energy density. We use $\eta_0 = \sqrt{\mu_0/\epsilon_0}$,

the intrinsic wave impedance of free space, $\omega = \frac{2\pi c}{\lambda}$ and $\langle W \rangle = \frac{\langle |E_T|^2 \rangle}{c\eta_0}$, to get

$$\langle P_T \rangle = \langle P_D \rangle = \frac{4\pi\delta(\lambda)A\langle |E_T|^2 \rangle}{3\lambda\eta_0} + N \frac{\lambda^2\langle |E_T|^2 \rangle}{8\pi\eta_0} = \frac{\langle |E_T|^2 \rangle}{\eta_0} \left(\frac{4\pi\delta(\lambda)A}{3\lambda} + N \frac{\lambda^2}{8\pi} \right). \quad (3)$$

Typically, measurements utilize two antennas, one transmitting antenna and one receiving antenna. However, due to enhanced backscatter, the transmitting antenna actually removes more power from the chamber than the receiving antenna. Therefore we will assume that $N=3$ as a conservative initial estimate.

Given the equations above, we would like to estimate the power required to establish a known electric field. But what does that really mean? Is that a total field or a Cartesian component of the field? RTCA DO160 [4] specifies field in terms of total field, but IEC 61000-4-21 [6] specifies field in terms of a Cartesian component. Regardless of which we choose, there are other subtle problems. For one, in a statistical environment such as a reverberation chamber, there can be a significant difference (5 dB or more) between a peak field and an average field, and the difference increases as the number of configurations (paddle positions, antenna locations, frequencies) increases. Finally, unlike simple deterministic environments, there is a difference between saying that a device is exposed to a field of 100 V/m and a squared field of 10,000 V²/m², which is also different from a field of 40 dB V/m. So, what should we do?

We will generate a few curves showing required power, assuming an expected peak field of 200 V/m, assuming both total and Cartesian field, and also assuming 12 independent samples.

Our first step is to rewrite the equations in terms of either total field or Cartesian field ($N=3$):

$$\langle P_T \rangle = \langle P_D \rangle = \frac{\langle |E_T|^2 \rangle}{\eta_0} \left(\frac{4\pi\delta(\lambda)A}{3\lambda} + 3 \frac{\lambda^2}{8\pi} \right) = \frac{3\langle |E_R|^2 \rangle}{\eta_0} \left(\frac{4\pi\delta(\lambda)A}{3\lambda} + 3 \frac{\lambda^2}{8\pi} \right). \quad (4)$$

Our next step is to write things in terms of the average magnitude of the field, rather than the average squared magnitude. To do this, we need to know something about the statistical distribution of the field. For simplicity, we will assume the chi or χ distribution, having two DOF (degrees of freedom) for a Cartesian component of the electric field, and six DOF for the total field [7]. In this case we can write

$$\langle |E_T|^2 \rangle = \langle |E_T| \rangle^2 \frac{768}{225\pi} \approx \langle |E_T| \rangle^2 \cdot 1.0865 \quad (5)$$

and

$$\langle |E_R|^2 \rangle = \langle |E_R| \rangle^2 \frac{4}{\pi} \approx \langle |E_R| \rangle^2 \cdot 1.27324. \quad (6)$$

Next, we look at the peak field, assuming a specific number of samples. These are summarized in Table 3.

Table 3. Scale factor to estimate peak field from average.

Number of samples M	E_T scale factor $S_T(M)$	E_R scale factor $S_R(M)$
10	1.477	1.891
12	1.508	1.950
100	1.810	2.553
1000	2.072	3.078

We can now write an estimate for the power required to generate a desired peak electric field

$$\begin{aligned} \langle P_T \rangle = \langle P_D \rangle &= \frac{[E_T]_M^2 \cdot 1.0865}{[S_T(M)]^2 \eta_0} \left(\frac{4\pi\delta(\lambda)A}{3\lambda} + 3\frac{\lambda^2}{8\pi} \right) \\ &= \frac{3[E_R]_M^2 \cdot 1.27324}{[S_R(M)]^2 \eta_0} \left(\frac{4\pi\delta(\lambda)A}{3\lambda} + 3\frac{\lambda^2}{8\pi} \right). \end{aligned} \quad (7)$$

All we need now is the surface area of the chamber and the skin depth of the walls. Based on dimensions given in the web site, the chamber is 37.2 m (122 feet) high and has a diameter of 30.5 m (100 feet). That implies that the chamber can be roughly modeled as a cylinder 22 m (72 feet) high and radius of 15.2m (50 feet), capped by a hemisphere with a radius of 15.2m (50 feet), and sitting on a circle with a radius of 15.2m (50 feet). The surface area is given as

$$A = \pi R^2 + 2\pi R h + 2\pi R^2 = 4290.4 \text{ m}^2. \quad (8)$$

The skin depth is a function of frequency and the conductivity of the walls. Assuming aluminum, we found conductivities σ in the range of 1.5×10^7 S/m to 3.8×10^7 S/m [16]. However, in a previous experiment, Hill [17] found the microwave conductivity to be much lower than

expected. The lower value was 8.83×10^6 S/m, so we will use this as the minimum estimated conductivity. The skin depth $\delta(\lambda)$ can be calculated from the conductivity as [17]

$$\delta(\lambda) = \sqrt{\frac{\lambda}{\pi c \mu \sigma}} . \quad (9)$$

We can now estimate the power required to generate a 200 V/m peak field under ideal conditions and assuming no additional losses.

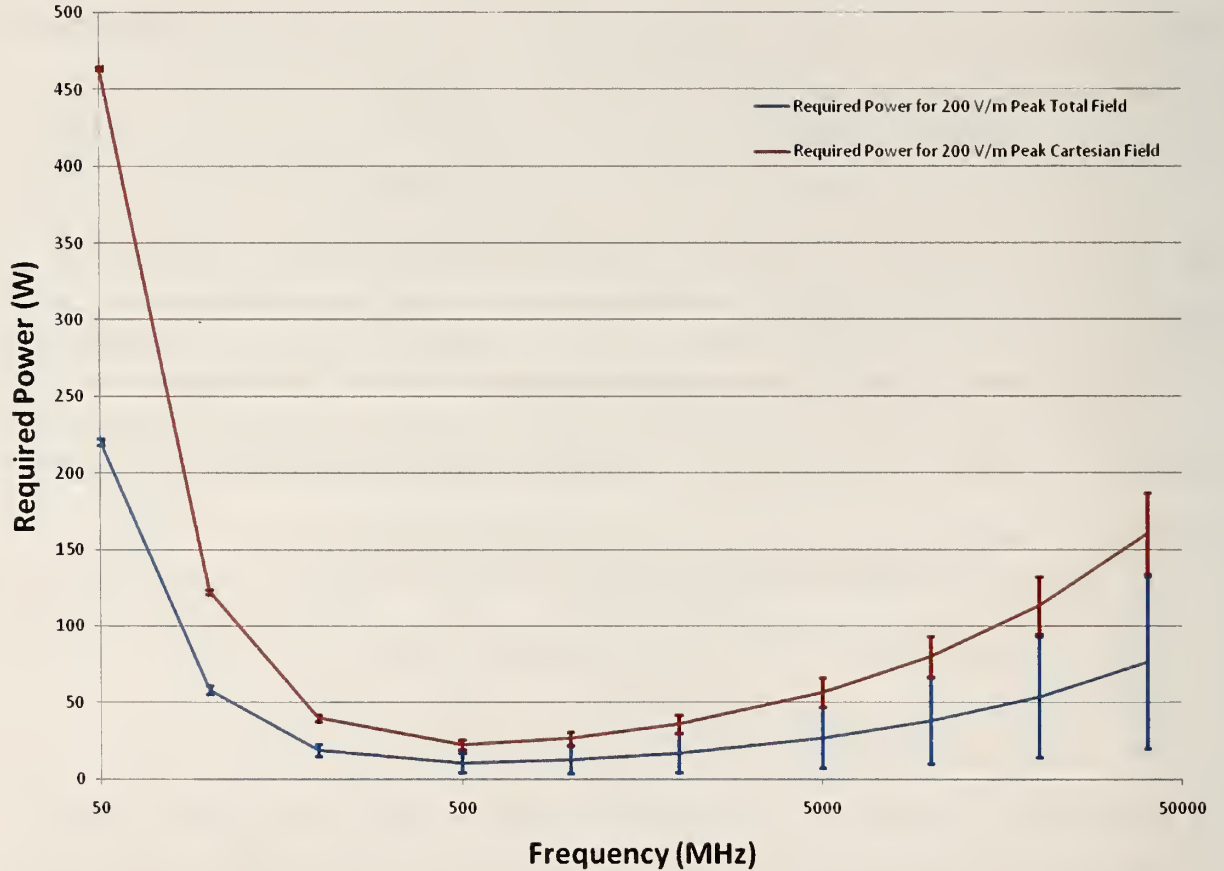


Figure 2. Multiple predictions for the power required to generate a 200 V/m peak field using 12 samples.

Figure 2 shows an estimate of the power required to generate a 200 V/m field assuming a measurement based on 12 samples, electrical conductivities that are constant with frequency, and that all losses are due to the antennas or ideal aluminum walls. The range shown on each curve (total spread of approximately 3 dB) indicates variations caused by the possible range in conductivity for aluminum. The range is small at lower frequencies (below 1 GHz), because the losses are dominated by the antennas and will not be strongly influenced by different wall conductivities. The required power can be reduced by approximately 3 to 4 dB if 1000 samples are used rather than 12.

Most likely, this chart grossly underestimates the power required to generate a 200 V/m field. Welds, seams, lights, apertures, and the additional contents of the chamber will all increase the loss of the empty chamber. In NBS Tech Note 1092, losses were approximately 5 dB higher than expected. Some of this may be attributable to the microwave permeability of the walls, but that is still unknown. These required powers shown may need to be increased substantially (5 to 10 dB) to account for these possible losses. Finally it is quite possible that the test object will be a significant load on the chamber. The surface area of the test object could be on the order 10 % of the chamber surface area, which should have a negligible effect, assuming the conductivity of the test object is similar to that of the chamber walls. However, an open support structure made of steel beams could have a significant impact.

As a final estimate, 120 W should be sufficient to generate a 200 V/m peak field in the empty chamber under ideal assumptions and conditions from 100 MHz to 18 GHz. A more realistic estimate would be closer to 1 kW. At lower frequencies there could be problems. Final power estimates are based on an experimental evaluation of the SPF and are described in section 6.1.6.

4.2. Simple Low-Frequency Numerical Simulations for the SPF

We were tasked to measure the reverberation characteristics of the Space Power Facility (SPF), which is depicted in Figure 3. Due to the symmetrical nature of the chamber, we were concerned that the chamber would exhibit specific modal characteristics at lower frequencies. To understand where the natural modes of the cavity occurred, some simple simulations were run prior to traveling to Sandusky, Ohio to measure the electromagnetic characteristics of the chamber. These simulations were not intended to provide an accurate 3-dimensional model of the facility but rather to simulate the possible impact of various measurement scenarios at the lower frequencies and provide some insight to assist in developing a measurement test plan.

Simulations were performed with a commercial 3D full-wave electromagnetic field simulation by use of the finite-element method. The chamber geometry was developed within the simulation program and the dipole source located within the calculation region. A boundary condition was applied to the model and an initial mesh was then generated. The simulation was iteratively solved at a specified frequency. The simulations were run at 30 MHz, 50 MHz, and 80 MHz. The model consisted of the chamber and the door buttresses, and later the Orion module was added to the model. Initially a conductivity of copper, 5.8×10^7 Siemens/m, was used for the cavity walls, and after some initial measurements the cavity walls were changed to reflect the conductivity of aluminum, 3.77×10^7 Siemens/m. A 15 cm dipole was introduced into the cavity to excite the fields. At 50 MHz we looked at incorporating large fabric panels. At 50 MHz and 80 MHz we looked at the fields both with and without the vehicle, and finally, we incorporated both the vehicle and the cryoshroud into the cavity at 50 MHz. We introduced the vehicle and the cryoshroud to understand “hot spots” that could be generated due to the cryoshroud’s circular geometry coupled with the circular geometry of the space vehicle. The following sections summarize the results of these simulations.

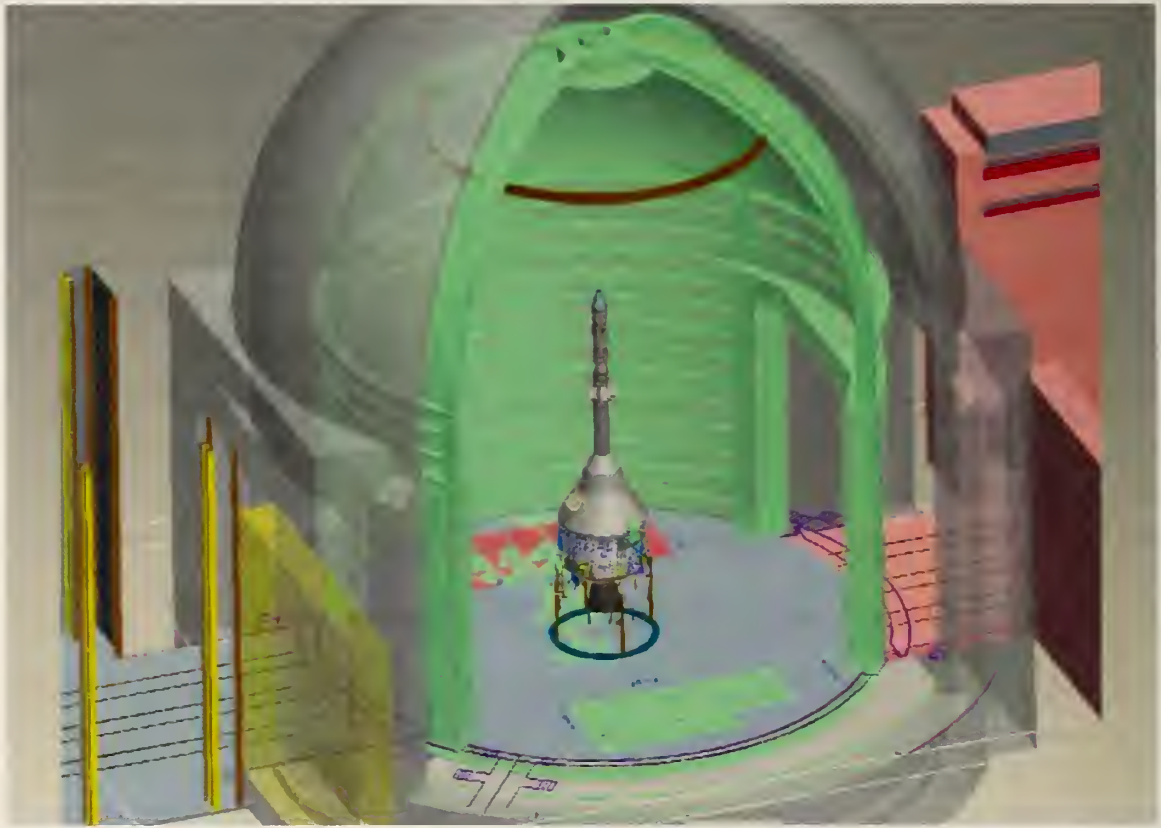


Figure 3. Schematic of Space Power Facility with Orion spacecraft shown inside. (Drawing courtesy of NASA)

4.2.1. SPF Model at 30 MHz

The following model contains the door buttresses and is calculated based on a wall conductivity of 5.8×10^7 Siemens/m. The simulation meshing is shown in Figure 4 where over 400,000 tetrahedra were used in the final calculation. Figure 5 shows the total E-field along the xz-axis. This axis does not go through the axis that cuts through the middle of the buttresses but lies along the axis perpendicular to it. An area of high electric field strength is seen about 100 m above the floor, indicating a natural resonant mode. The field distribution along both the xz-axis and yz-axis is shown in Figure 6. The yz-axis is the axis that cuts through the middle of the buttresses. Another distinct area of high electric field strength lies on the yz-axis about 90 m above the floor of the SPF chamber. By rotating Figure 6, we can locate the dipole antenna, which was positioned at 5.2 m (17 ft.) above the floor of the chamber, shown on a cut in the xy-

axis as shown in Figure 7. This figure gives us an indication of the electric-field strength throughout the rest of the chamber.

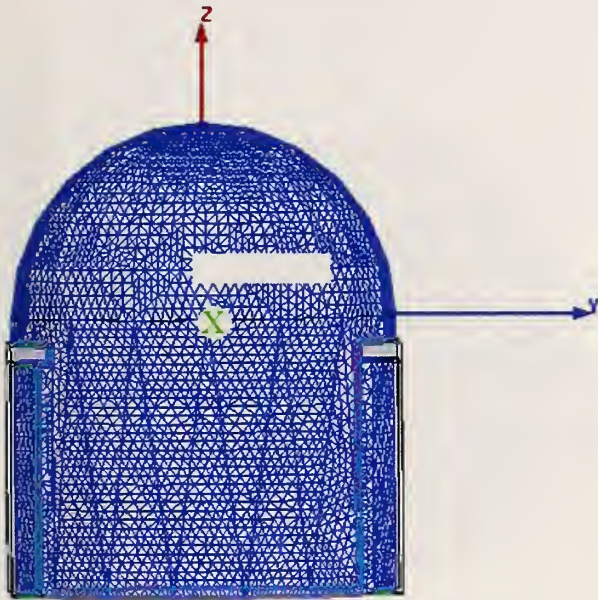


Figure 4. 30 MHz model showing the final adaptive mesh.

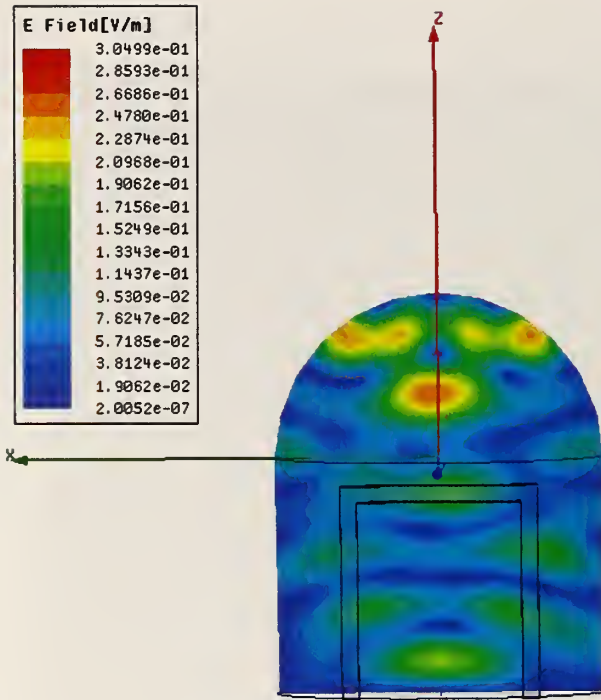


Figure 5. Total electric-field distribution in the SPF chamber at 30 MHz along the xz-axis.

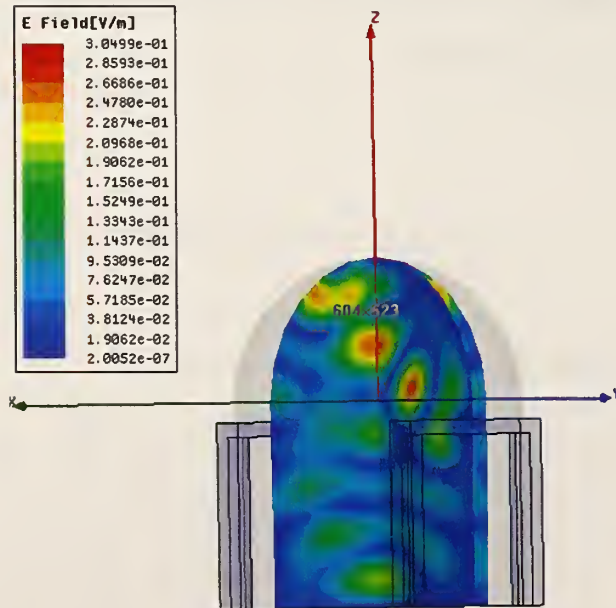


Figure 6. Total electric-field distribution, at 30 MHz, in the SPF chamber along the xz-axis and yz-axis. The yz-axis cuts through the plane in middle of the buttresses.

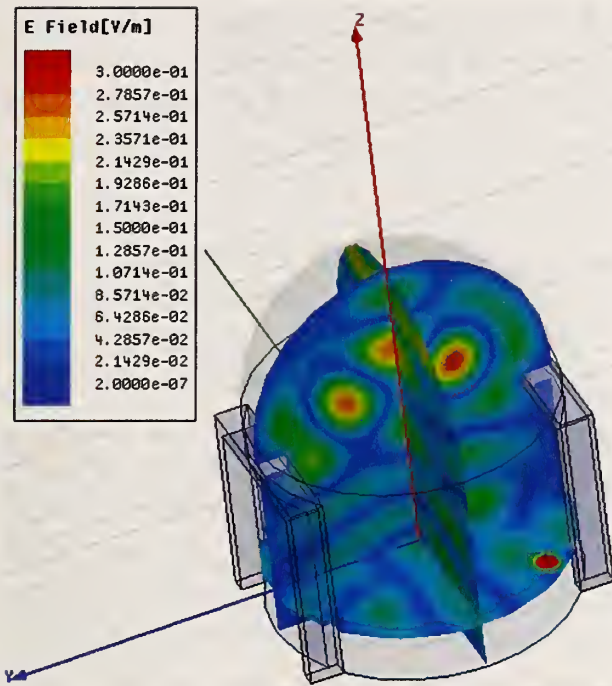


Figure 7. The dipole antenna is shown in the lower, right side of the model. This is the total electric-field distribution along the xz-axis and yz-axis at 30 MHz.

4.2.2. SPF Model at 50 MHz

This model was solved at 50 MHz for a wall conductivity of 3.77×10^7 Siemens/m, the conductivity of aluminum. The final adaptive mesh is shown in Figure 8 and contains close to 700,000 tetrahedra. A total electric-field plot along the xz-axis and yz-axis is shown in Figure 9. At this frequency, more natural resonant modes are set up in the SPF chamber. It appears as though the high electric-field levels seen in the dome in the 30 MHz model are absent at this frequency.

During discussions about the strong modes that could be set up in the SPF chamber due to the geometry, a suggestion was made to use large sheets of conductive fabric to stir the fields, as is done with a metallic paddle in a reverberation chamber. To model this, two conductive sheets were drawn into the model suspended above the chamber floor (see Figure 10); a top view showing how the panels are oriented with respect to the chamber walls is shown in Figure 11. To demonstrate how the field distribution changes as the conductive, fabric panels move (maybe

due to the presence of a large fan), the orientation of the fabric panels was changed five separate times. Figure 12 shows the five separate models in and the different orientations of the fabric panels and how they were changed to simulate the movement of the fabric. The field distribution plots for each of these five models are shown in Figure 13. This simulation seems to show that the fabric panels do not break up the modes in a significant way.

The next thing we incorporated into the 50 MHz model was the vehicle including the Automatic Launch Abort System (ALAS) without their antennas. The structure was modeled with Perfect Electrical Conductors (PEC). Figure 14 and Figure 15 are field-distribution plots showing the vehicle centered in the SPF chamber. Figure 14 shows the field distribution plotted along the xz-axis and yz-axis as in Figure 9, but the outline of the vehicle can be seen. Modes have been introduced along the outer edge of the vehicle due to the presence of the vehicle and the circular geometry of both the vehicle and the cavity. Figure 15 shows the field distributions for the axes offset 5 m from the center. The purpose here was to understand the uniformity within the cavity at a point away from the center of the cavity. We then wanted to know how the fields would change if the vehicle were offset from the center of the cavity. This was done to avoid a coaxial-type phenomenon created by the circular nature of the SPF chamber (outer conductor) and the space vehicle (inner conductor). These plots are shown in Figure 16 and Figure 17. Figure 16 shows the vehicle offset 5 m from the center xz- and yz-axes and the field distributions plotted on those same axes. The field distribution at the center of the cavity is shown in Figure 17 for the central xz- and yz-axes but with the vehicle offset from the center, as in Figure 16.

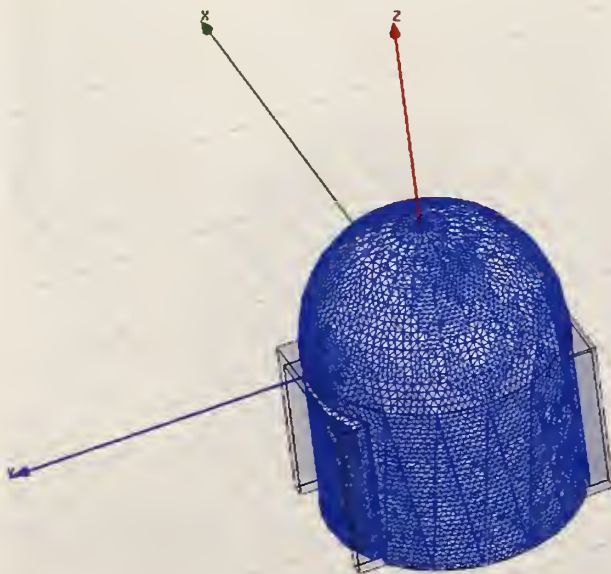


Figure 8. 50 MHz model showing the final adaptive mesh.

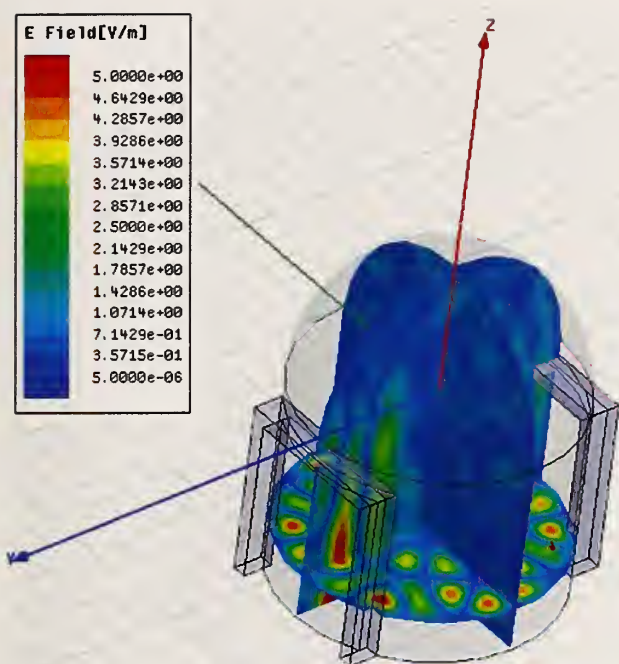


Figure 9. The dipole antenna is in the lower, right side of the model. This is the total electric-field distribution along the xz-axis and yz-axis at 50 MHz.

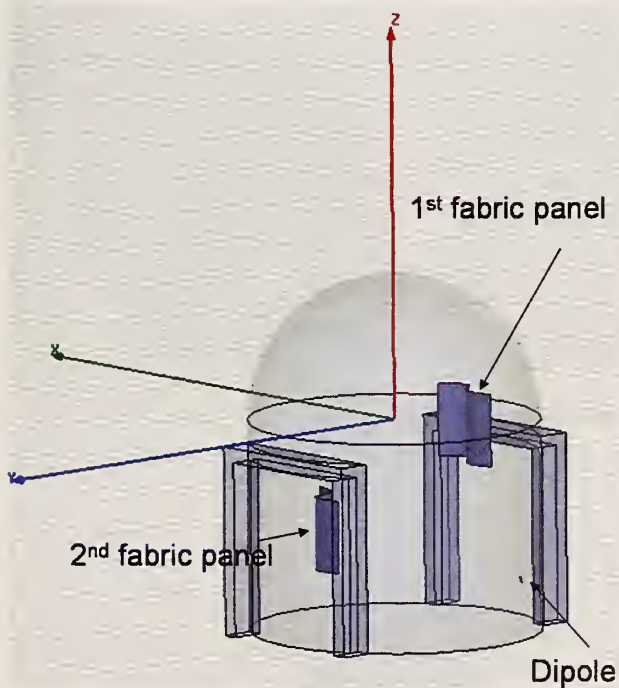


Figure 10. 50 MHz model incorporating conductive fabric sheets that would be used to stir the modes within the SPF chamber.

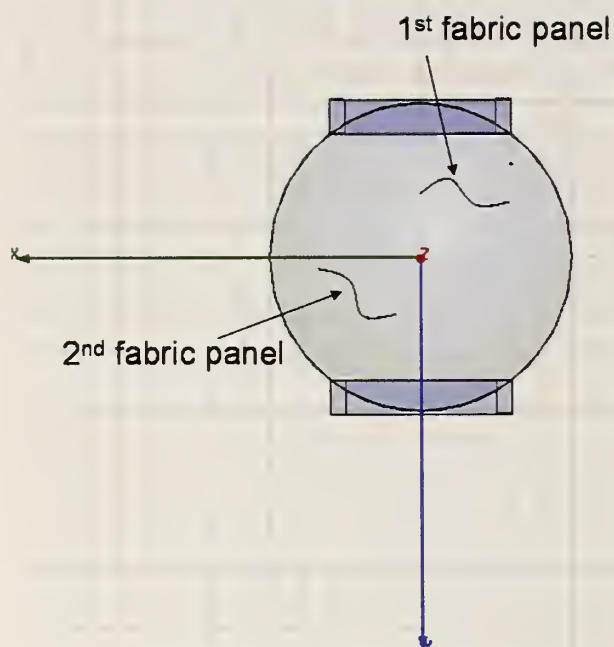


Figure 11. Top view showing the placement of the conductive fabric sheets with respect to the chamber walls.

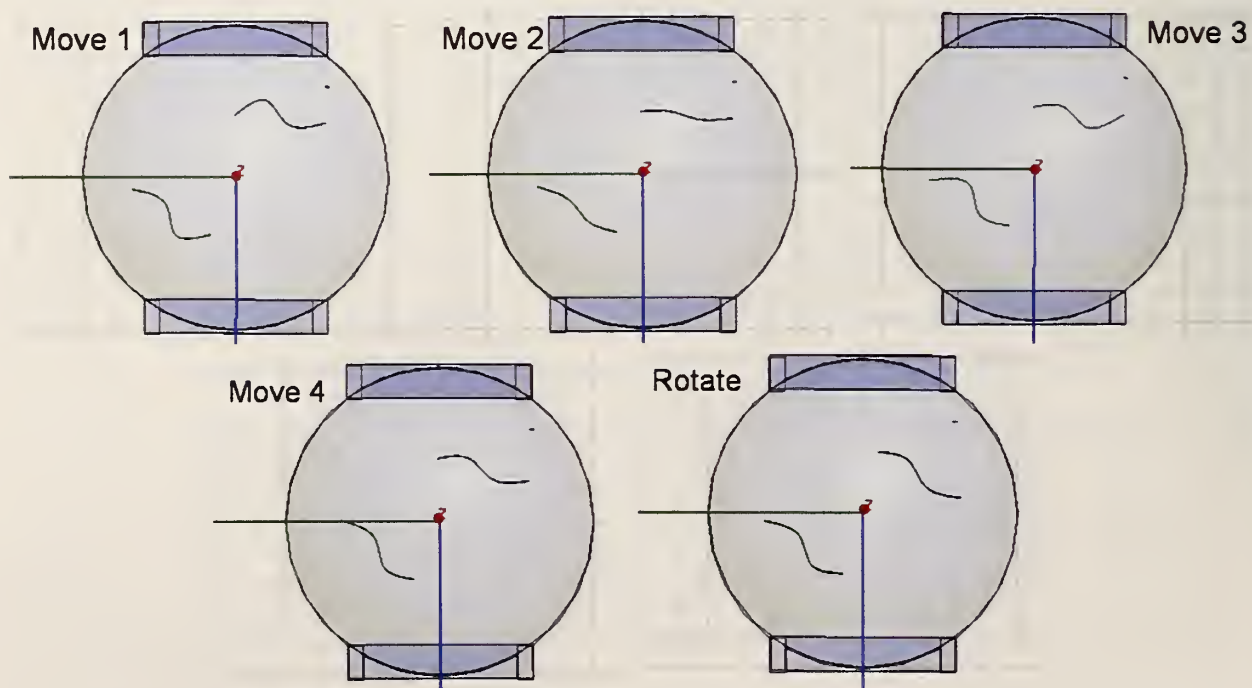


Figure 12. Five different models showing conductive fabric panels and their movement.

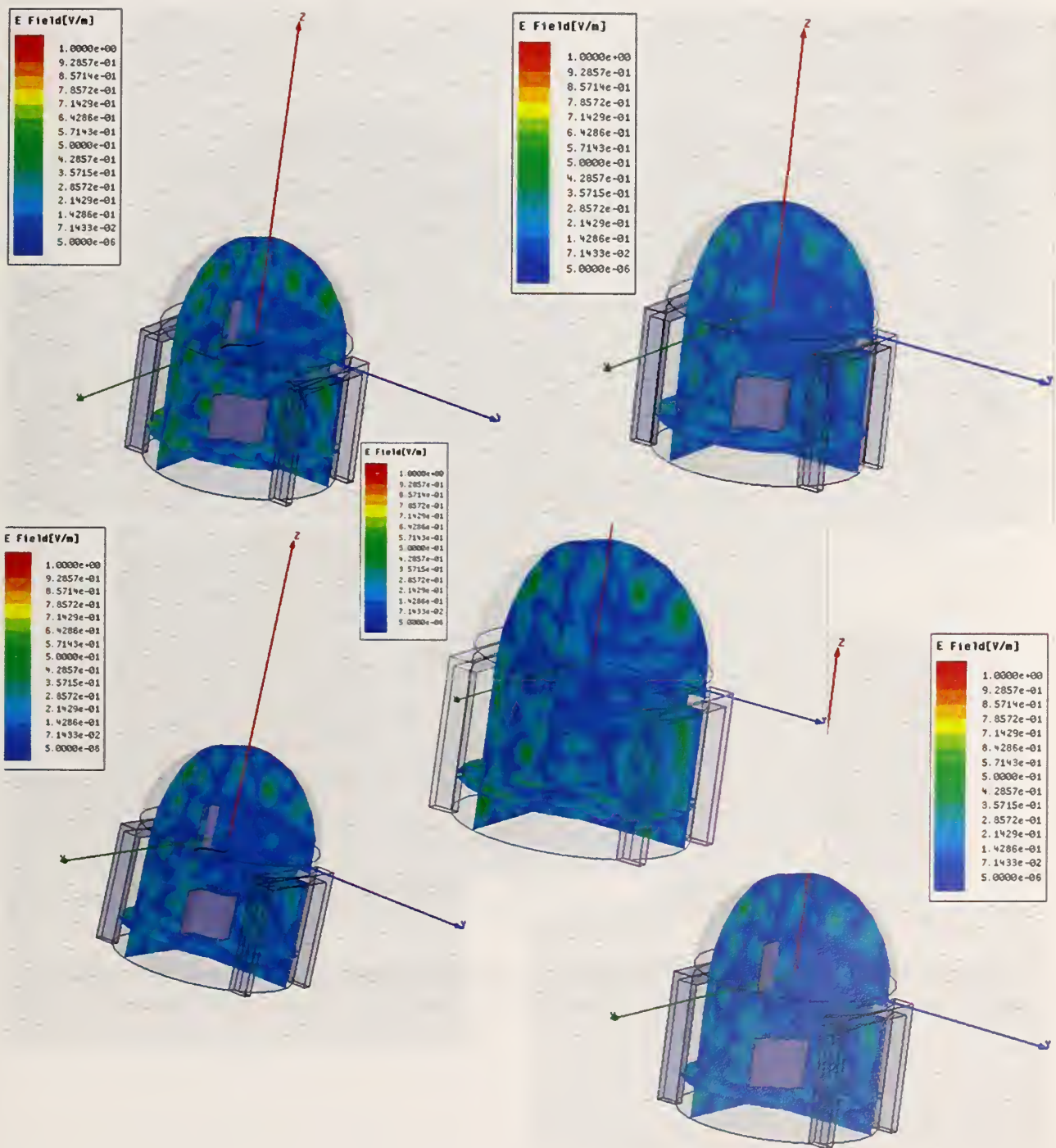


Figure 13. Collage showing change in the field distribution plots as the conductive fabric panels move.

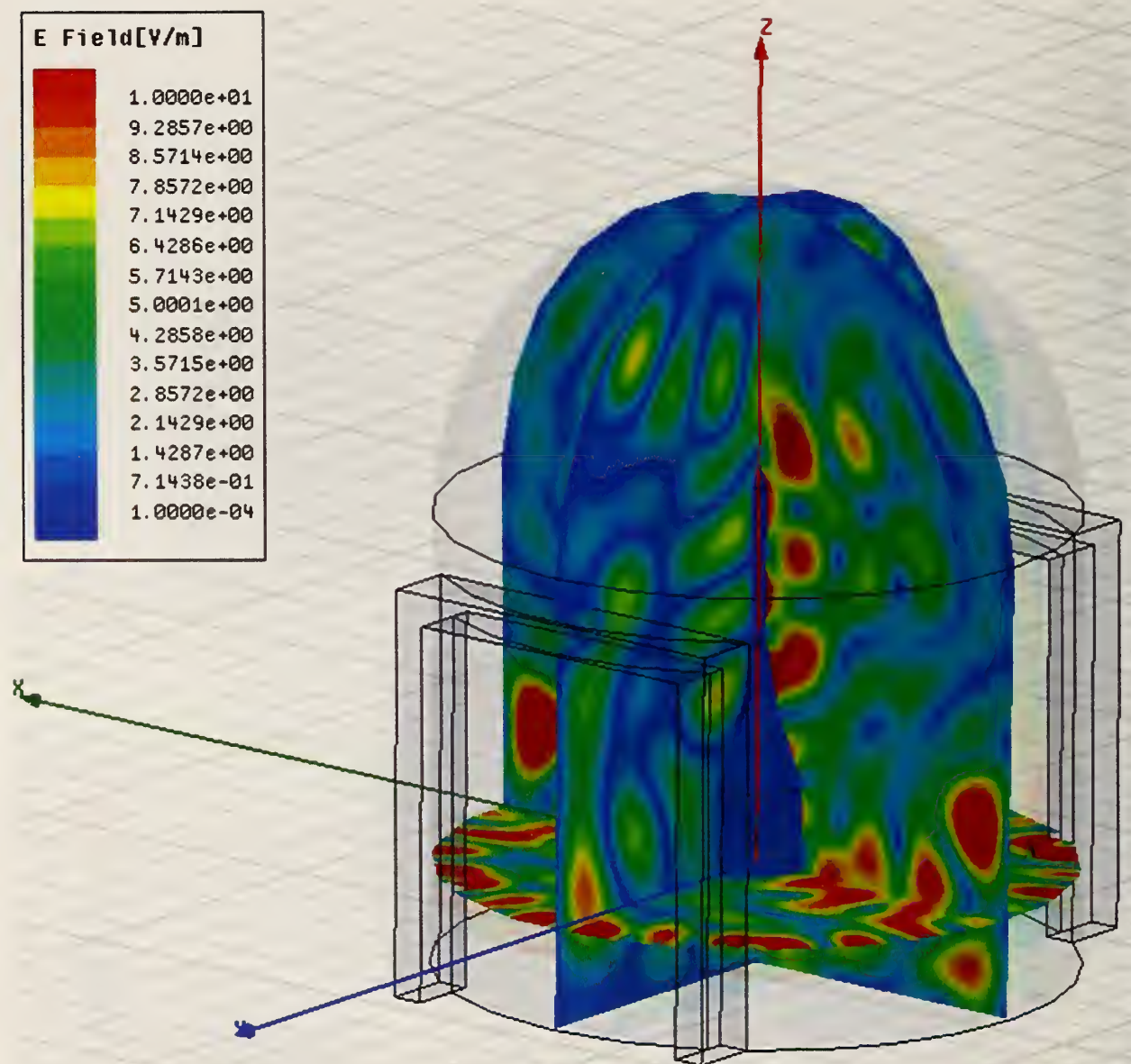


Figure 14. Total electric-field distribution plots at 50 MHz along the xz- and yz-axis for the space vehicle and ALAS centered in the SPF chamber.

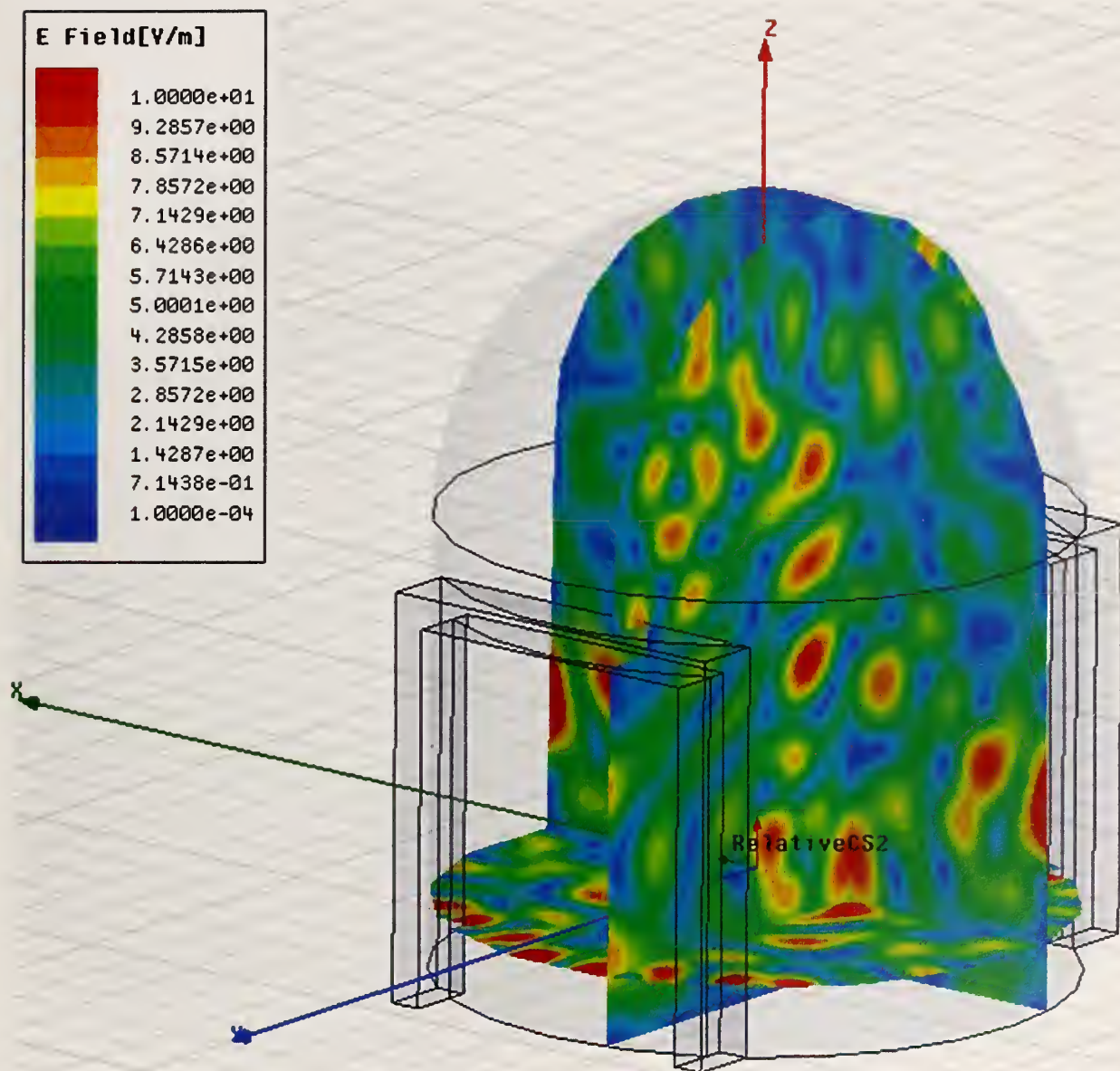


Figure 15. Total electric-field distribution plots at 50 MHz for offset (5 m) xz- and yz-axes for the space vehicle and ALAS centered in the SPF chamber.

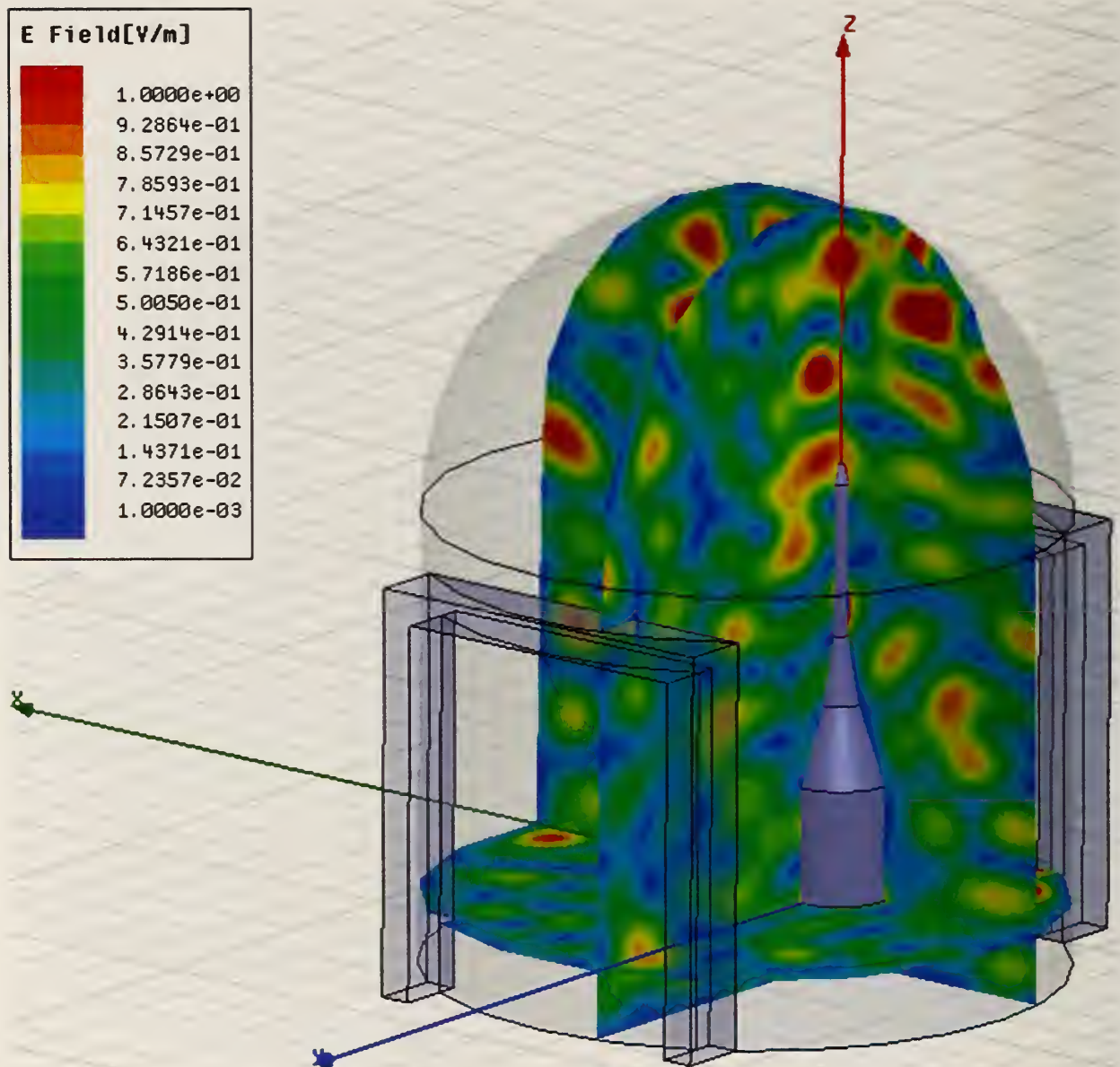


Figure 16. Total electric-field distribution plots at 50 MHz for the space vehicle offset 5 m from the center of the SPF chamber. Fields are plotted along the offset xz- and yz-axes.

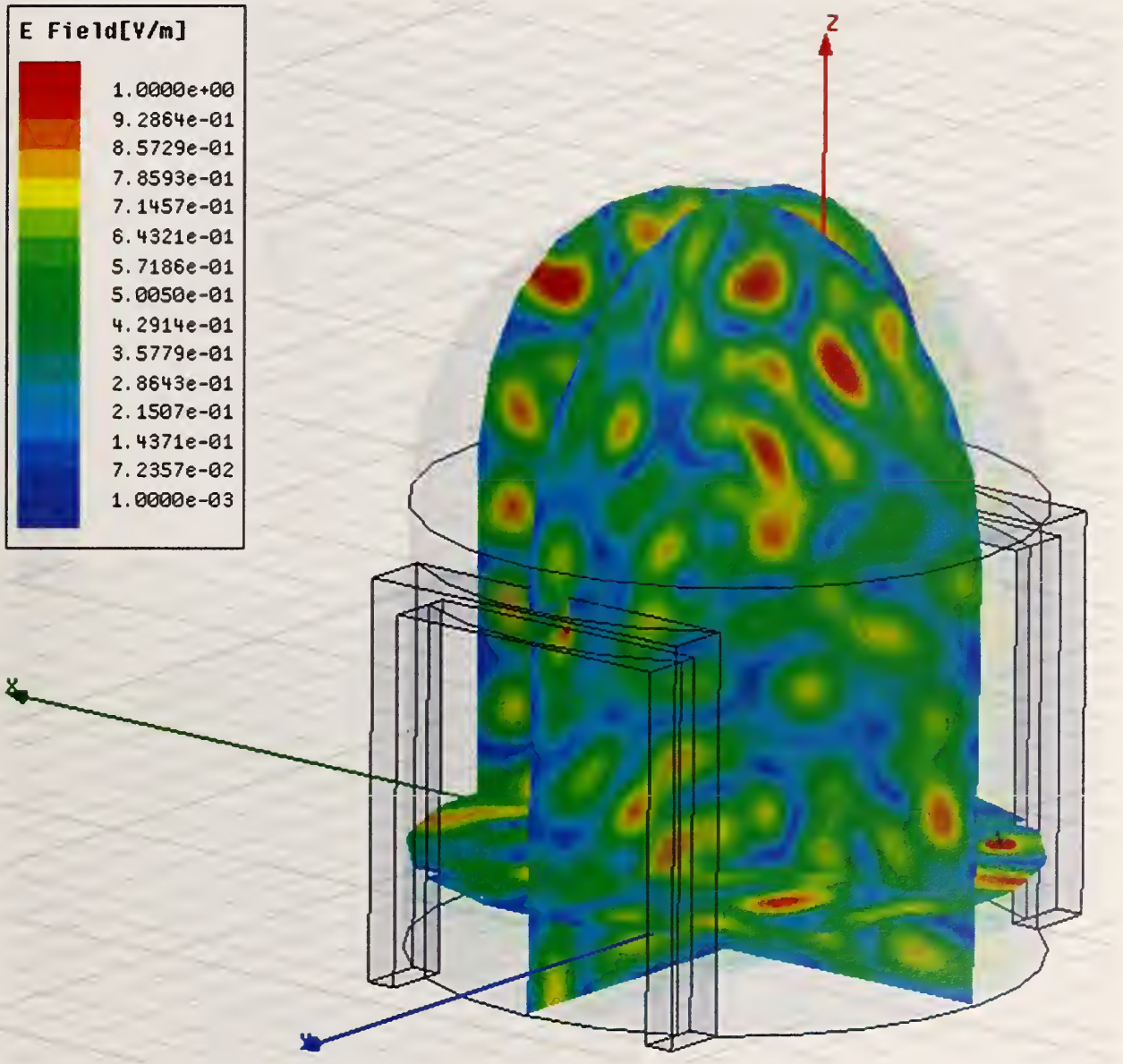


Figure 17. Total electric-field distribution plots at 50 MHz for the space vehicle offset 5 m from the center of the SPF chamber. Fields are plotted along the central xz- and yz-axes of the SPF chamber.

4.2.3. SPF Model at 80 MHz

We developed another model at 80 MHz to show the modal distribution both with and without the space vehicle and ALAS. The modal distribution in the SPF chamber without the space vehicle is shown in Figure 18. We notice that the modal distribution seems to be more random than for the 30 MHz model and the 50 MHz model. We then introduced the space

vehicle offset by 5 m from the center of the cavity and plotted the field distributions along both the central xz- and yz-axes, as shown in Figure 19, and along both the offset xz- and yz-axes, as shown in Figure 20. We do see some high field levels along the ALAS for the vehicle offset from the center of the cavity at 80 MHz.

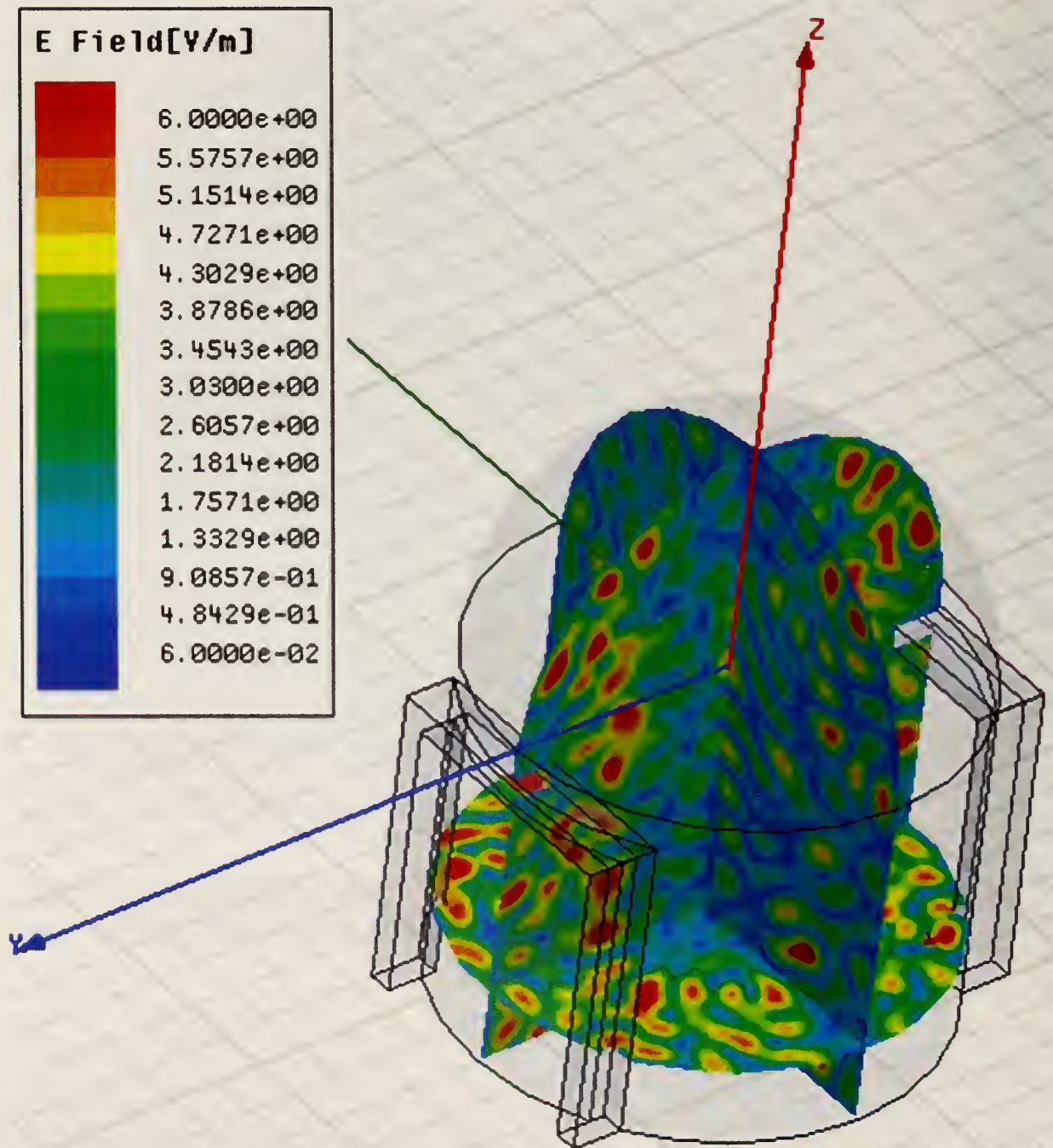


Figure 18. Total electric-field distribution plots along the central xz-axis and yz-axis at 80 MHz. The dipole antenna is in the same location as for previous models.

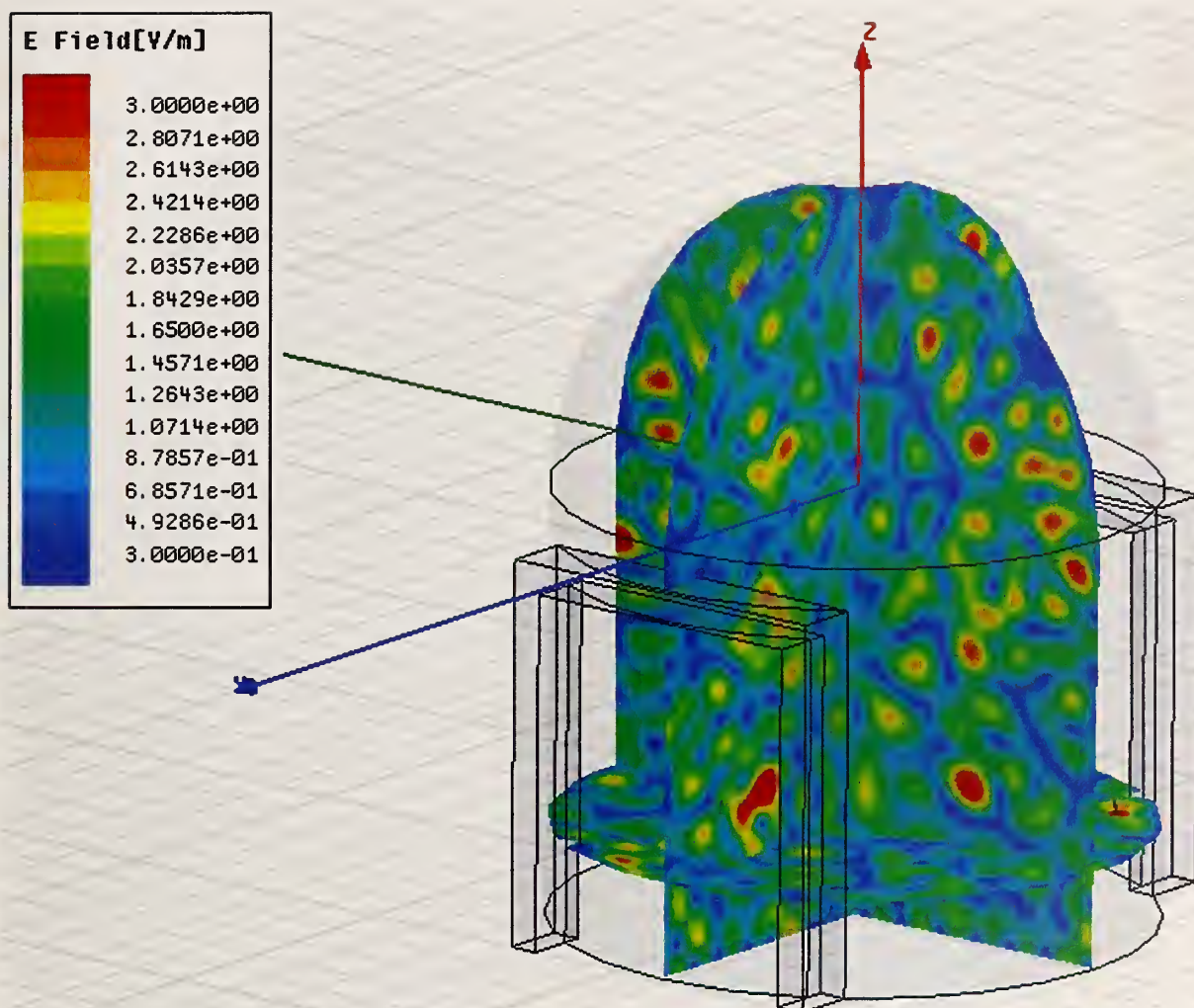


Figure 19. Total electric-field distribution plots at 80 MHz for the space vehicle offset 5 m from the center of the SPF chamber. Fields are plotted along the central xz- and yz-axes.

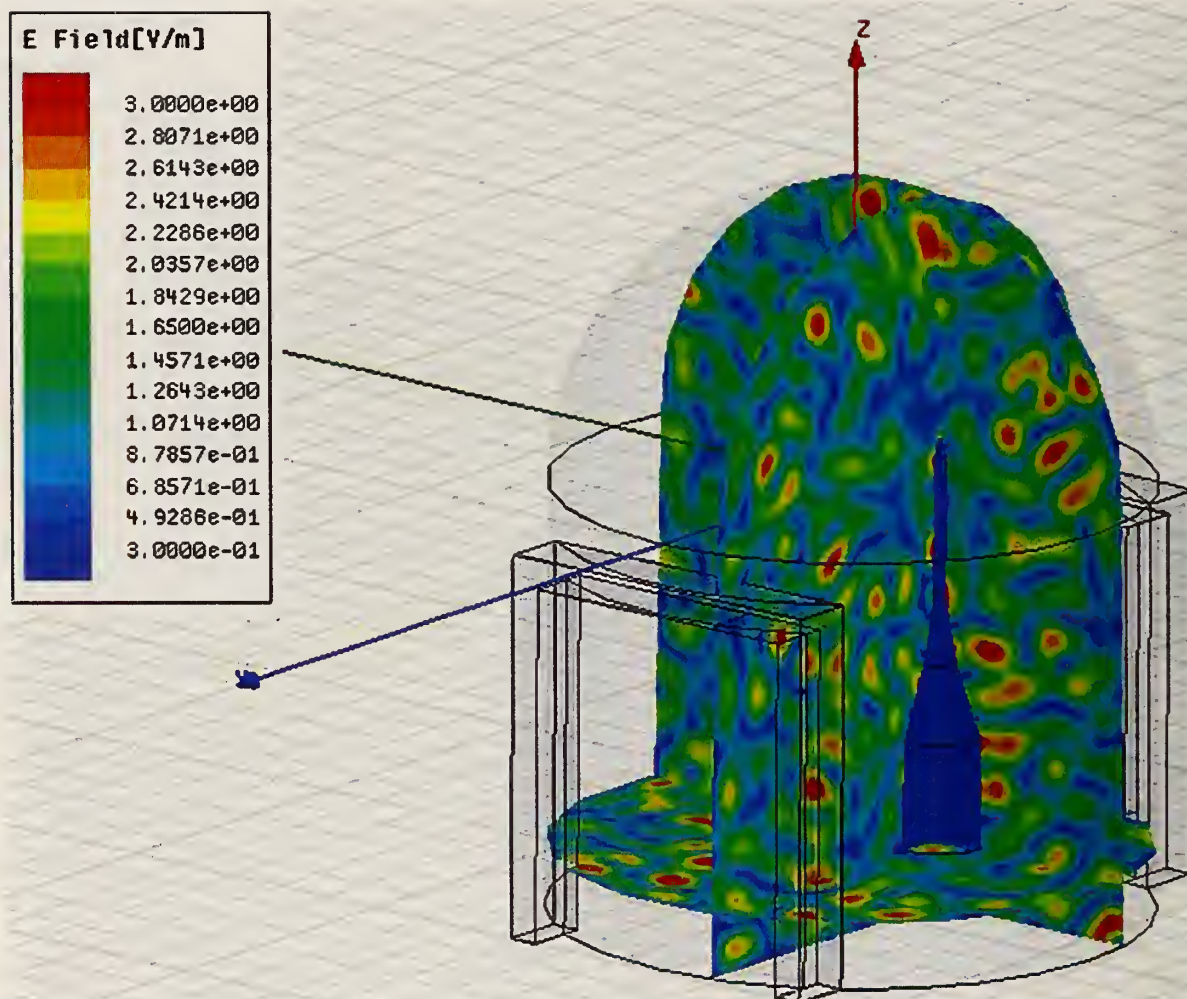


Figure 20. Total electric-field distribution plots at 80 MHz for the space vehicle offset 5 m from the center of the SPF chamber. Fields are plotted along the offset xz- and yz-axes.

4.2.4. 50 MHz model with the space vehicle installed inside cryoshroud

Electromagnetic Interference (EMI) testing of the space vehicle in the SPF chamber was not an independent measurement, but was one of four tests required for certification of the space vehicle. Other tests were to be conducted in and around the SPF chamber. For one of the tests, a cryoshroud needed to be installed inside the SPF chamber to conduct the low-temperature and high-temperature tests to simulate the heating and cooling in space. The test coordinators

wanted to install the cryoshroud on the train car platform that the space vehicle would be attached to prior to the EMI tests and then leave the vehicle and the cryoshroud in place for the EMI tests. The installation and removal of the cryoshroud is a very time-consuming and expensive operation, so the elimination of one step of this process would have benefitted NASA. The problem for the EMI testing is that the cryoshroud is a metal object and, once again, the introduction of this symmetrical geometry lends itself to creating natural resonant modes. One concern was that confining the fields in this small area would possibly create high-level fields around the vehicle and related equipment. Several simulations were run for the cryoshroud and vehicle combination to understand the modal distribution both within the cryoshroud and outside of the cryoshroud. An artist's rendering of the cryoshroud/vehicle combination is shown in Figure 21, and a simple model, including the cryoshroud model developed by NIST, is shown in Figure 22.



Figure 21. Artist's rendering of the bottom portion of the space vehicle inside an infrared (IR) Lamp array and the cryoshroud. (Drawing courtesy of NASA)

In the first set of plots the dipole antenna remained in the same position on the outside of the cryoshroud as for previous models. The total electric-field distribution plots for the vehicle and cryoshroud centered in the SPF chamber is shown in Figure 23. A top view showing these fields and the location of the cryoshroud, the space vehicle and the dipole antenna is shown in Figure 24. We notice a modal pattern outside of the cryoshroud, but no strong modes are set up within the cryoshroud for the antenna located outside of the cryoshroud.

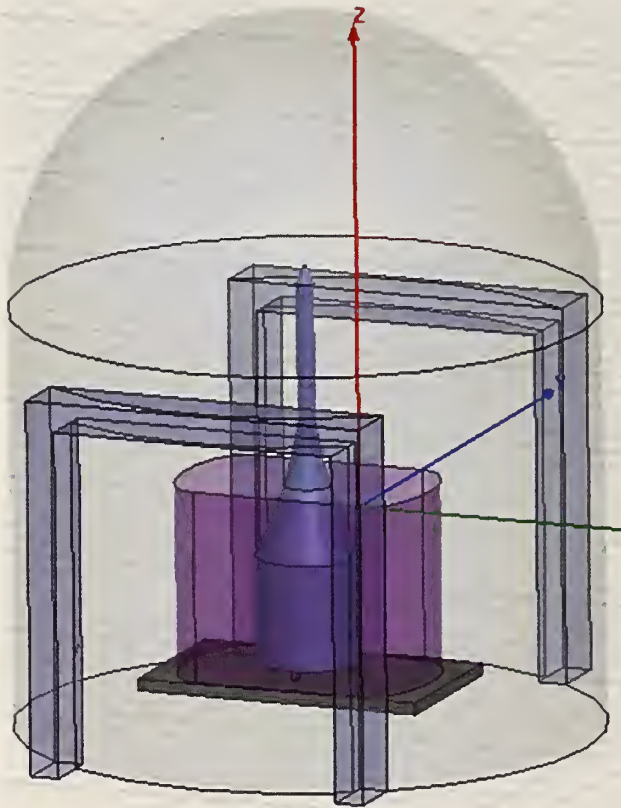


Figure 22. Simple model of vehicle and cryoshroud in SPF chamber.

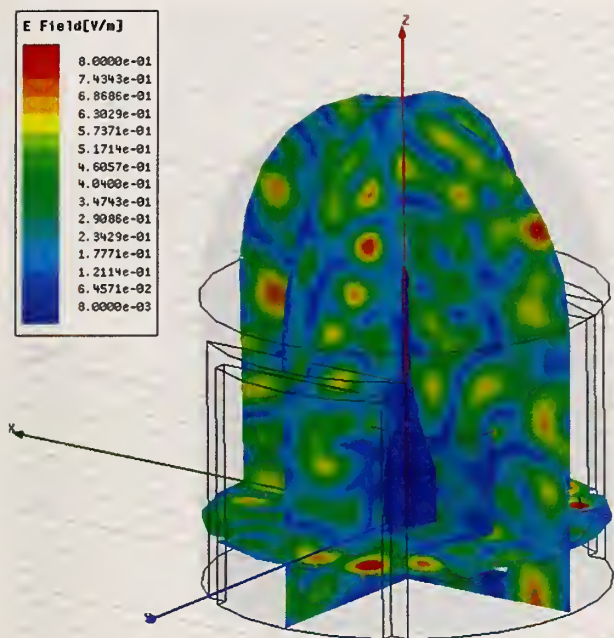


Figure 23. Total electric-field distribution plots at 50 MHz for the vehicle inside the cryoshroud centered in the SPF chamber. The dipole antenna is located on the outside of the cryoshroud.

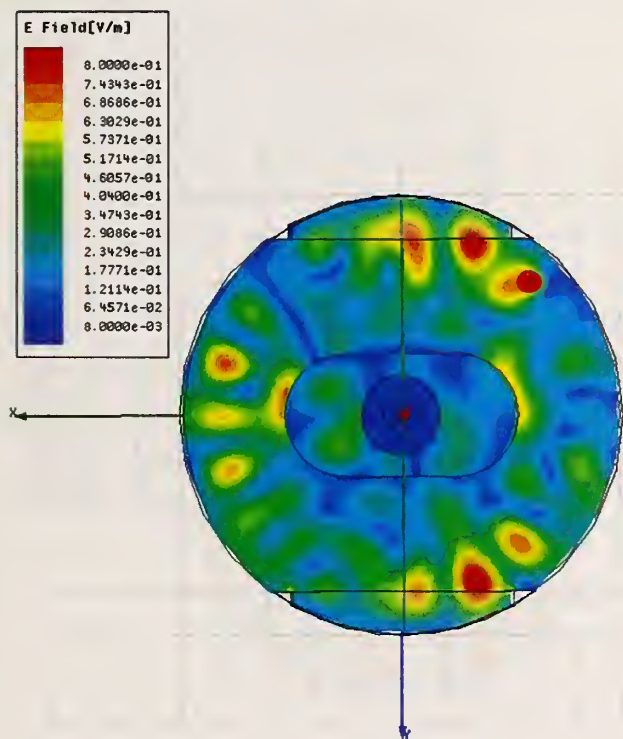


Figure 24. Top view showing total electric-fields within SPF chamber and cryoshroud at a height of 4 m. The space vehicle is the dark blue figure in the center of the cavity. The dipole antenna is located in the upper right quadrant of the figure.

The dipole antenna is now located within the cryoshroud, to simulate an actual measurement, as shown in Figure 25. If we run the model at 50 MHz, we show the different electric field distributions in Figure 26 to Figure 29. Figure 26 shows the field distribution plots along the central xz - and yz -axes for the vehicle and cryoshroud centered in the cavity. Figure 27 shows a top view of this configuration. A top view showing the field distribution for the offset (approximately 3.8 meters along each axis) xz - and yz -axes is shown in Figure 28, and a side view of the field distribution for the offset axes is shown in Figure 29. The modal distribution is very strong both inside and outside the cryoshroud, and the modal distribution inside the cryoshroud may lead to high-field levels near sensitive equipment if the cryoshroud is left around the space vehicle.

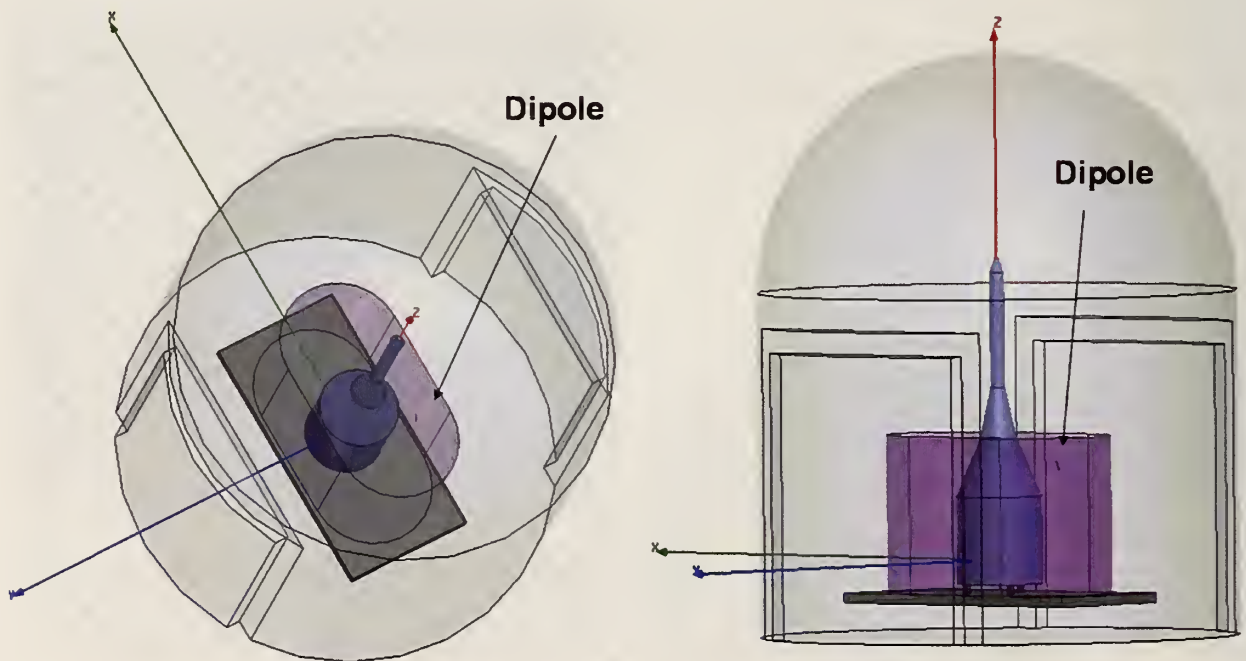


Figure 25. Schematic showing the placement of the dipole antenna inside the cryoshroud.

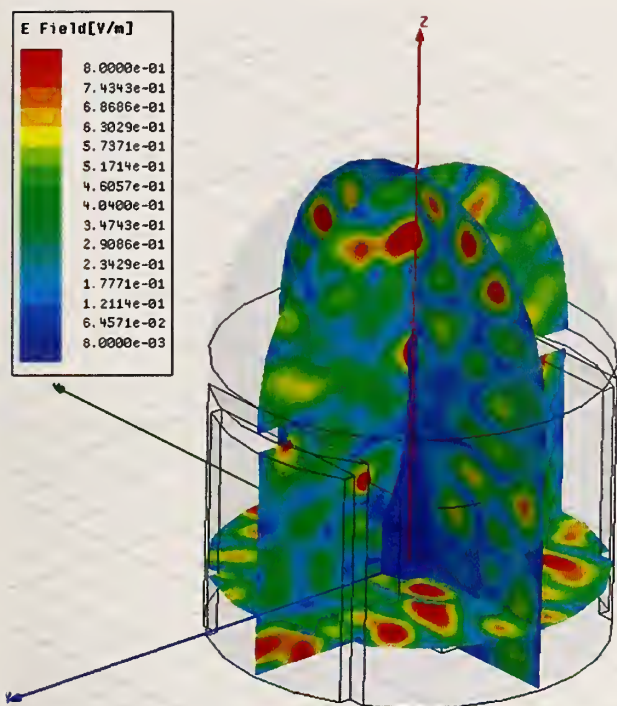


Figure 26. Total electric-field distribution at 50 MHz for the dipole located within the cryoshroud with centered xz- and yz-axes.

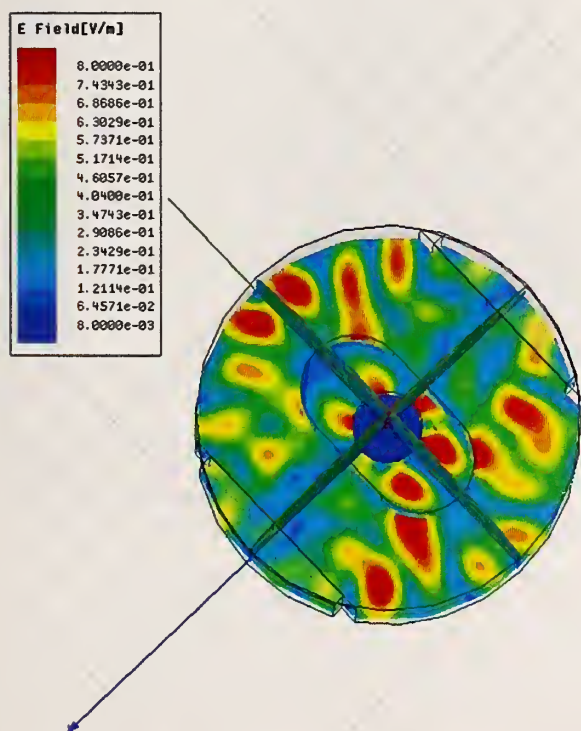


Figure 27. Top view of the total electric-field distribution at 50 MHz for the dipole located within the cryoshroud. The xz- and yz-axis are centered in the cavity.

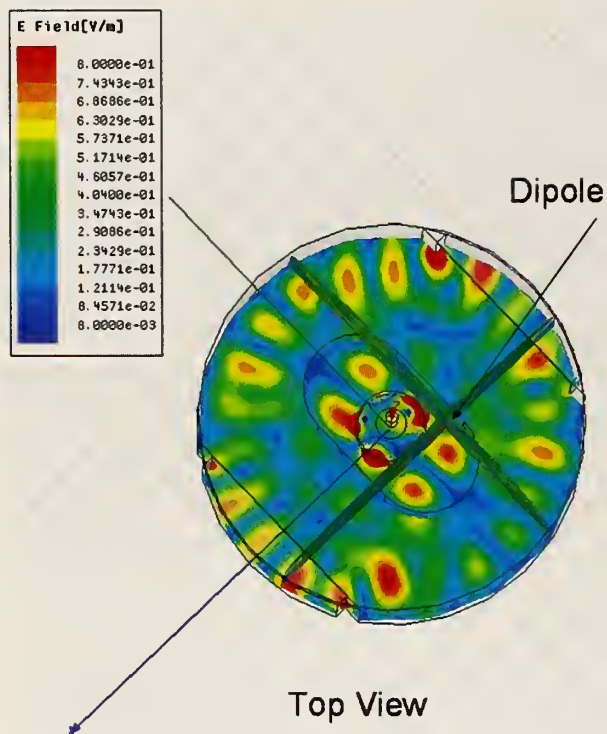


Figure 28. Top view of the total electric-field distribution at 50 MHz for the dipole located within the cryoshroud. The xz - and yz -axis are offset 3.8 m along each axis for a total offset of 5 m from the center.

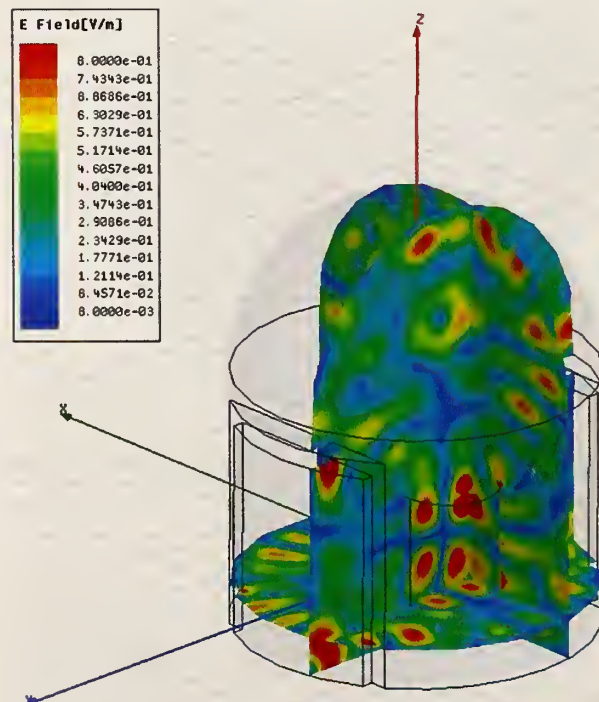


Figure 29. Total electric-field distribution at 50 MHz for the dipole located within the cryoshroud with offset (3.8 m) xz - and yz -axes.

4.2.5. 80 MHz model with the space vehicle installed inside cryoshroud

The last set of models was run for the dipole inside the cryoshroud at 80 MHz. Figure 30 shows the field distribution for the xz - and yz - axes centered in the cavity. Figure 31 and Figure 32 show the field distribution as the dipole is moved up and down inside the cryoshroud. At the position shown in Figure 32, we see the high-level modal fields distributed along the edge of the space vehicle. The dipole in this location seems to couple well to the vehicle inside the cryoshroud.

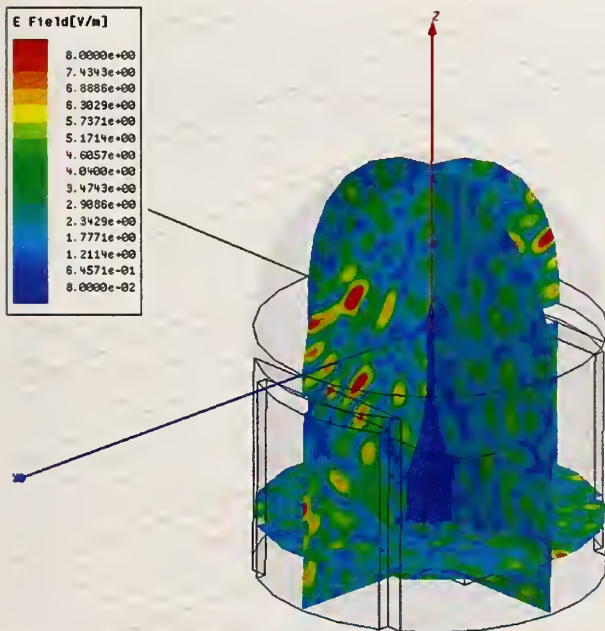


Figure 30. Field distribution at 80 MHz for the dipole located within the cryoshroud with centered xz - and yz -axes.

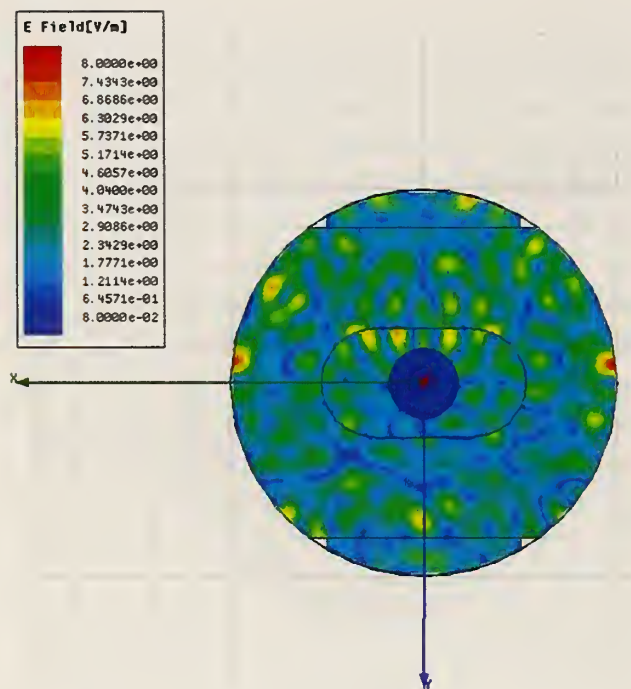


Figure 31. Top view of the field distribution at 80 MHz for the dipole located within the cryoshroud in position 1. The xz- and yz-axis are centered in the cavity.

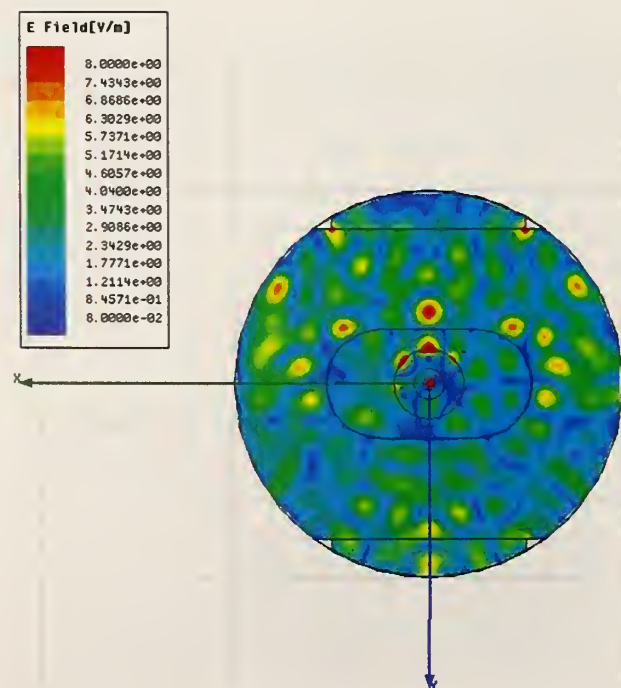


Figure 32. Top view of the field distribution at 80 MHz for the dipole located within the cryoshroud in position 2. The xz- and yz-axis are centered in the cavity.

4.2.6. Summary of Modelling Results

The simple simulations presented here were helpful as a test plan was being designed. They illustrated that the field complexity increased considerably as the frequency increased from 30 MHz to 80 MHz. This would indicate that it will be more difficult to generate uniform field statistics at 30 MHz, probably due to insufficient mode density at these lower frequencies. The simulations also indicated that large conductive curtains would be helpful in perturbing the fields in the chamber. However it still remains a challenge to realize these structures in practice. The final note on the simulations is the effect of the cryoshroud structure on the field. Here we see that this structure would introduce either shadowing or internal focusing that may be problematic during an actual test. We recommend that this configuration be avoided if at all possible.

5. Instrumentation and Experiments

5.1. Measurement Systems

We had several competing goals in evaluating the SPF. We knew that there would not be a large paddle available for the evaluation, so we would need to rely on frequency sampling to evaluate how well the SPF *could* perform as a reverberation chamber. But we also wanted some idea of how the SPF would behave as a “typical” reverberation chamber, even if the paddle used was obviously not ideal for the task. Finally, we also wanted some idea of ambient signal levels, since some preliminary tests indicated possible interference from outside sources. To meet these goals, we decided on three different measurement systems: (a) a vector network analyzer system for measurements at a large number of frequencies but a limited number of locations, (b) an electromagnetic field probe system to evaluate the SPF at multiple locations but at a limited number of frequencies, and (c) an ambient field monitoring system for analyzing the long-term ambient field levels. These measurement systems are described in more detail below.

5.1.1. Vector Network Analyzer (VNA) System

This system was used to measure the insertion loss at various locations within the SPF chamber. From this measurement, the Q factor can be determined, thus providing an idea of its reverberation characteristics.

This system consists of: (1) a VNA, (2) a transmitting antenna, (3) a receiving antenna, and (4) an interconnection between both antennas and the VNA. The required frequency coverage was divided into three ranges to best optimize the frequency sampling of the analyzer, as shown in Table 3. These data sets were then processed over a reduced range based on the limited bandwidth of each set of antennas. The resulting frequency bands were (1) low-band—30 MHz to 1 GHz, (2) mid-band—1 GHz to 18 GHz, and (3) high-band—18 to 40 GHz.

We employed precision analog electro-optic links to cover two of the required frequency bands. These links significantly improved the performance over that of conventional microwave cables. The optical links provided improved dynamic range and better immunity from electromagnetic interference [18]. The links were battery-powered and enclosed in a shielded box near the receiving antennas. This was done to minimize any EMI and to simplify antenna movement.

RF coax cables of high quality were used throughout, and a LNA (low noise amplifier) was added to the upper two bands. The estimated minimum dynamic range of this system is 50 dB for low-band, 30 dB for mid-band, and 35 dB for high-band. The configuration of the NIST measurement system for these measurements is shown in Figure 33 and Figure 34.

The antennas used were all commercially available, mechanically stable and designed for medium-power-handling capabilities. For the low-frequency band, discones were used and appropriately sized DRG (dual-ridged guide) horns were used for the two higher bands.

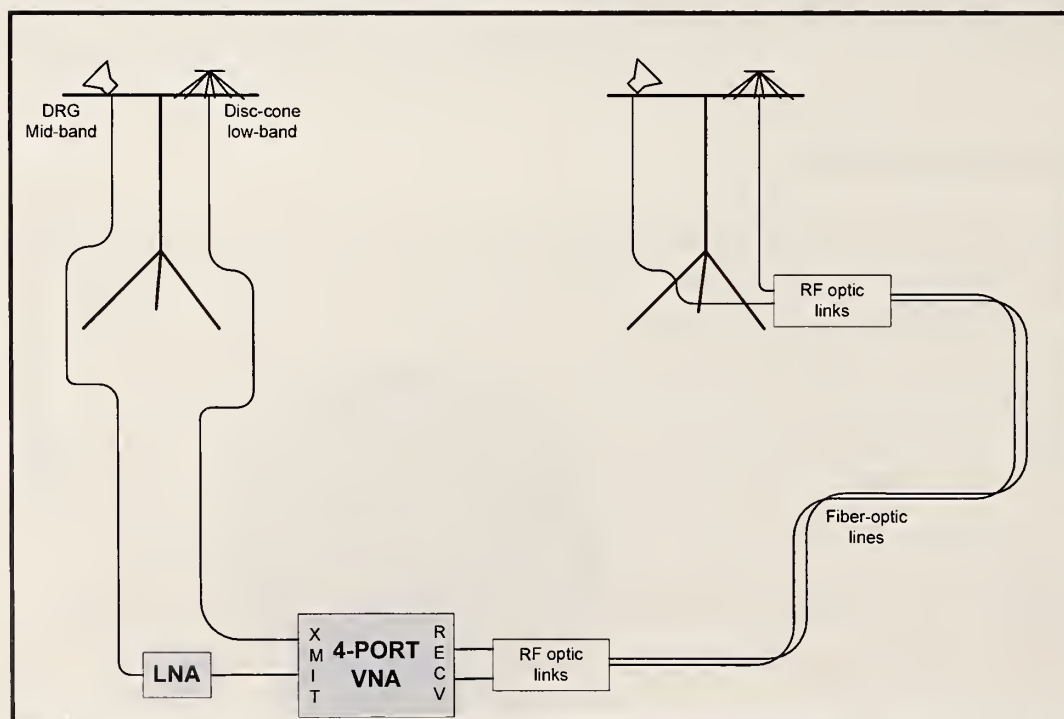


Figure 33. Measurement system used below 18 GHz. Note; two bands are covered with this arrangement.

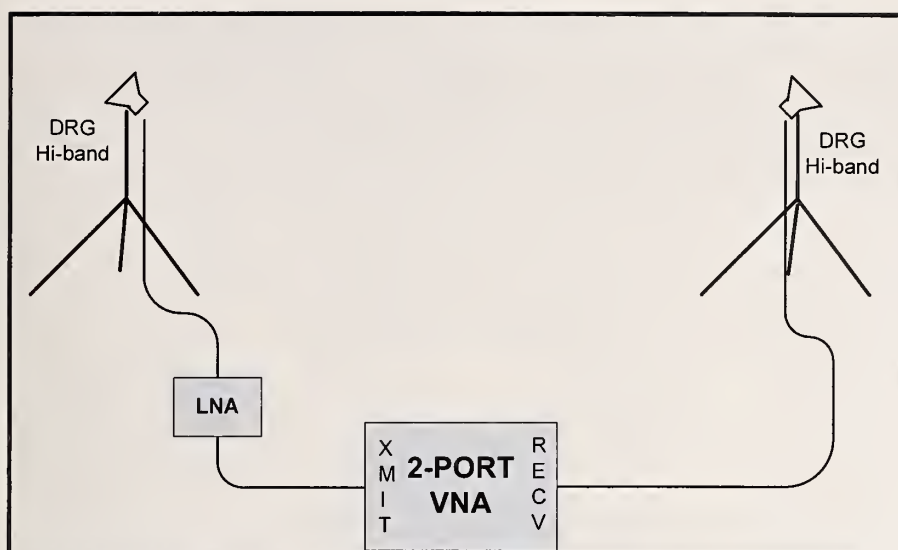


Figure 34. Measurement system used for the high frequency band (18-40 GHz).

The heart of this system is commercially available VNAs that are configured to acquire transmission data (S_{21}). Due to the internal hardware, a VNA is limited to a maximum number of frequencies per sweep, but we developed software that extends the number of data points to much larger values. If more points are than allowed by the VNA, the software subdivides a given frequency range into a user-selected number of sub-bands, each containing a user-selected number of equally divided points. Table 4 contains a summary of points used for each frequency band.

Table 4. Summary of Frequency Bands used.

Frequency Band	Start Freq	Stop Freq	Freq step size	Number of sub- bands	Total pts
Low	500 kHz	2.3 GHz	72 kHz	2	32002
Mid	500 kHz	18.5 GHz	72 kHz	16	256016
High	18 GHz	40 GHz	138 kHz	10	160010

Prior to connecting the cables to the antennas, a VNA calibration was performed to remove systematic transmission effects due to cabling and the frequency and phase variations of the optical transmission link. This procedure calibrates the system with respect to the input of the transmitting and receiving antennas. A known attenuator (30 dB) was used during this process to protect the VNA from the increased signal level due to the gain in system. A direct-connect test was performed prior to the chamber insertion loss measurement and again afterwards, to check system stability and performance. Noise-floor data were obtained by use of a 50 ohm load instead of the transmit antenna.

The frequency data were digitized and transferred to a laptop computer for subsequent data analysis and signal processing. Insertion-loss data were obtained with the transmitting and receiving antennas located at multiple specific locations in the SPF.

5.1.2. Isotropic Electric Field Probe System

The measurement system we employed to measure the electric field consisted of three major components: electric field probes, remote data acquisition, and a shielded enclosure that includes mounts for each field probe. Each of these components was designed by NIST in an effort to facilitate the measurement of an electric field without disturbing the field being measured. Due to the size of the cavity being measured in this application, we chose to suspend the electric field probes inside the cavity. While suspended, the probes would be moved throughout the cavity.

Each field probe was a miniature set of three orthogonal electrically small dipoles (either 5 cm or 8 mm in length depending on the frequency range). The voltage induced by the impinging electric field at the center gap of each dipole was detected using a high-impedance diode and filter circuit. The resulting direct current voltage output of each detector was then transferred to high-impedance digital voltmeters by a length of high-resistance line (carbon impregnated plastic filaments). The available lengths of high-resistance cables were approximately 3 meters. Given the size of the cavity and the cable length restriction, we chose to sample the field probes from within the test cavity in the presence of the electric field being measured. This sampling requirement forced us to design a remote data acquisition system that could sample each probe. Figure 35 shows a photo of the complete system suspended in the cavity.

In the photo, eight probes are mounted along the outer ring of the suspension fixture. In addition to the probes mounted on the outer ring, there is one probe mounted on the cable that suspends the fixture and another mounted along one of the support tubes, as shown in Figure 36, for a total of ten electric field probes mounted on the suspended fixture. The location of each probe – with respect to the mounting fixture – was fixed for the duration of the measurements. Since the SPF is roughly cylindrical, we did not attempt to construct a Cartesian coordinate system for aligning our probes. Instead, below 1 GHz, we attempted to align our probes such that the Z axis of each probe was aligned vertical and parallel with the cylindrical walls, the Y axis was aligned horizontal and tangential to the walls and PVC (polyvinyl chloride) ring, and the X axis was aligned along the radial dimension. Above 1 GHz, the axes of the probes are not as evident, so no attempt was made to align the probes with any specific coordinate system. However, we will continue to refer to the X, Y, and Z components, because this is how the data are stored by the measurement system

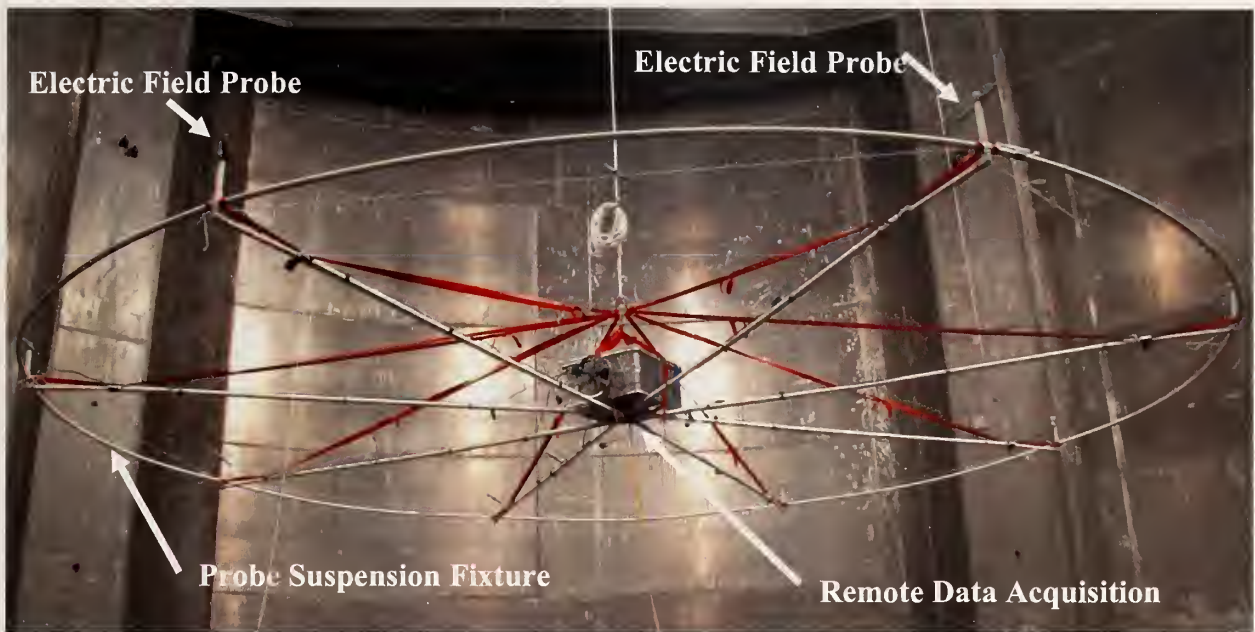


Figure 35. Photo showing the three major components of the measurement system: Electric field probes, remote data acquisition system and the probe suspension fixture.

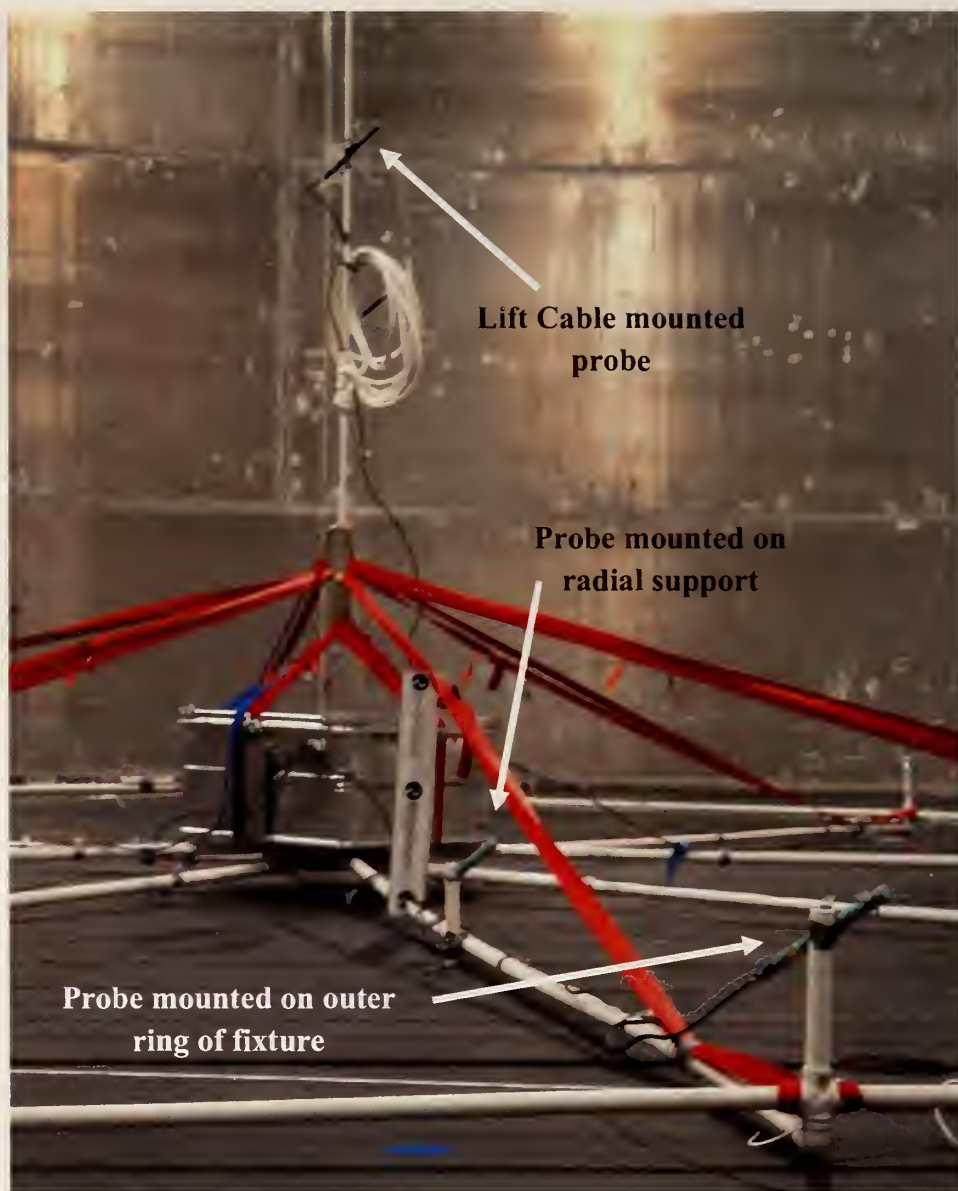


Figure 36. Photo showing two additional probes not mounted on the outer ring of the structure.



Figure 37. Close-up of one of the 5 cm dipole probes. The diode detector is under the small black dot at the center gap of the dipole. The black material is opaque epoxy covering the diode to prevent photo effects in the diode response.

The white ring-like structure on which the probes are mounted is constructed of non-metallic PVC plastic pipe. This plastic ring is suspended (along with the enclosure) by use of the red nylon straps. Along the large outer ring, probes are secured directly to the PVC pipe. Figure 37 is a close-up picture of a 5 cm electric-field probe in its mounting fixture.

The silver enclosure in the centers of Figure 35 and Figure 36 houses the Remote Data Acquisition system designed specifically for this measurement. The enclosure is constructed of solid aluminum plates with a lid that opens for access to the equipment. An EMI gasket was applied to the interface between the enclosure and lid in an effort to prevent electromagnetic energy from entering or escaping the enclosure.

The only protrusions from the remote data acquisition enclosure are two optical-fiber bulkhead feed-throughs that allow the probe cables to connect to the data acquisition equipment. A fiber optic cable also exits the box via one of the feed-throughs. The optical fiber feed-through is designed (not by NIST) to act as a high-pass filter and prevent frequencies below the cutoff from entering or exiting the enclosure (waveguide below cutoff). The cutoff frequency of the feed-through used was approximately 44.2 GHz.

Probe sampling and digitizing is done from within the enclosure. The remote data acquisition system is designed to acquire data directly from each of the ten probes, digitize it, and transmit the information (via a fiber optic cable) to a computer located outside the cavity. Figure 38 shows a photograph and Figure 39 shows a block diagram of the remote data-acquisition system.

This remote data-acquisition system is designed to be as self-contained as possible. The only link the system has to the outside of the chamber was a duplex fiber-optic cable that transfers real-time data to a laptop computer. The fiber optic data transfer is made possible by a USB to fiber optic converter. The converter is essentially “invisible” to the computer, making it seem as though the computer is directly connected to the data-acquisition card. Power for the USB to fiber optic converter comes from an appropriately filtered off-the-shelf DC-DC converter.

The remaining elements of the system are powered from the two 12-volt batteries installed within the enclosure. These two batteries provide enough power to allow for more than 18 hours of constant use. A simple hot-swap circuit was installed to enable one battery to be changed at a time without powering down the system. This circuit also provided short-circuit protection via a diode. Additional short-circuit protection was obtained by using an in-line fuse. One channel of the analog-to-digital converter was dedicated to measuring the battery voltage (after the hot-swap circuit).

Each of the ten probe cables passes through one of the two optical fiber feed-throughs and is connected into a bulkhead plate mounted above the analog-to-digital converter card. A standard probe connector was used on one side of the bulkhead, while the other side breaks out each probe channel into a twisted pair. This twisted pair consists of one signal wire and one ground wire and runs from the bulkhead plate to the terminals of the analog-to-digital converter card. Each twisted pair is wrapped around a small stack of ferrites to reduce any interference that might be present.

The channels of each probe – three channels per probe – are connected to the analog-to-digital converter card. The analog-to-digital converter card is configured to operate in a differential mode where the negative side of the channel is connected to the signal ground and the positive side is connected to the probe signal. Channels 2-31 are dedicated to sampling the probes.

When the voltage of each probe channel is measured, multiple samples are taken in rapid succession. Each sample is immediately sent back via the fiber optic cable to the computer outside the cavity. The number and frequency of samples is intentionally set to reduce noise induced by 60 Hz electrical lines. The most common sampling setup is to average over five line cycles, taking a minimum of 50 samples per line cycle. Sampling in this manner effectively averages out most of the noise induced by 60 Hz electrical lines. If noise at other frequencies is a problem, this sampling process may be repeated and the results averaged again.

Channel “0” of the analog-to-digital converter card is dedicated to measuring a temperature probe. This probe monitors the ambient temperature in the enclosure. Should the temperature change significantly (± 5 C) inside the box, the calibration of the analog-to-digital converter card would become void and would have to be recalibrated.

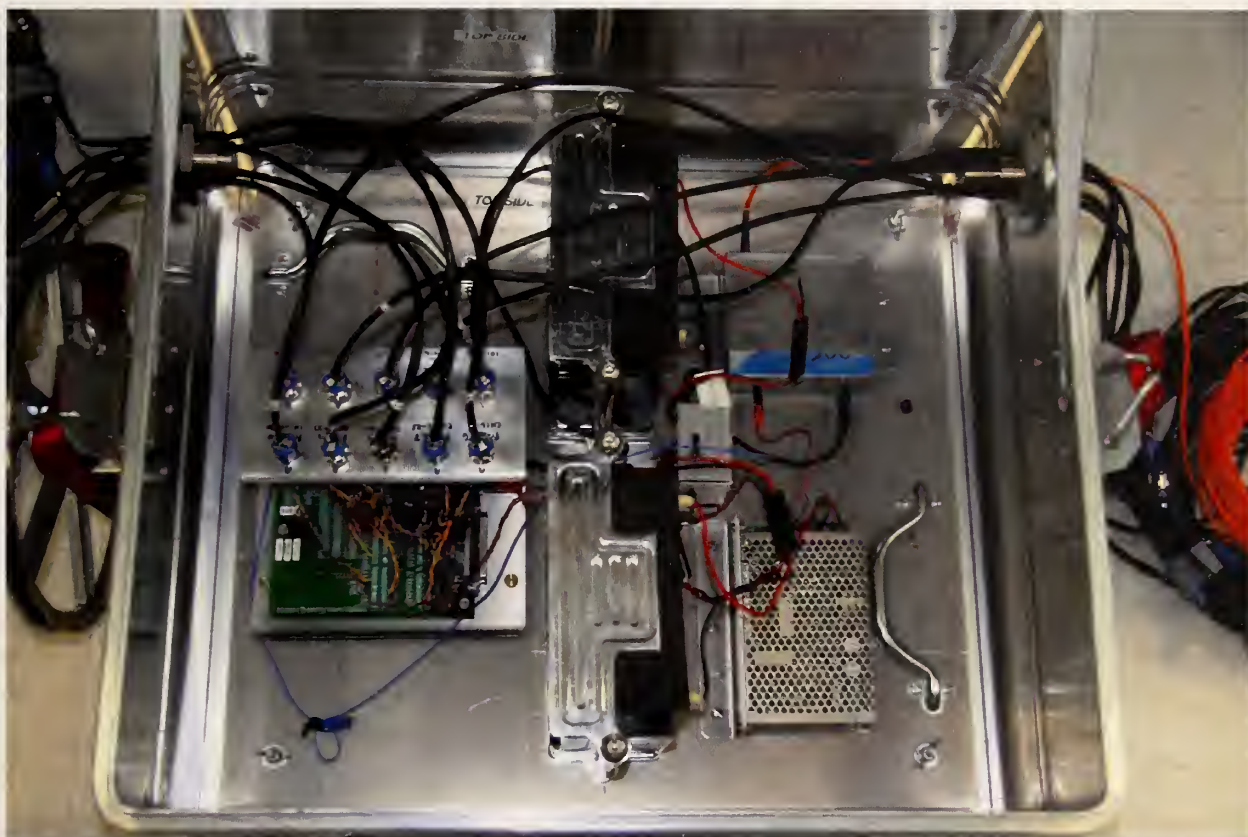


Figure 38. Photo showing DAQ board and probe connections, batteries and power supplies inside the probe electronics box.

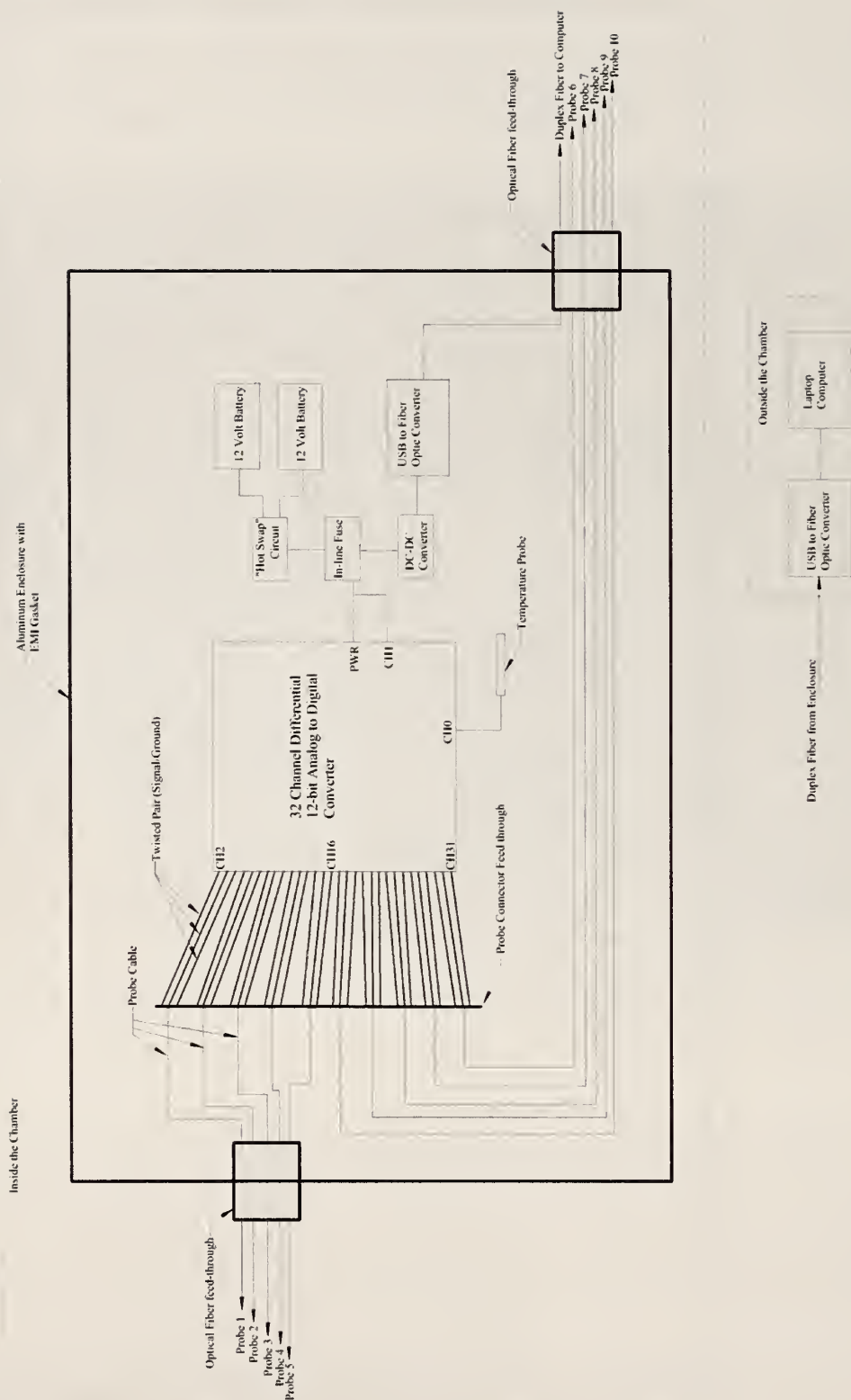


Figure 39. Conceptual block diagram of the remote data-acquisition system. Notice that the diagram is separated into equipment that is inside the chamber and equipment that is outside the chamber.

5.1.3. Ambient Signal Monitoring System

This system consisted of an antenna mounted on a convenient support (tripod usually) and connected to a spectrum analyzer that was in turn controlled by a laptop computer. The initial measurements were performed by two systems, one with a lower-frequency discone antenna designed for 30 MHz -1300 MHz, and the other with a dual-ridged horn antenna designed for 1 GHz -18 GHz. Section 6.4 shows more details on this system. We also used this monitoring arrangement to track signals in the equipment control area between the aluminum inner chamber and the concrete outer shell during the probe tests while we were using the high-powered amplifiers.

5.2. Measurement Objectives

The tasks before us were to evaluate the electromagnetic characteristics of the SPF as an empty chamber and to characterize the effects caused by the introduction of the floor assembly of the cryogenic shroud (cryo-floor), which was a square approximately 12 m on a side. The concern was that the carbon-based paint on the surface of the metal cryo-floor would electrically load the chamber excessively. After doing a series of tests (described below) on the totally empty chamber the cryo-floor was wheeled into place at the center of the chamber. There were more extensive tests carried out with the cryo-floor in place, because this will be the baseline configuration for the actual E3 evaluation. The plan is to have the spacecraft setting on the cryo-floor during the E3 testing.

The process of “evaluating” this chamber posed some challenging questions and hurdles. The geometry suggested that we may see issues with whispering-gallery modes, caustics, and other undesirable (non-uniform) characteristics in the field structure within the chamber. The size is such that we knew that our best efforts would yield only a very sparse sampling of the volume and would limit (or eliminate) our ability to mechanically stir, as is done in a typical room-sized reverberation chamber. We were able to sample a reasonable number of positions near the floor by use of antenna supports of various heights and to sample along a vertical line to near the top of the chamber dome, plus another vertical line about four meters off-center. The vertical scan was limited to frequencies below 18 GHz, because the 18-40 GHz equipment was not portable enough to lift off the floor. While this sparse sampling may be inadequate to detect fine structure in the fields, we were pleasantly surprised to see very good uniformity throughout the chamber, based on these samples. We should also note that all VNA and probe measurements were performed with no personnel in the chamber. The measurement equipment was controlled remotely via fiber-optic systems or a time delay.

There were limited options for positioning the measurement hardware in this large cavity. We were able to position antennas either at various positions around the floor at three heights (1.68 m with tripods, and 2.6 m and 6 m with crank-up masts) or suspend the receiving system from a rope at the center of the chamber and scan vertically. There were more opportunities to use the crank-up masts on the floor while the chamber was empty (section 5.2.1). Once the cryo-floor was positioned, the masts were used around the perimeter of the cryo-floor and a tripod was used on the cryo-floor to prevent scratching or damage to the surface (section 5.2.2). The vertical scan system allowed us to position our receiving antennas from floor level to well into the dome (30+ meters above the floor). This capability was made possible by the personnel at the NASA facility. They had fastened a high-capacity electric winch to the floor at the west end of the SPF. Attached to the winch was a special synthetic rope (zero stretch) that passed through a pulley directly above the winch and from there to a pulley at the apex of the dome. This system provided a very convenient method to hoist measurement equipment vertically on the center line of the chamber. The electrical supply to the winch was removed prior to each radio-frequency test to minimize interference. The winch braking action was sufficient to prevent movement of the load when power was removed. An additional feature was a set of pulleys and a rope installed on the southeast wall that allowed the vertical axis to be offset from the centerline by a few meters such that a vertical scan could be done near the projected outer diameter of the future spacecraft. This arrangement worked quite well.

5.2.1. Ground Level Test points in the Empty Chamber

The experiments in the empty chamber were done using the vector network analyzer (VNA) system to measure the insertion loss between two antennas (section 5.1.1). The cable and system losses were removed via a response calibration measurement (directly connecting the two cable ends via a precision barrel). We used adjustable antenna supports (masts) to position the antennas at two different heights above the floor, typically 2.36 m and 6.0 m. The supports held the two antennas about 2 m apart on a boom with adjustable mounts to vary the polarization and direction of the antennas. We mounted a low-frequency (30 MHz -1300 MHz) discone at one end and a high-frequency horn (1 GHz-18 GHz) on the other. With this arrangement we were able to sweep the entire frequency range up to 18 GHz at the same time, by use of one set of two VNA ports for each of the low-band and high-band antennas.



Figure 40. Initial attenuation measurements near the center of the chamber with antennas' polarization matched and aligned to bore sight.

The initial set of measurements was made with the antennas near the center of the chamber and each pair polarization-matched and aligned on bore sight to maximize the direct coupling, as shown in Figure 40. The schematic of the test positions is shown in Figure 41. When this configuration is used in an environment that has low to moderate Q , the direct path signal can easily be isolated from the reflections by use of Fourier transforms and time-gating. This is useful to establish baseline data on the performance of the antennas. However in this chamber, because of the high Q and the need for exorbitantly close frequency spacing, we were not able to do time-gating. Hence, these tests were used to check and adjust the system settings, verify software, and get a first look at the chamber performance. These data then became part of the overall database for the chamber, but are not presented in this report.

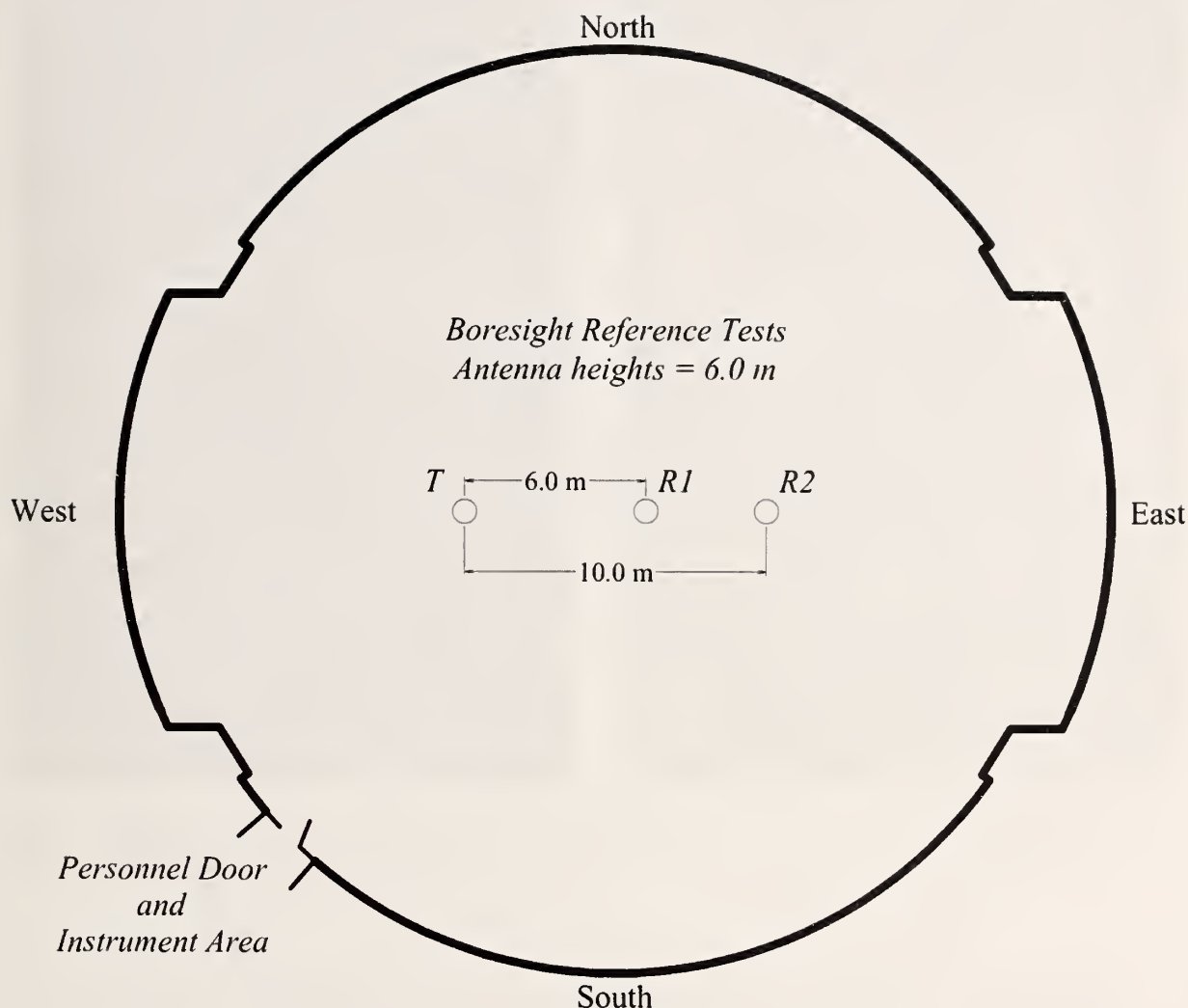


Figure 41. Plan view of the antenna positions for the initial tests. (T represents the transmit location, $R1$ and $R2$ indicate the receive antenna location)

The following experiments were performed at two heights and at the test locations shown in Figure 42. The antennas were deliberately aligned so as to minimize any direct-path coupling, cross-polarized and directed (in the case of the horns) away from each other. With the transmitting antenna placed in position $T1$, the receiving antennas were placed in positions $P1$ through $P5$ and at heights of both 2.36 m and 6.0 m, for a total of 10 measurements. The transmitter was then moved to position $T2$, and the receiving antenna was placed in position $P5$ at a height of 6.0 m, and then to positions $P6$ through $P8$ and both heights for a total of seven additional measurements. The photographs in Figure 43 show examples of the test arrangement.

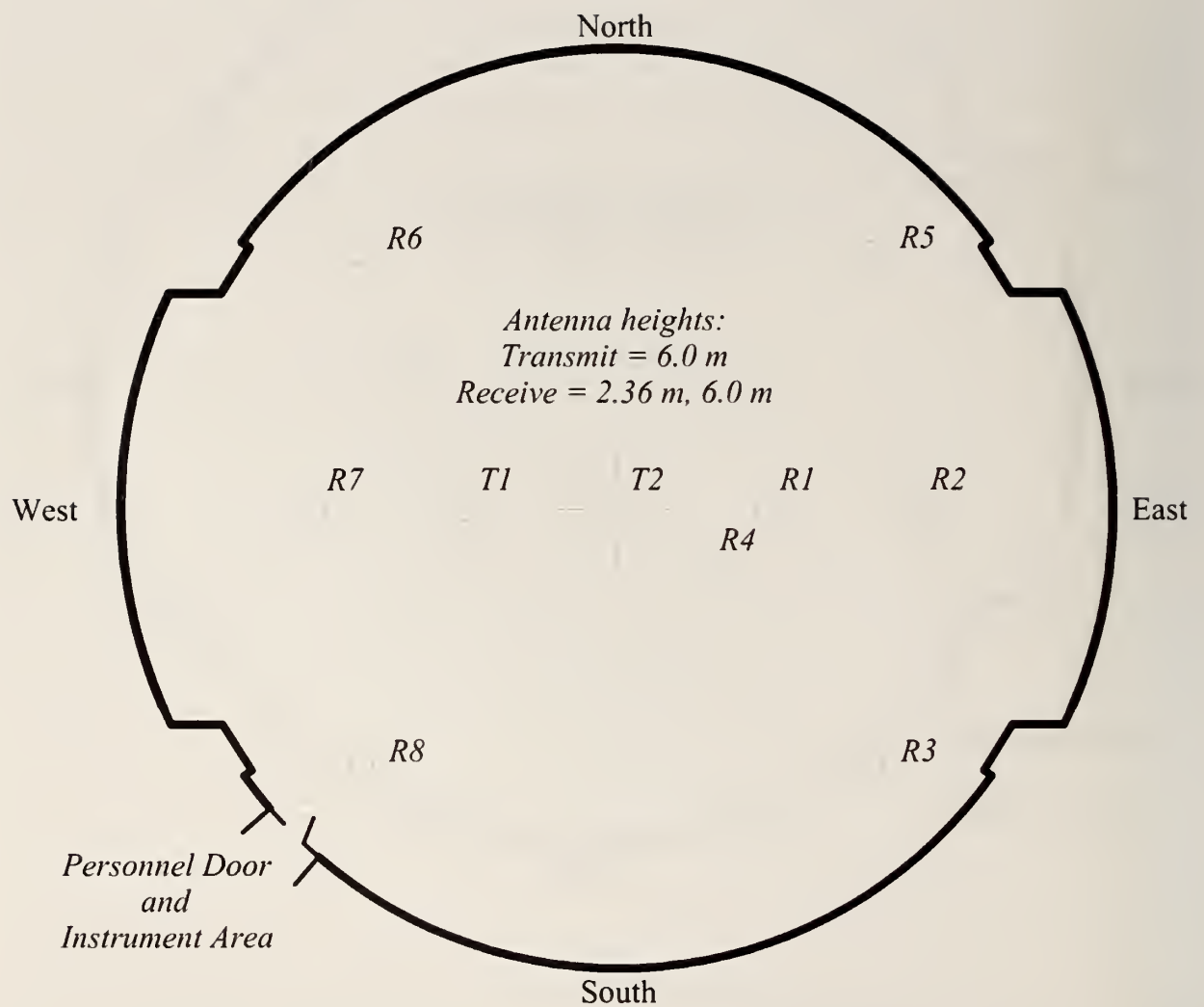


Figure 42. Plan view of measurement points for the low- and mid-band frequency ranges. ($T1$ and $T2$ are transmitting locations and R_i are receiving locations).



Figure 43. Two examples of the test configuration used to position the antennas during the empty chamber tests at the low- and mid-band frequencies.

The higher-frequency band from 18 GHz – 40 GHz required that we use a different analyzer, antennas, and supports. The optical links (see section 5.2.1) were not usable in this frequency range, so the antennas were directly connected by low-loss coaxial cables about 2 m long. This means, of course, that the separation of the two antennas could be no more than the length of the cables. Since the small horn antennas were strongly directional, we could easily minimize the direct coupling by simply pointing the antennas in appropriate directions. The antennas were held on fiber tripods at a height of 2.0 m. We were able to sample the fields only in the floor area, due to the equipment constraints. Figure 44 shows the test points (a total of 12 configurations) chosen on the floor for this frequency band, and the photos in Figure 45 show the physical arrangement of the equipment and antennas. The transmitting and receiving antennas were randomly positioned (direction and polarization) for each test position, with the requirement that the antennas are generally pointing away from each other to minimize direct coupling.

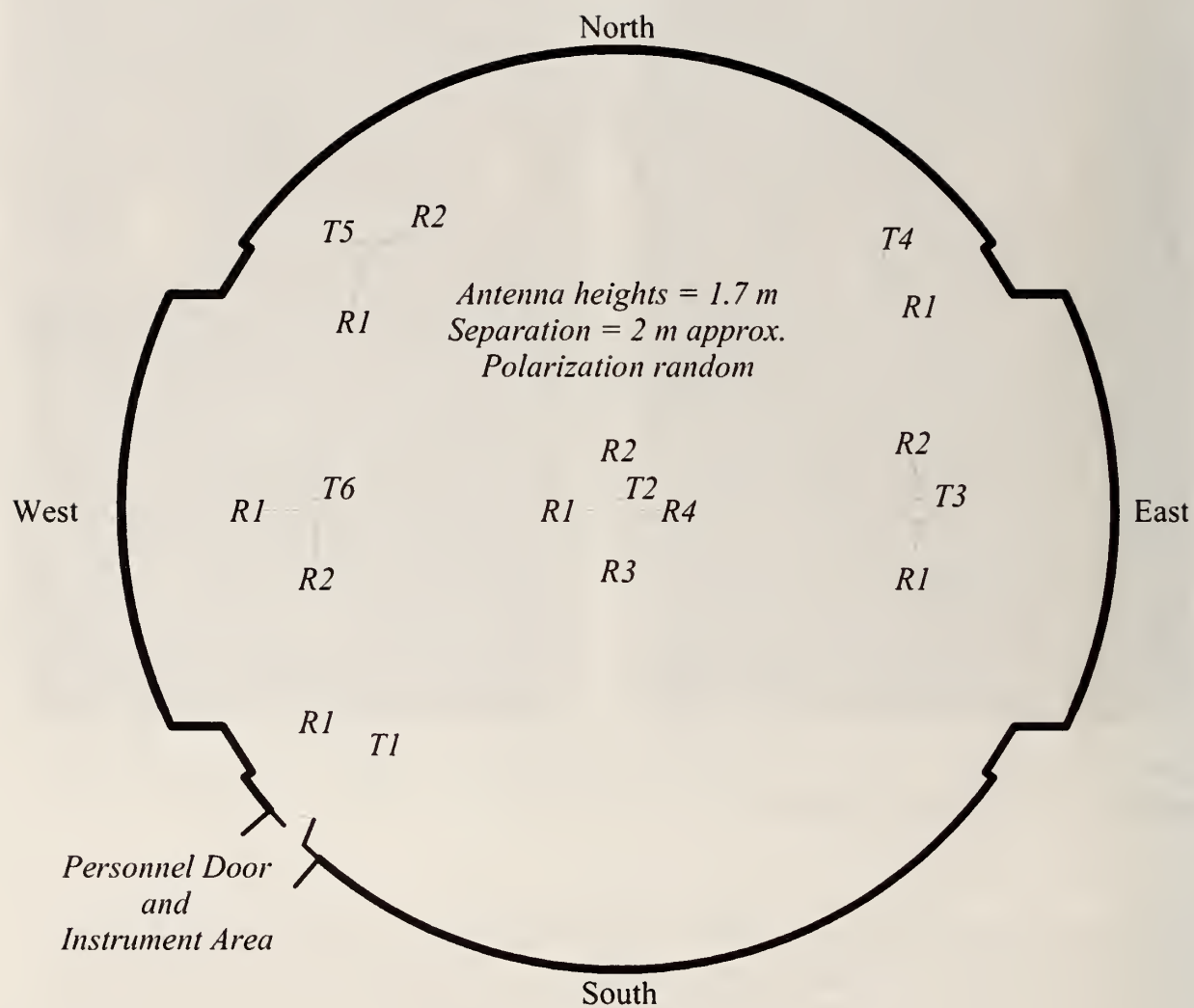


Figure 44. A plan view showing the approximate positions of the 18 GHz-40 GHz test equipment in the empty chamber. (*T* indicates the test point and location of the transmitting antenna, while *R* indicates sequential positions of the receiving antenna.)



Figure 45. Photos of 18 GHz-40GHz setup.

5.2.2. Ground Level test points with Cryoshroud Floor

The floor to the cryoshroud assembly was rolled into the SPF chamber following the tests described in the previous section. The photo in Figure 46 shows the cryo-floor after it is positioned in the center of the chamber prior to closing the large aluminum door. We attempted to repeat similar test points in the chamber with the cryo-floor in place as was done in the empty chamber. However, we chose not to put the large antenna supports on top of the cryo-floor, for safety reasons and to prevent any possible damage to the floor. Rather, we used the fiber tripods to hold the individual receiving antennas at a height of about 1.7 m above the cryo-floor deck.



Figure 46. The cryo-floor assembly is positioned in the center of the SPF aluminum chamber prior to closing the large access door.

The cryo-floor assembly remained in the chamber for all the subsequent tests. The first set of measurements was in the 18 GHz-40 GHz band, because the system was still configured and ready from the previous measurements. The test positions in the chamber for this band were more limited, due to the presence of the cryo-floor assembly and the short cables. We decided not to lift the analyzer and other equipment onto the cryo-floor, for safety reasons and to avoid possible damage to the analyzer. The resulting five test positions are shown in Figure 47.

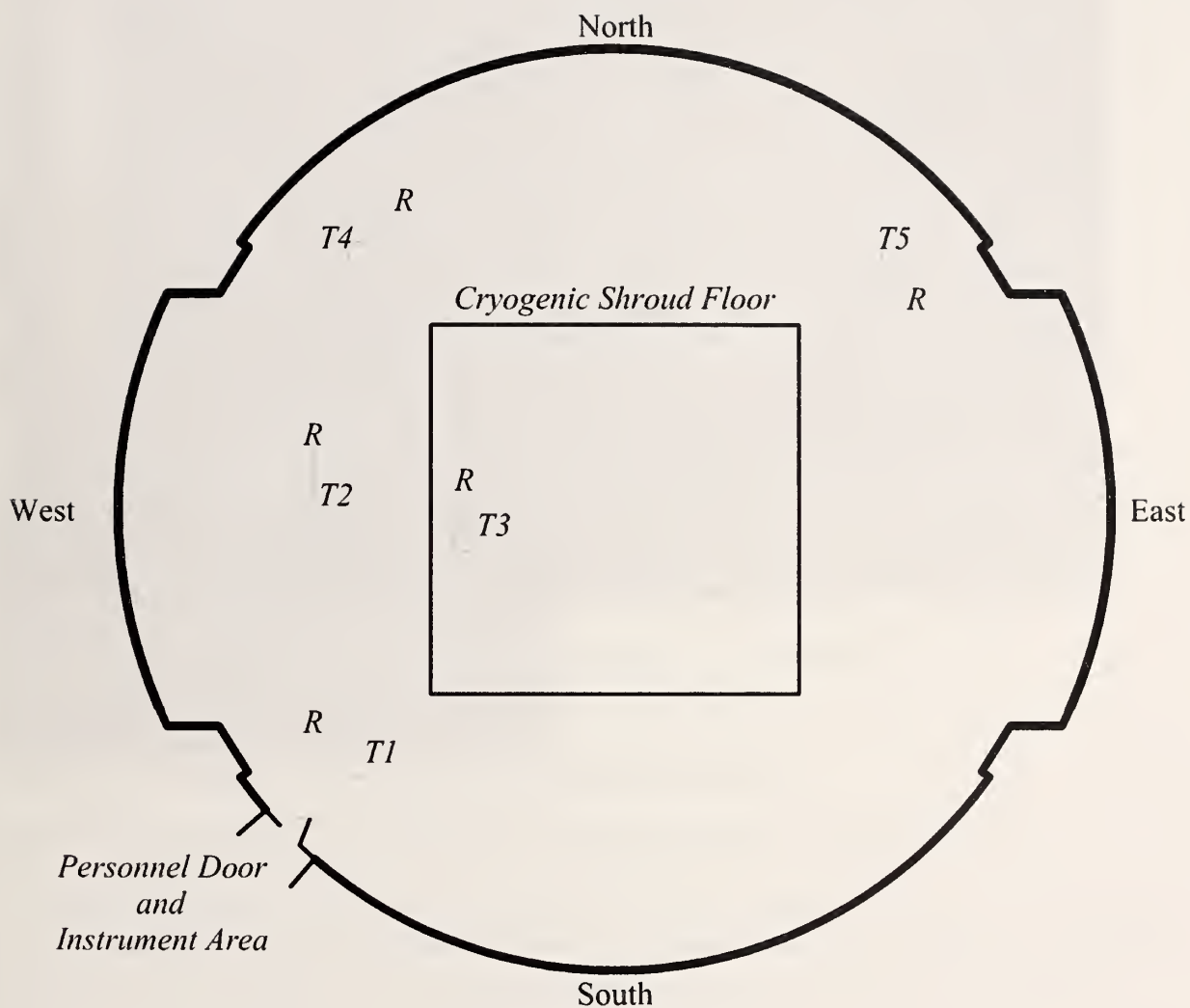


Figure 47. Test locations for the 18 GHz-40 GHz band with cryo-floor in the chamber. (T_i indicates approximate location of transmitting antenna and R the location of receiving antenna)



Figure 48. Photograph of 18 GHz-40 GHz band test point *R5* of Figure 47.



Figure 49. Photograph of 18 GHz-40 GHz band test point *R3* in Figure 47.

Figure 48 and Figure 49 show two of the test positions for the 18 GHz-40 GHz band.

We then set up the low- and mid-band system again and proceeded to replicate as many ground level test positions as possible. Figure 50 shows a schematic of the approximate locations of the test antennas in the chamber. The transmit antenna was placed in two of the six positions marked on Figure 50, and the receiving antennas were placed in each of the other five locations. For each receiving location measurements were made at two heights: 2.36 m and 6.0 m, for a total of 20 floor positions around the cryo-floor. We next placed the receiving antennas on tripods for the tests conducted on the cryo-floor assembly. Figure 51 shows a schematic of the approximate locations of the test antennas in the chamber, and the photographs in Figure 52 show a couple of different test positions at ground level with the antenna masts. Measurements were performed for the nine configurations shown in Figure 51 plus three repeated configurations, for a total of 12 configurations.

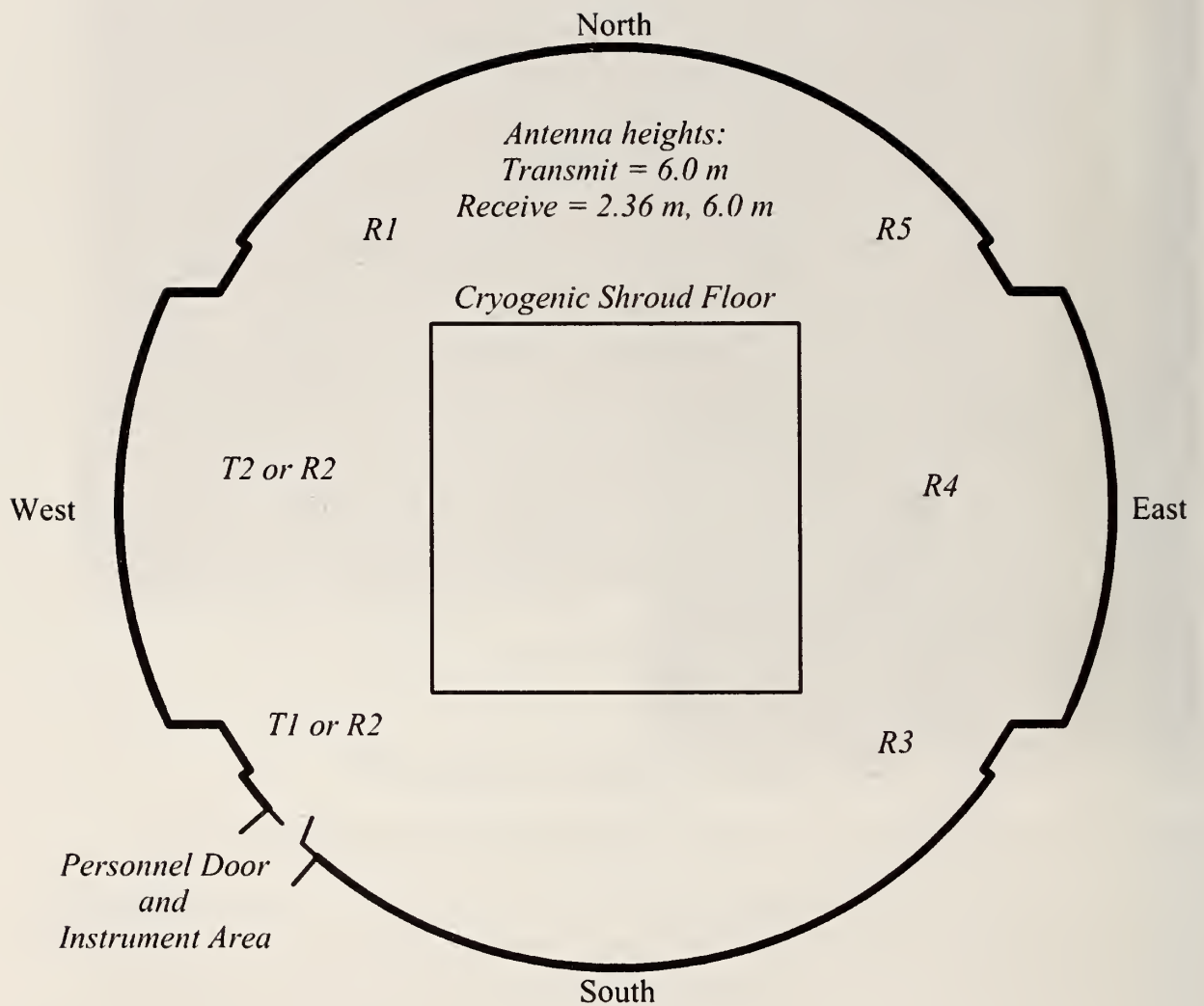


Figure 50. Approximate test locations on the chamber floor for the low- and mid-band frequencies with the transmit positions (*T*) located on the center line near the west door. Tests were also performed with the transmit antenna located near the personnel door and the receive location (*R2*) near the west door.

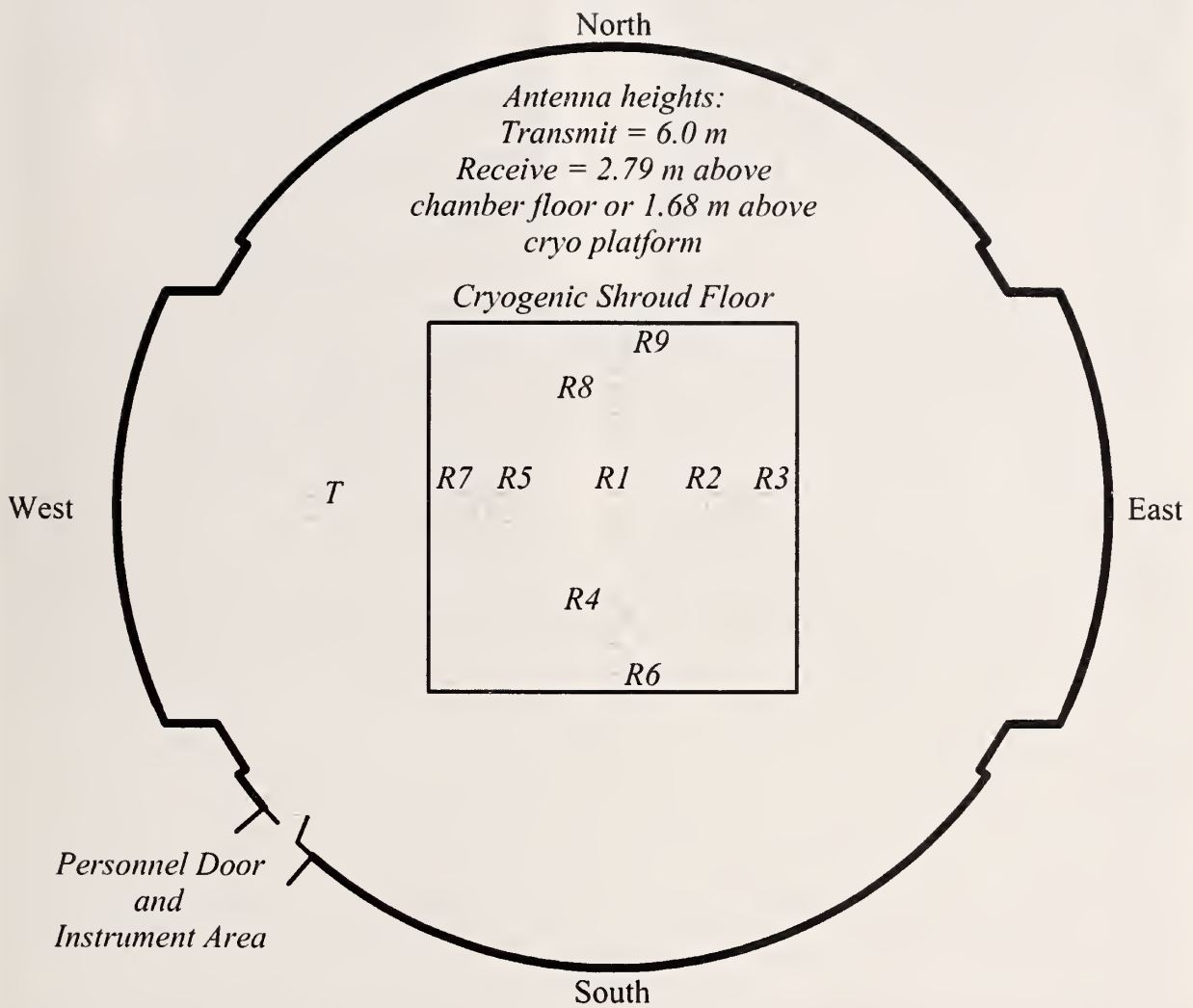


Figure 51. Approximate test locations with the individual receive antennas mounted on the small tripods on the cryo-floor. The transmit antennas were set 6 m above the chamber floor near the west door. These positions were repeated so that both the low (<1 GHz) and mid (1 GHz-18 GHz) bands covered all positions on the cryo-floor.



Figure 52. Photographs of typical transmit and receive antenna positions while testing at positions on the chamber floor.

5.2.3. Tests along the vertical axis by use of the VNA and Probe Systems

For the vertical sampling tests, the receive antennas were removed from the mast and placed on the RF/fiber link box. A rope-and-pulley system was used to raise and lower this box along the vertical centerline. Figure 53 is a sample photo during the vertical sampling tests, and it shows the antennas, box and ropes. The transmit antennas were placed at location *T1* in Figure 50, and the receive antennas were moved to a fixed height. Then insertion loss data were obtained at multiple pre-determined receive heights summarized in Table 5. When no cryo-floor was present, we had a total of eight measurements, including one repeated measurement at 6 m. The rope was then offset by approximately 4 m so that a series of vertical measurements could be made above position *R4* shown in Figure 42, giving four additional measurements. Once the cryo-floor was moved into the chamber, these vertical measurements were repeated, but with approximately twice the number of heights for a total of 12 measurements along the centerline and ten measurements offset from the centerline. Similar vertical scans were performed by use of the probe system as shown in Figure 54, although no probe measurements were made in the empty chamber or with the rope offset from the centerline.

Table 5. Measurement heights for vertical scans.

Measurement Condition	Measurement Height Above Floor (m)
Insertion loss, empty chamber, centerline	3, 6, 10, 15, 20, 25, 30, +repeat @ 6
Insertion loss, empty chamber, offset	3, 6, 15, 20
Insertion loss, with cryo-floor, centerline	3, 6, 8, 10, 12.5, 15, 17.5, 20, 22.5, 25, 27.5, 30
Insertion loss, with cryo-floor, centerline	3, 6, 8, 10, 12.5, 15, 17.5, 20, 22.5, 24
Probe system	3, 6, 8, 10, 12.5, 15, 17.5, 20, 22.5, 25, 27.5, 30



Figure 53. Representative photo of the vertical scan setup.

6. Experimental Data

As discussed in section 5, measurements were performed by use of two measurement systems: the VNA system and the isotropic field probe system. The majority of our measurements were performed by use of the system that could provide the most information in the shortest time—the Vector Network Analyzer system. This system was able to provide measurements of coupling between two antennas at a large number of frequencies (tens of thousands) for whatever positions the transmitting and receiving antennas were placed. By averaging the measurements

over a number of frequencies, it was possible to estimate the variation in coupling that would be expected for any pair of antennas placed in any locations in the chamber. This approach allowed us to gather a large quantity of data in a short period and was used to generate the vast majority of data described in this report. However, this system was not well equipped to provide measurements of field at a large number of locations (especially in and around the expected locations of test devices). For these measurements we used the isotropic field probe system. This system was much slower than the VNA system and was therefore used only for evaluating (a) approximate field levels for a given input power, (b) field uniformity, and (c) the suitability of using the SPF as a reverberation chamber as described by measurement standards[4][6]. These measurements required the use of a paddle that, ideally, should have been large relative to at least the smallest dimension of the chamber [14]. Unfortunately, we also needed a paddle that could be easily shipped, and our resulting paddle had a diameter of approximately 1.4 m. The paddle used for these measurements is shown in Figure 54. This paddle was obviously insufficient, given the size of the chamber. However, we hoped that by directing the transmitting antenna into the paddle, we could approximate the effect of moving the transmitting antenna to multiple locations. While this approach will not indicate how well this chamber can perform given a large paddle, we hoped that the results would be good enough to compare to measurements based on reverberation chamber standards that require a minimum of 12 paddle positions. For this purpose, a minimalistic paddle may be sufficient.

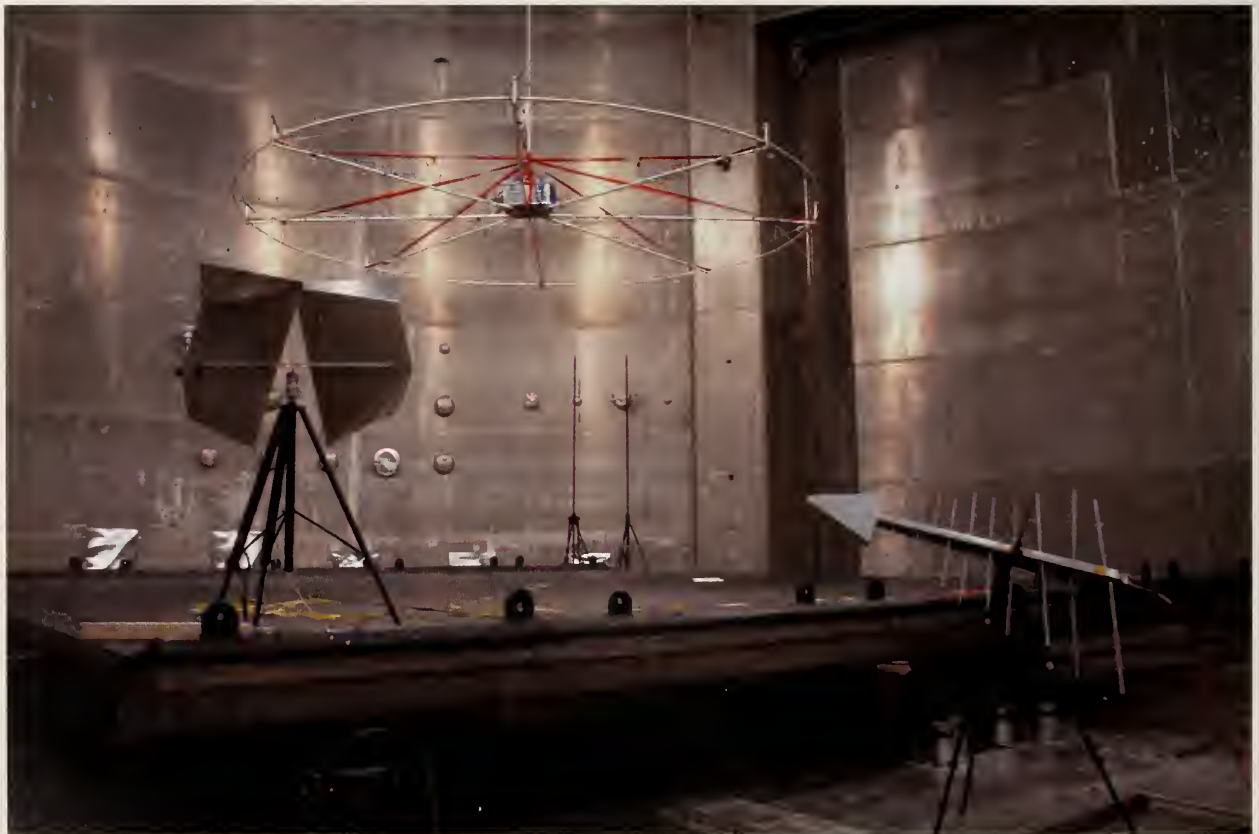


Figure 54. Paddle used for probe system measurements.

6.1. *Basic VNA Measurement Approach*

Our basic measurement approach using a VNA was similar to that given in [14], with two exceptions: the optical link used in these measurements allowed measurement of the transmission coefficient S_{21} only (reflection coefficients S_{11} and S_{22} and the reverse transmission coefficient S_{12} were not available), and samples were taken as a function of frequency rather than paddle position. The lack of the reverse transmission coefficient is not a problem, because S_{12} and S_{21} should be the same [14], but the missing reflection coefficients require some additional measurements and processing, as described below. Regarding the use of frequency sampling, as long as the chamber characteristics are relatively flat over the averaging bandwidth and the bandwidth of a mode in the chamber is narrow relative to the frequency spacing of the measurement system, the two approaches should give similar results. For simplicity, we will refer to $|S_{21}|^2$ as the insertion loss measured between the input port of the transmitting antenna and the output port of the receiving antenna.

To illustrate how measured data were processed, we will present a detailed example for the first set of low-frequency data described in Figure 42, with the transmitting antenna at point T1 at a height of 6 m, and the receiving antenna at point P1 at a height of 2.36 m. Processing procedures at all other locations, configurations, and frequencies were identical, except as noted. For the results we present below, we averaged over 141 points, or an averaging bandwidth of approximately 10 MHz. To estimate the average insertion loss at a given frequency, we average the value at that frequency with the 70 points below and above. An example of a single frequency sweep, along with its 141 point moving average, is shown in Figure 55.

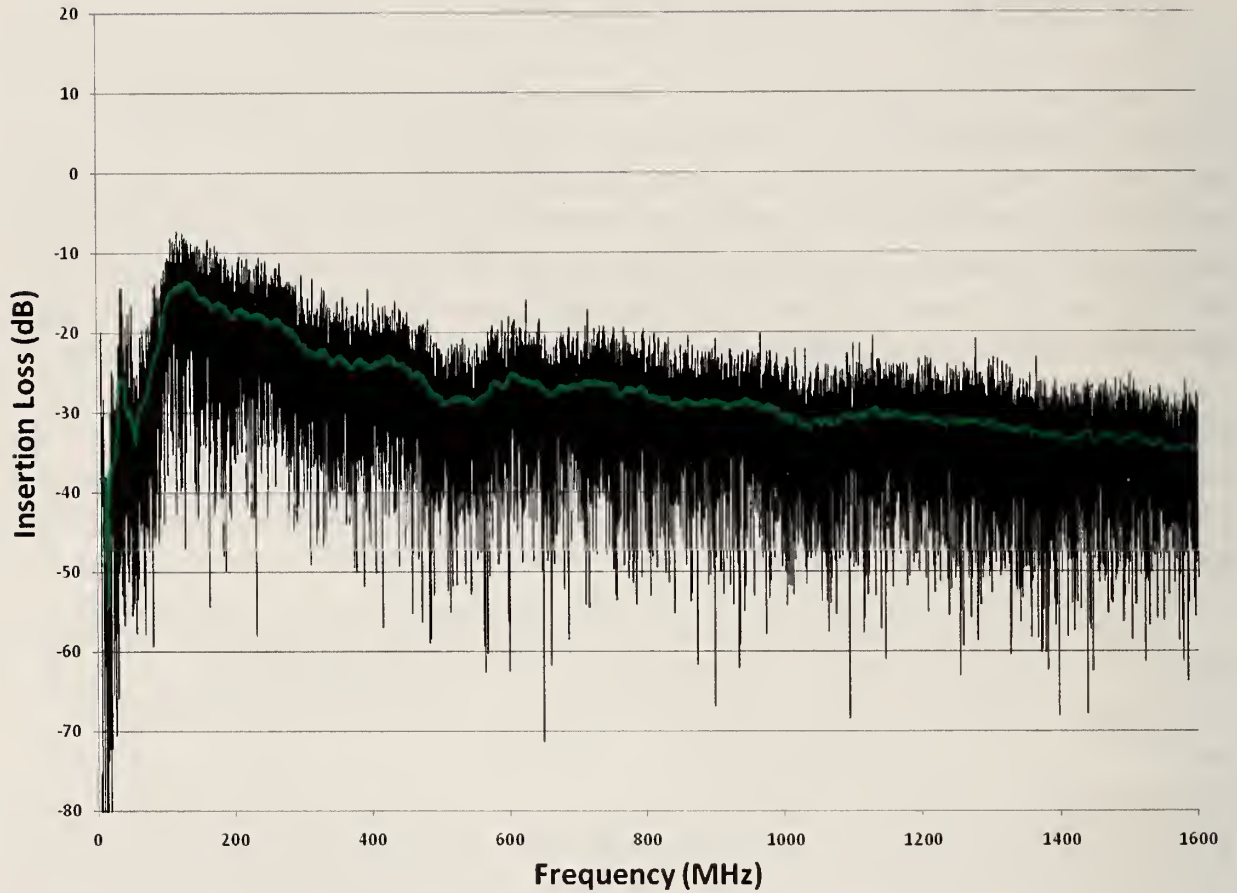


Figure 55. Raw low-band frequency sweep along with 141 point (10 MHz) moving average.

Chamber responses are typically smooth with frequency, so the large roll-off below 100 MHz and the smaller fluctuations from 300 MHz to 400 MHz, from 450 MHz to 600 MHz, near 650 MHz, and from 1 GHz to 1.1 GHz are most likely due to poor impedance-matching of the transmitting and/or receiving antennas at these frequencies. The reflection coefficients of both the transmitting and receiving antennas were evaluated on the NIST Open Area Test Site, and a typical result is shown in Figure 56. The measured reflection coefficient is high (greater than 0.2) in each of the frequency ranges described above, as expected. The reflection coefficient is especially high (greater than 0.9) below 70 MHz, and uncertainties will be large for these frequencies (details provided later).

Since we are interested in the characteristics of the SPF and not the combination of SPF and our antennas, we correct for the mismatch as was done in [14]. For both the transmitting and receiving antennas, S_{11} was measured and a correction factor of $\frac{1}{1-|S_{11}|^2}$ was computed and applied for each antenna.

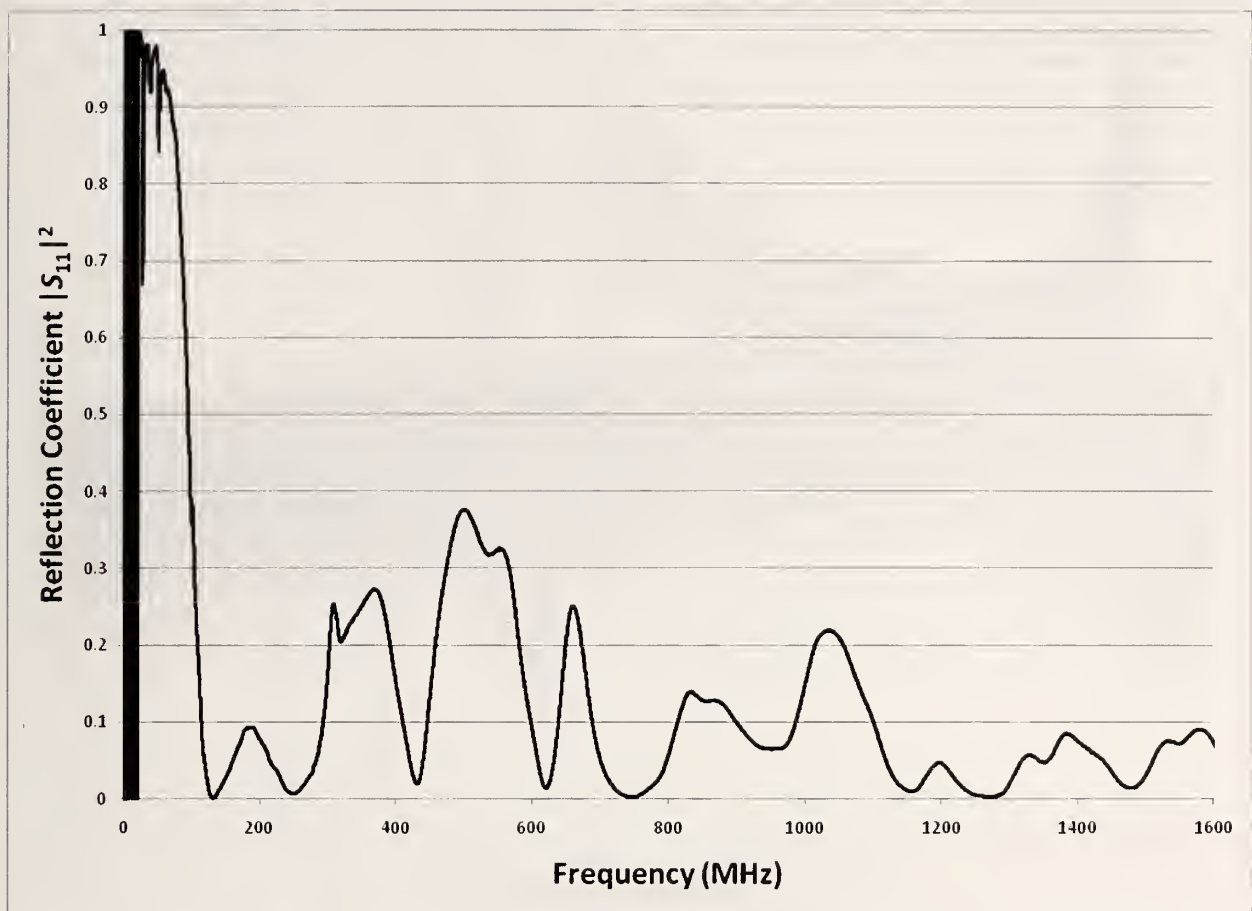


Figure 56. Typical reflection coefficient for low-frequency antennas.

Figure 57 shows the same data from Figure 55 but with mismatch correction factors applied. Overall the data appear better behaved, with the exception of the apparent gain below 40 MHz. This is caused by very large reflection coefficients (near unity) that result in very large correction factors. The same data are also presented on a logarithmic frequency scale in Figure 58. Such a scale is useful when presenting data up to 40 GHz. In this figure it is apparent that frequency averaging is not very useful at low frequencies, where there are multiple problems: low mode density, large corrections due to poorly matched antennas, and large variations over the averaging bandwidth. For these reasons, we will focus on the behavior of the SPF above 70 MHz. A more thorough investigation using antennas designed for lower frequencies and large paddles is recommended to determine the behavior of the SPF below 70 MHz.

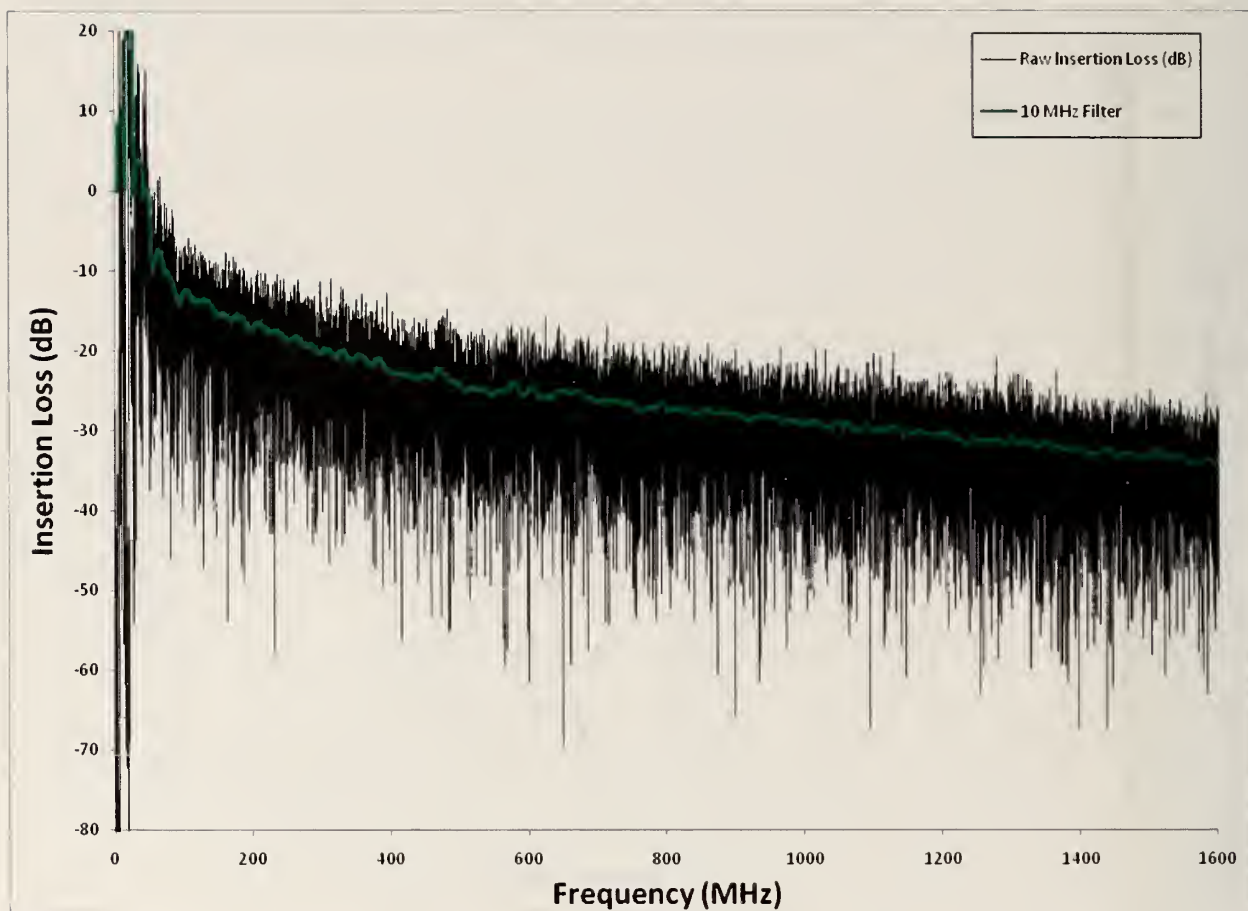


Figure 57. Insertion loss corrected for antenna mismatches.

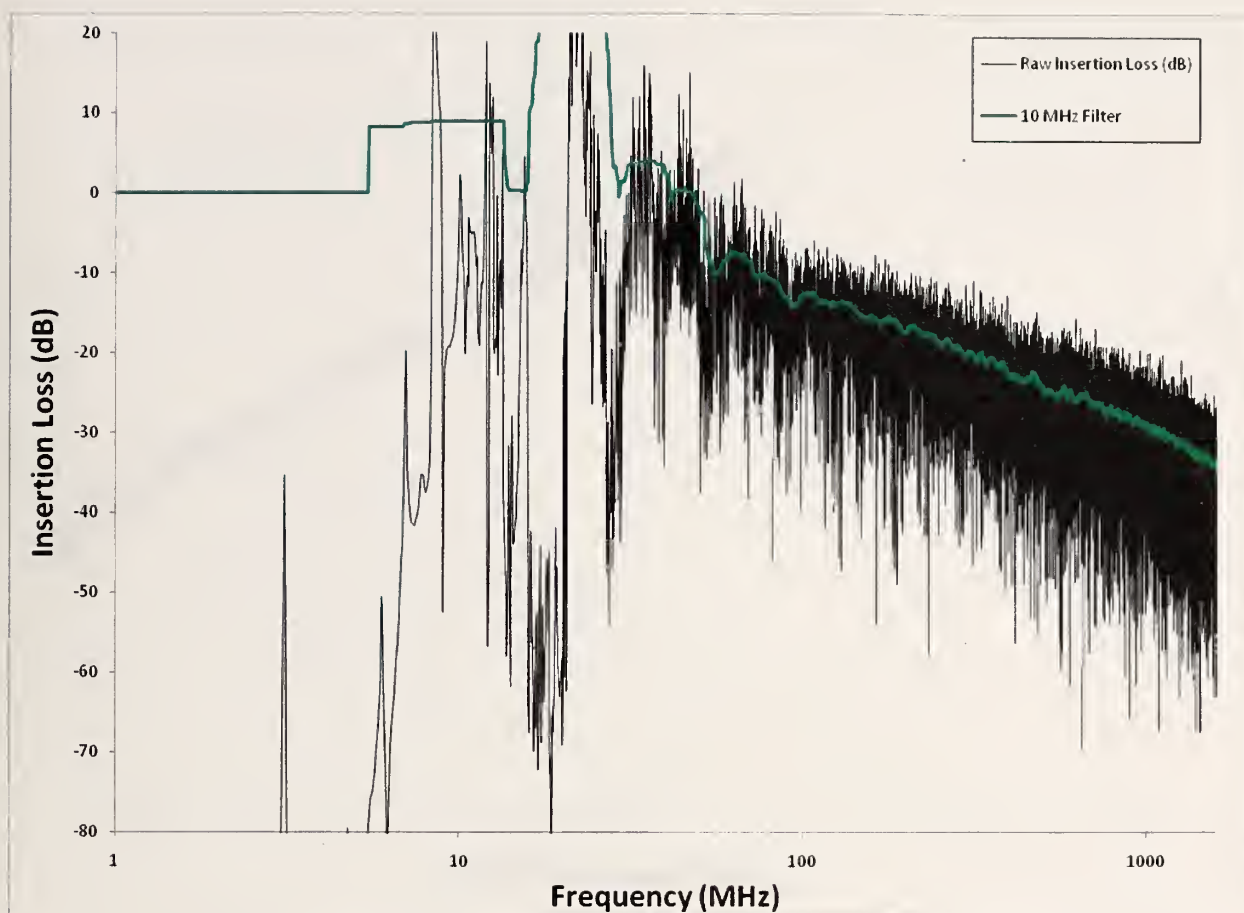


Figure 58. Corrected insertion loss with frequency on a logarithmic scale.

6.1.1. Low-band Results

There were a total of 29 measurements (17 floor, 8 center vertical, and 4 offset vertical measurements combined) performed in the empty SPF, and these are summarized in Figure 59. Figure 60 summarizes the 54 measurements (20 floor, 12 on the cryo-floor, 12 center vertical, and 10 offset vertical) with the cryo-floor present. The overall agreement is much better than expected, with a standard deviation of approximately 0.4 dB, which is very close to what we would expect from an ideal chamber with 141 samples, which is approximately 0.36 dB.

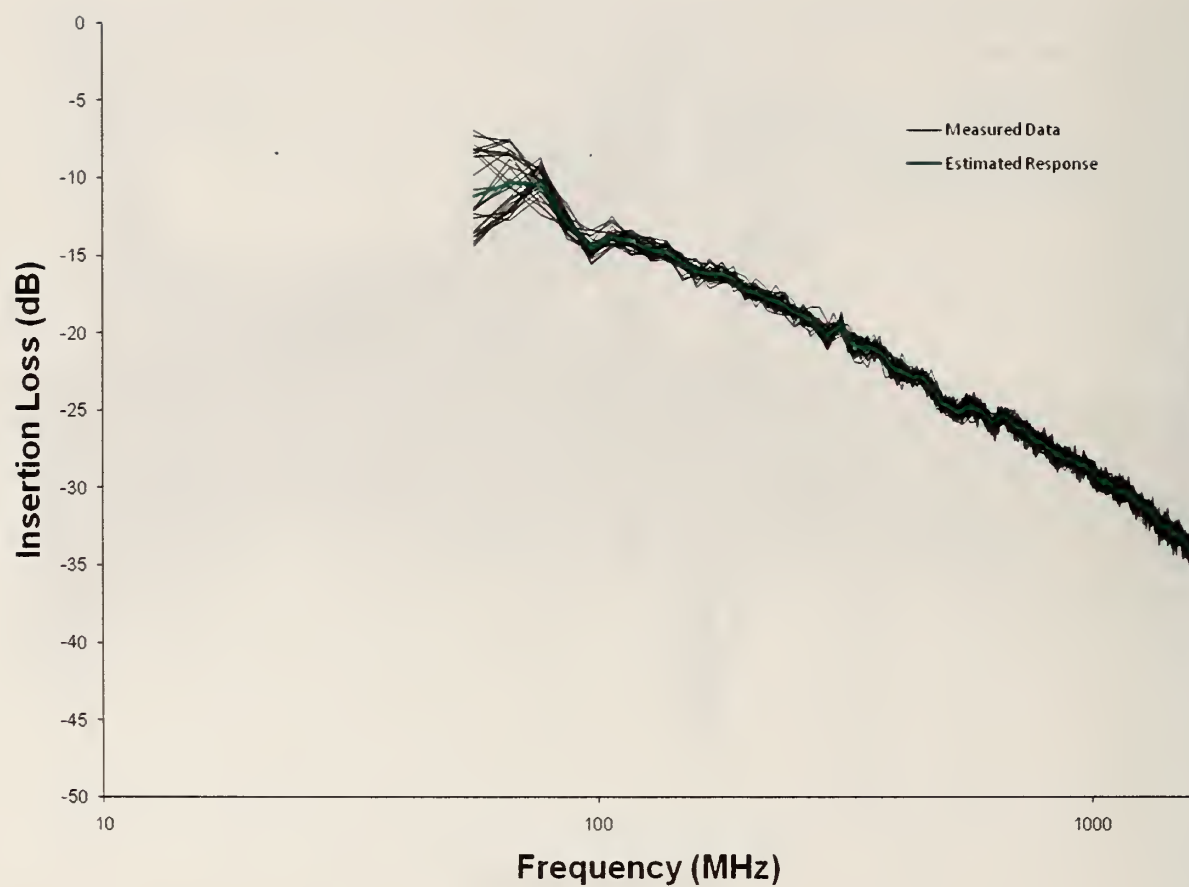


Figure 59. Frequency-averaged results from 29 measurements in the empty SPF, and the average of all measurements, which gives the estimated response of the chamber.

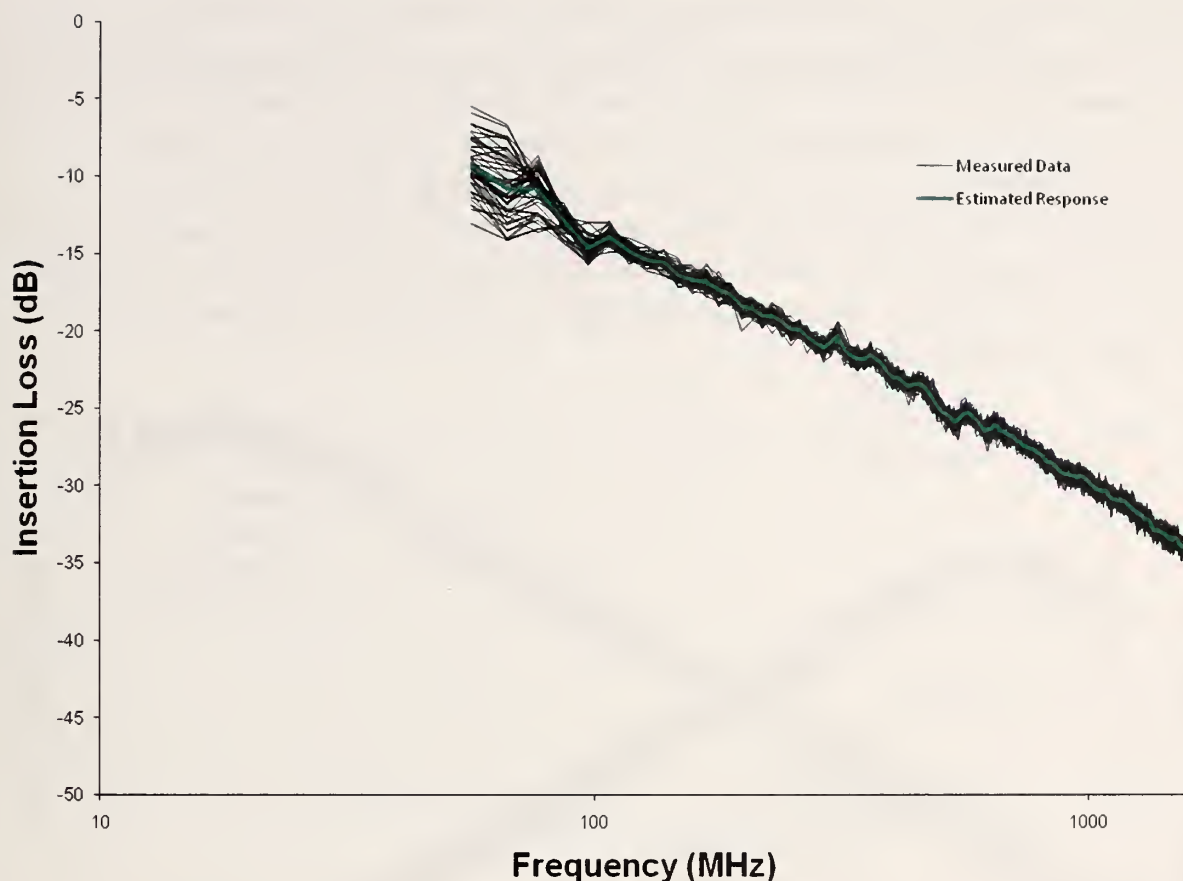


Figure 60. Frequency-averaged results from 54 measurements in the SPF with the cryo-floor, and the average of all measurements, which gives the estimated response of the chamber.

6.1.2. Mid-band Results and Anomalies

Data between 1 GHz and 18 GHz were processed in a manner similar to that applied to the low-frequency data. Unfortunately, the high-frequency system (including cables, attenuators, connectors, and optical links) was much more sensitive to proper connection procedures. On a few occasions, after a measurement (or worse, after a series of measurements) was completed, we found that a connector was loose. As a result, there are a small number of anomalies that were most likely caused by loose connectors, but could possibly indicate positional dependencies in the SPF. A summary of our measured results is shown in Figure 61. The green curves, which have unusual results between 8 GHz and 12 GHz, were all taken on a single vertical scan of the SPF. A cross check before the vertical scan showed a good connection, but after the scan a second cross check showed a questionable connection, so most likely there was a loose connector during the entire vertical scan. The blue curve indicates a single anomalous result

between 1.4 GHz and 1.6 GHz. Measurements before and after the questionable measurement appear to be fine. As a result, we have no explanation for the observed behavior, but we think it is not a characteristic of the SPF. Finally, between 16 GHz and 18 GHz, there is a small rise and fall in all of the insertion-loss measurements. This appears to be related to characteristics of the mismatch correction factor that was applied to the measured data, and is not typical or explainable based on what we know of large conductive cavities. Therefore we assume that this artifact is a characteristic of our measurement system and not the SPF. As a result, we estimate the behavior of the SPF as a straight line in this region, with endpoints determined by data at higher and lower frequencies.

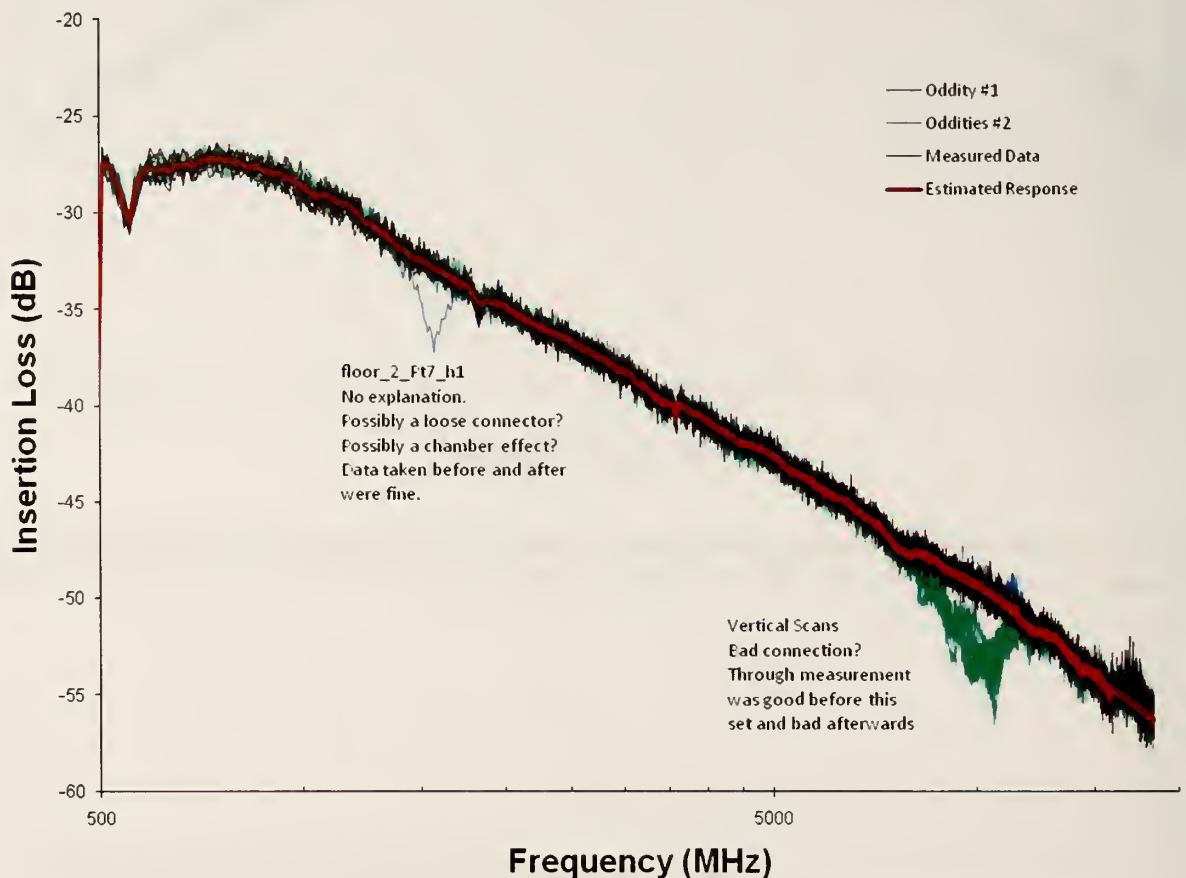


Figure 61. Frequency-averaged results from 29 measurements in the empty SPF, including anomalies, and the average of all “good” measurements.

Figure 62 shows measured results with the cryofloor in the SPF. Out of 54 measurements, only one showed anomalous behavior (curve shown in green), and this one measurement was the last measurement, taken on a Saturday afternoon. This unusual behavior shows a higher response (less loss) and is not consistent with a connector problem, which typically results in higher apparent loss. However, given when the anomalous measurement was taken, we assume that the unusual results are due to human error and are not representative of the SPF.

Again, consistency in the curves shown in both Figure 61 and Figure 62 (ignoring the anomalies) is much better than expected, with a standard deviation of approximately 0.4 dB to 0.45 dB.

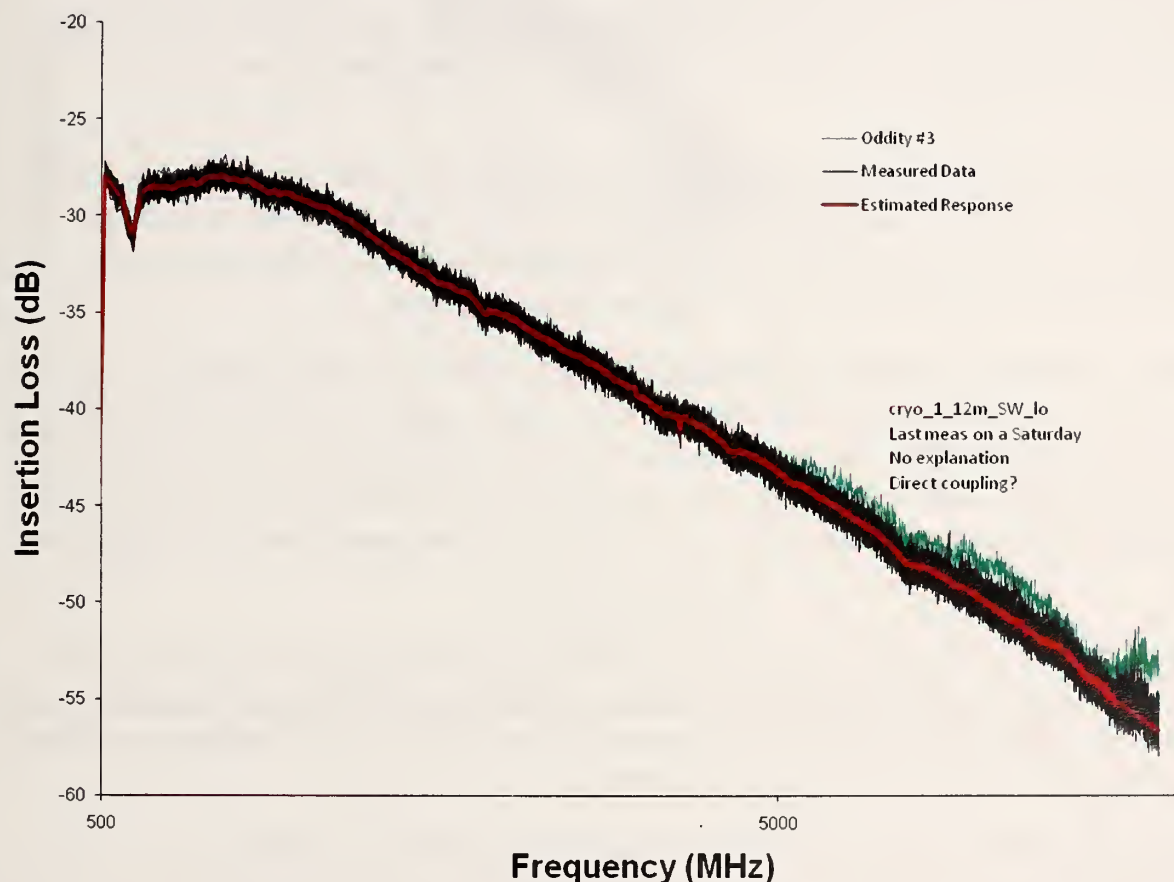


Figure 62. Frequency-averaged results from 54 measurements in the SPF with the cryo-floor, including anomaly, and the average of all “good” measurements.

Due to the somewhat unorthodox methods used in processing these data, we recommend that additional measurements be performed to definitively rule out or verify the anomalous behavior.

6.1.3. High Frequency Results and Anomalies

Above 18 GHz, measurements were both more complicated and significantly more limited. Only 12 locations were evaluated in the empty SPF, shown in Figure 63, and 5 locations with the cryo-floor located in the SPF, shown in Figure 64. These figures are plotted on a logarithmic frequency scale to be consistent with previous figures. Unfortunately, since these frequencies

span slightly more than one octave, the logarithmic spacing results in large “blank areas.” These blank areas become less significant when the full spectrum of measured frequencies is presented. In every measurement shown in both Figure 63 and Figure 64, there is an unexpected dropout between 32 GHz and 35 GHz. Subsequent analysis revealed the same behavior when the antennas are directed at each other, in both the SPF and an anechoic chamber. Reflection characteristics do not indicate poor matching characteristics at these frequencies. The evidence indicates that the antennas used in these measurements must have lossy characteristics at these frequencies, and the observed dropouts are indicative of antenna imperfections and not imperfections in the SPF.

Once the cryo-floor was placed in the SPF, one of the five measurements made, shown in green in Figure 64, is obviously and significantly different (3 dB or more) from any of the other measurements. We assume this was the result of a mechanical problem (cable, connector, instrumentation) and therefore disregard this measurement entirely.

In addition, there are anomalies between 18 GHz and 20 GHz. These were much more evident on the later measurements made when the cryo-floor was in place. Given the relatively good behavior from 1 GHz to 18 GHz, we think that the observed anomalies are due once again to cable and connector issues. However, since we have done no additional measurements in the SPF, it remains possible that the variations are indicative of some spatial non-uniformity in the SPF.

In both Figure 63 and Figure 64, the red curve indicates our best estimate of the insertion loss characteristics of the SPF based on measurements, experience, and in some cases educated guesses (removing trends that seemed unexpected or inconsistent). Further measurements should be performed to validate or refute these assumptions.

The agreement between the 12 curves in Figure 63, ignoring obvious anomalies, is not as good as that observed at lower frequencies, but the standard deviation is still less than 0.6 dB. For the 4 black curves in Figure 64, agreement is somewhat worse. Ignoring the data below 20 GHz, the standard deviation is typically around 0.5 dB, but approaches 1 dB near 25 GHz and above 38 GHz.

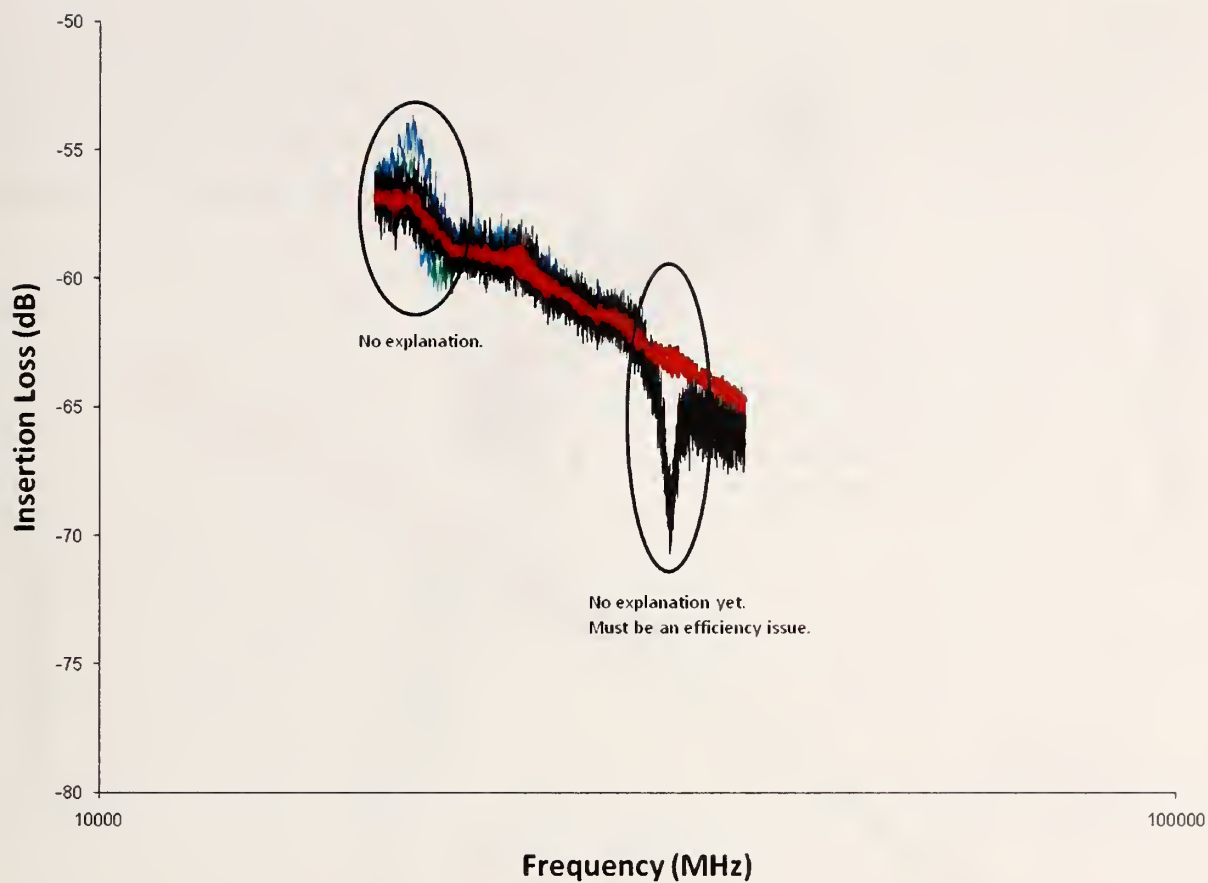


Figure 63. Frequency-averaged results from 12 measurements in the empty SPF, including anomalies, and an estimated SPF behavior.

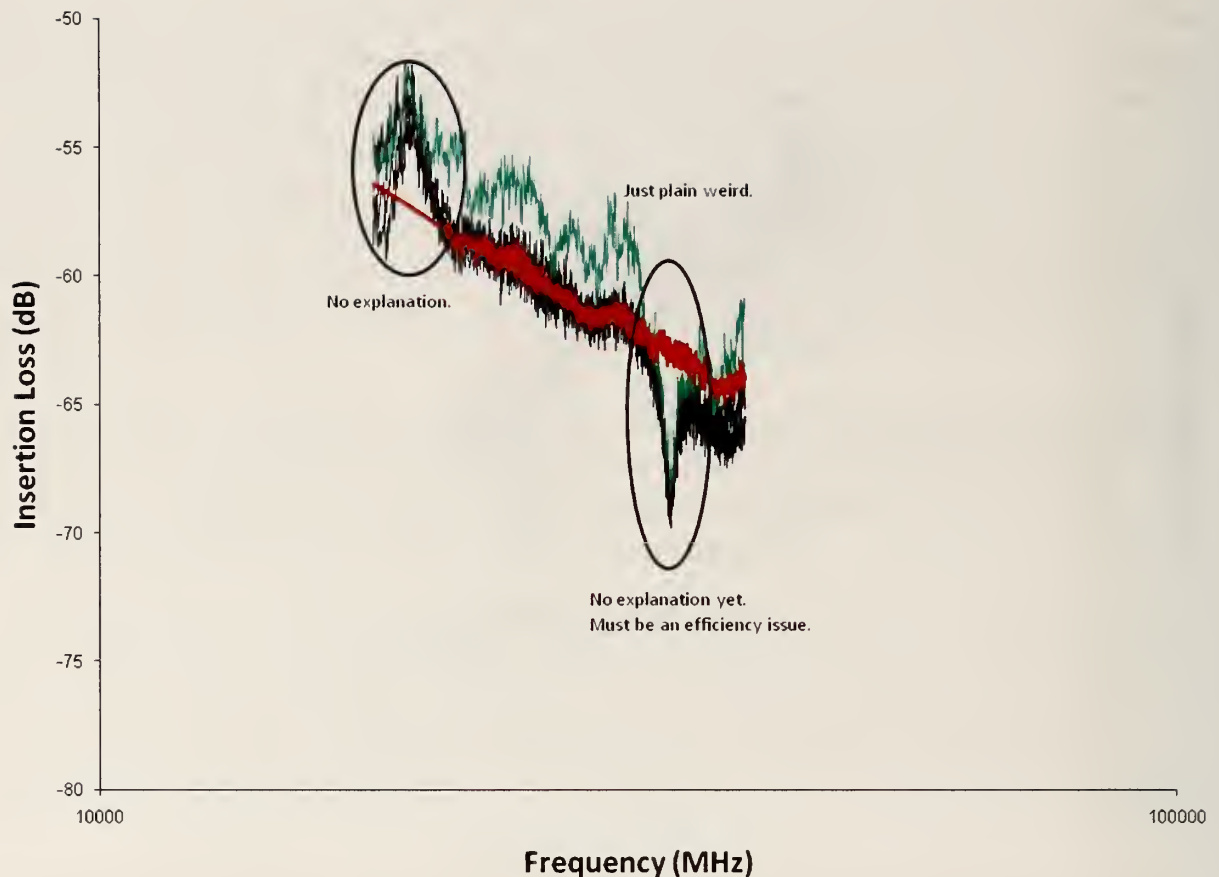


Figure 64. Frequency-averaged results from five measurements in the SPF with the cryo-floor, including anomalies, and an estimated SPF behavior.

6.1.4. Overall Summary

Over the entire frequency range, the overall uniformity from location to location was significantly better than expected, with variations on the order of what we would expect from an ideal chamber. **The multiple anomalies are troubling, and we strongly recommend additional measurements to either confirm or refute our assumption that any measured results that are significantly different from others are in fact anomalies and not due to the SPF.**

We combined results from each frequency band to obtain an overall estimate of the insertion loss of the SPF from 70 MHz to 40 GHz, as shown in Figure 65. This figure shows disagreement between the low-band and mid-band measurements that can be traced to using the measurement antennas out of their recommended frequency ranges. Figure 65 also shows original data (broad light curves) and our estimated corrected or “cleansed” data (narrower and darker curves). We then selected the data from each band that we considered to be most reliable to generate a single

estimate of the insertion loss over the entire frequency range. The result for both the empty SPF and the SPF with the cryo-floor in place is shown in Figure 66. The uncertainty is the estimated chamber response is discussed in section 7, and our standard uncertainties are evaluated to be less than 2 dB. This estimated uncertainty should apply to all of the subsequent quantities derived from estimates of the insertion loss.

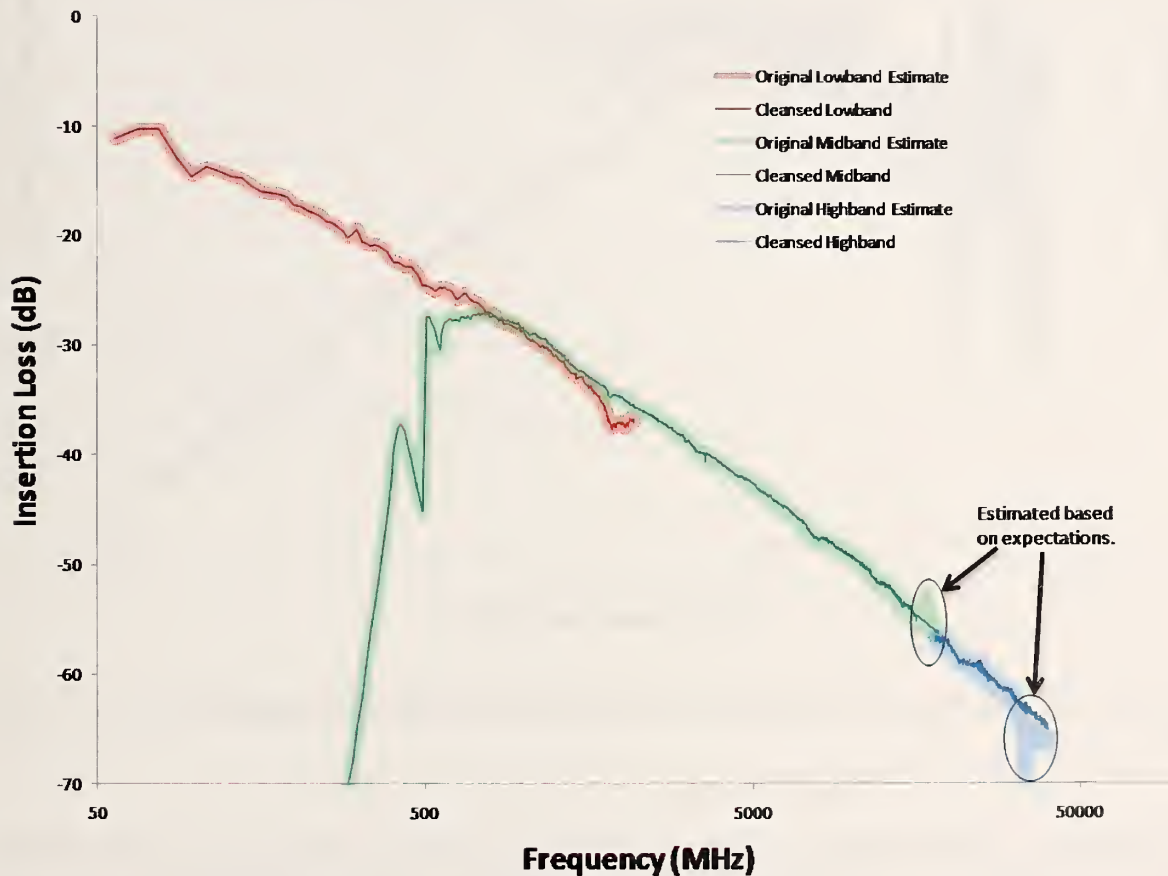


Figure 65. Combined estimated chamber insertion loss.

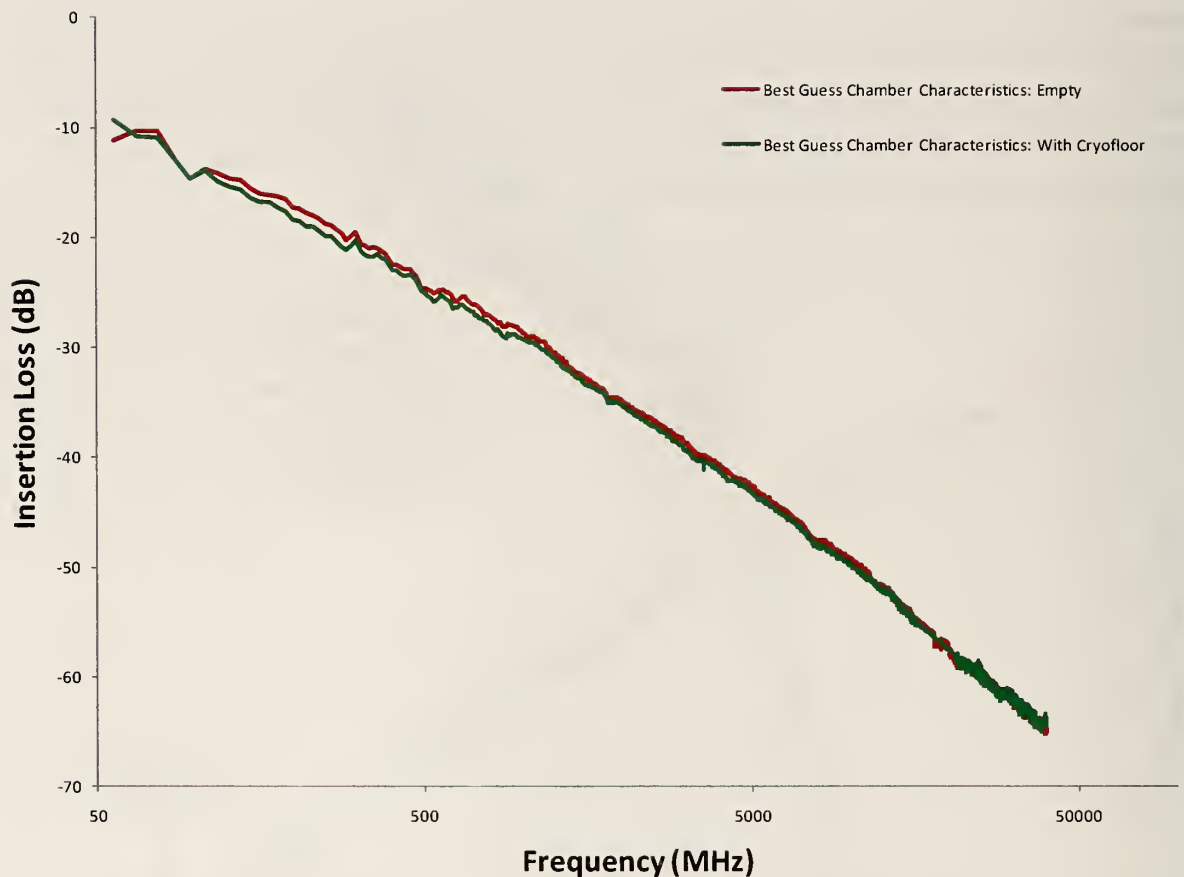


Figure 66. Final estimated insertion loss for the SPF, both with and without the cryo-floor.

The difference in insertion loss estimates of the SPF with and without the cryo-floor (Figure 67) is surprisingly small (generally less than 1 dB, and always less than 1.25 dB). It is a large structure covered in a black, high-carbon paint, so we were expecting substantially more loss. However, the cryo-floor is small relative to the overall size of the SPF, and evidently results in only a small perturbation.

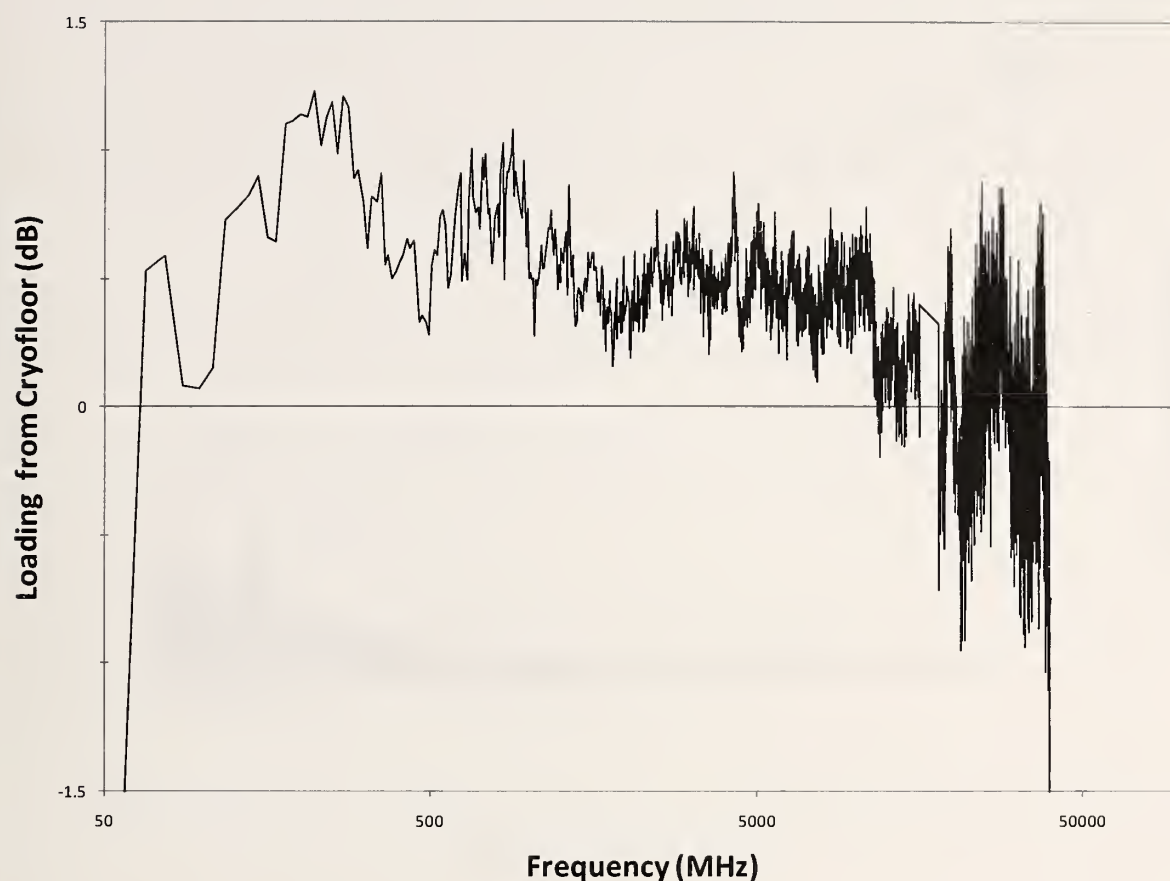


Figure 67. Estimated loading due to placement of the cryo-floor in the SPF.

Finally, we plot the variability of all of the frequency-averaged measurements we made with the VNA system in Figure 68. This is the standard deviation of all measurements performed at different locations in the chamber (after removing anomalous results). The most impressive characteristic of this chart is that the standard deviation is very close to the theoretical limit for an average of 141 samples for most of the measured frequency range. The data above 18 GHz are noticeably higher and noisier than those at lower frequencies. The higher level is most likely due to higher uncertainties associated with the high-frequency measurement system. The data appear to be noisier because far fewer measurements were made using the high-frequency system. More measurements would have reduced the noise, but the mean trend of higher variability would have remained the same.

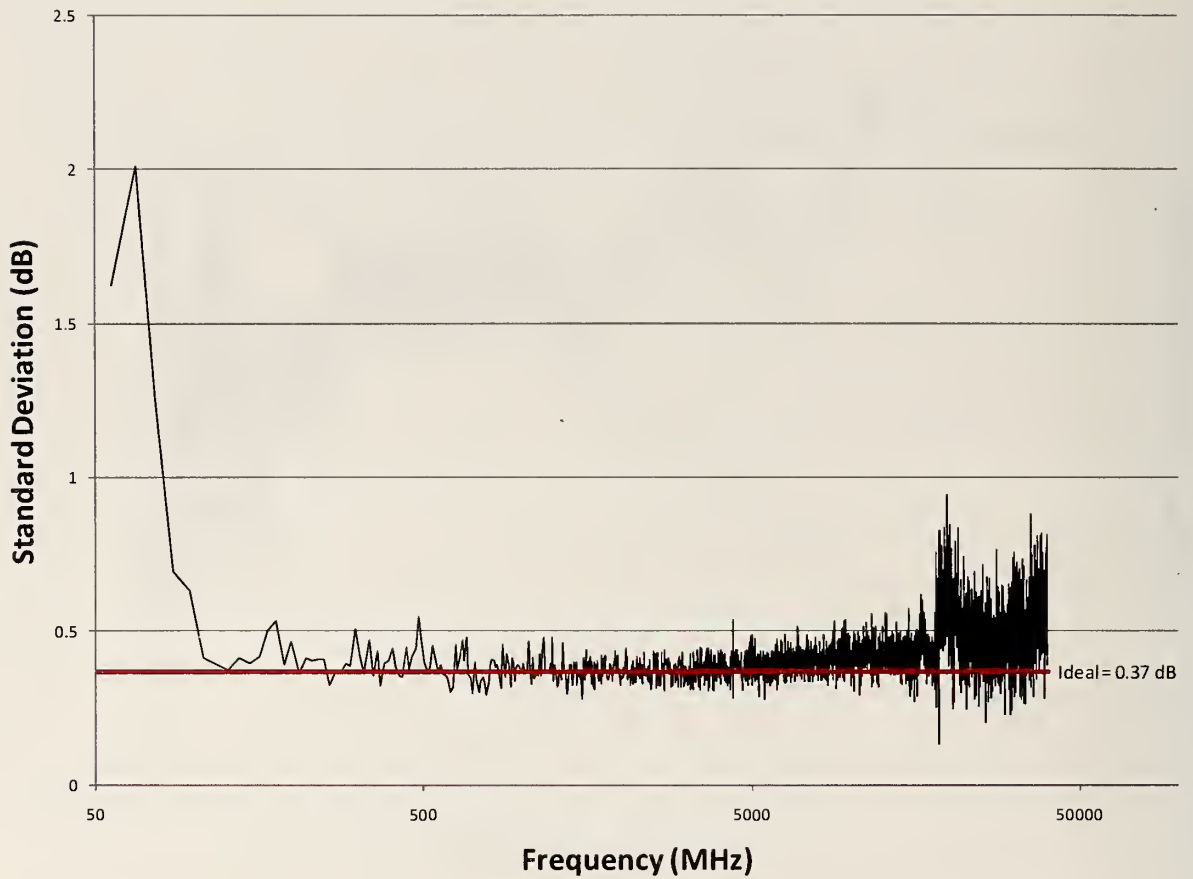


Figure 68. Spatial uniformity of frequency-averaged insertion loss measurements.

6.1.5. Derived Quantities

Once we have an estimate of the insertion loss of the chamber, we can estimate many other parameters [14]. All parameters estimated here are based on measurements made with the cryo-floor present in the SPF. For example, the quality factor Q can be estimated from the loss L as

$Q = \frac{16\pi^2 V}{\lambda^3} L$, where V is the volume of the SPF and λ is the wavelength. Our estimated Q is shown in Figure 69.

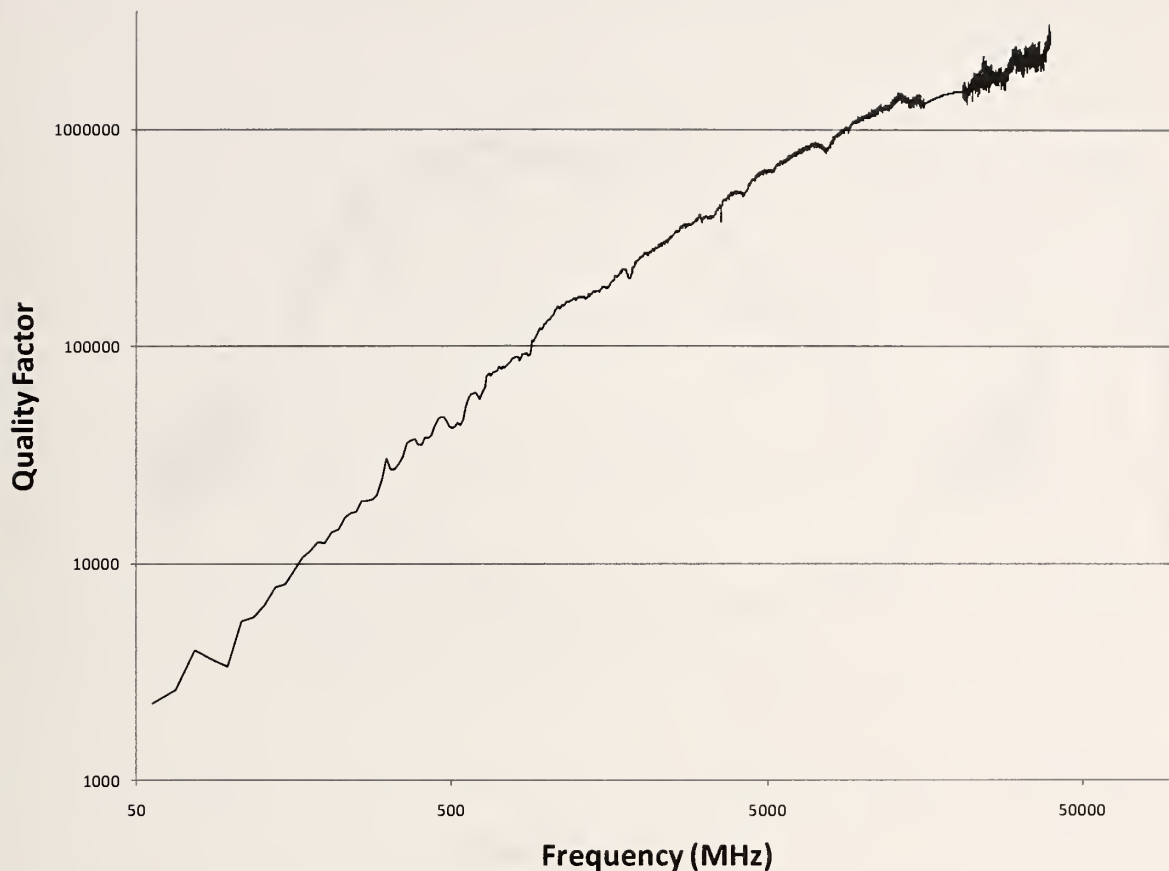


Figure 69. Estimated quality factor of the SPF.

From Q , many other quantities can be estimated. The exponential decay time τ , sometimes referred to as the “ring time,” can be estimated from Q as $\tau = \frac{Q}{\omega}$, where ω is the radian frequency. The estimated decay time is shown in Figure 70. Ring times in excess of 10 μs are typical for frequencies over 200 MHz, with ring times of 20 μs from 1 GHz to 7 GHz. This will make pulsed rf testing complicated, especially for short pulses with durations on the order of the ring time or less, and will require further investigation.

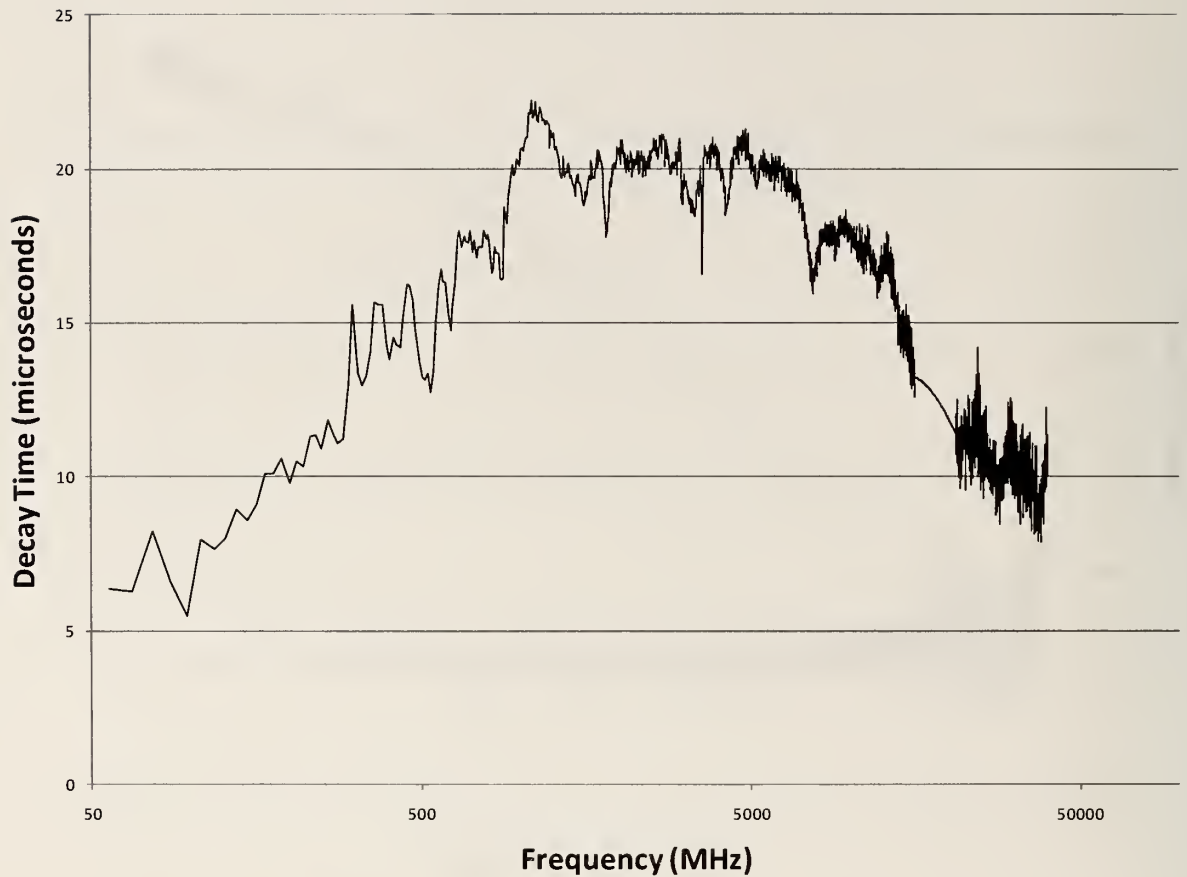


Figure 70. Estimated decay time of the SPF.

We can also estimate the “bandwidth” BW of individual modes in the SPF to verify that samples taken as a function of frequency were taken at an interval large enough for the samples to be roughly independent. The bandwidth can be estimated as $BW = \frac{f}{Q}$, where f is the frequency.

The estimated bandwidth is shown in Figure 71. In general, the mode bandwidth is narrower than 25 kHz, which is well below the frequency step size of 75 kHz used in the VNA measurements.

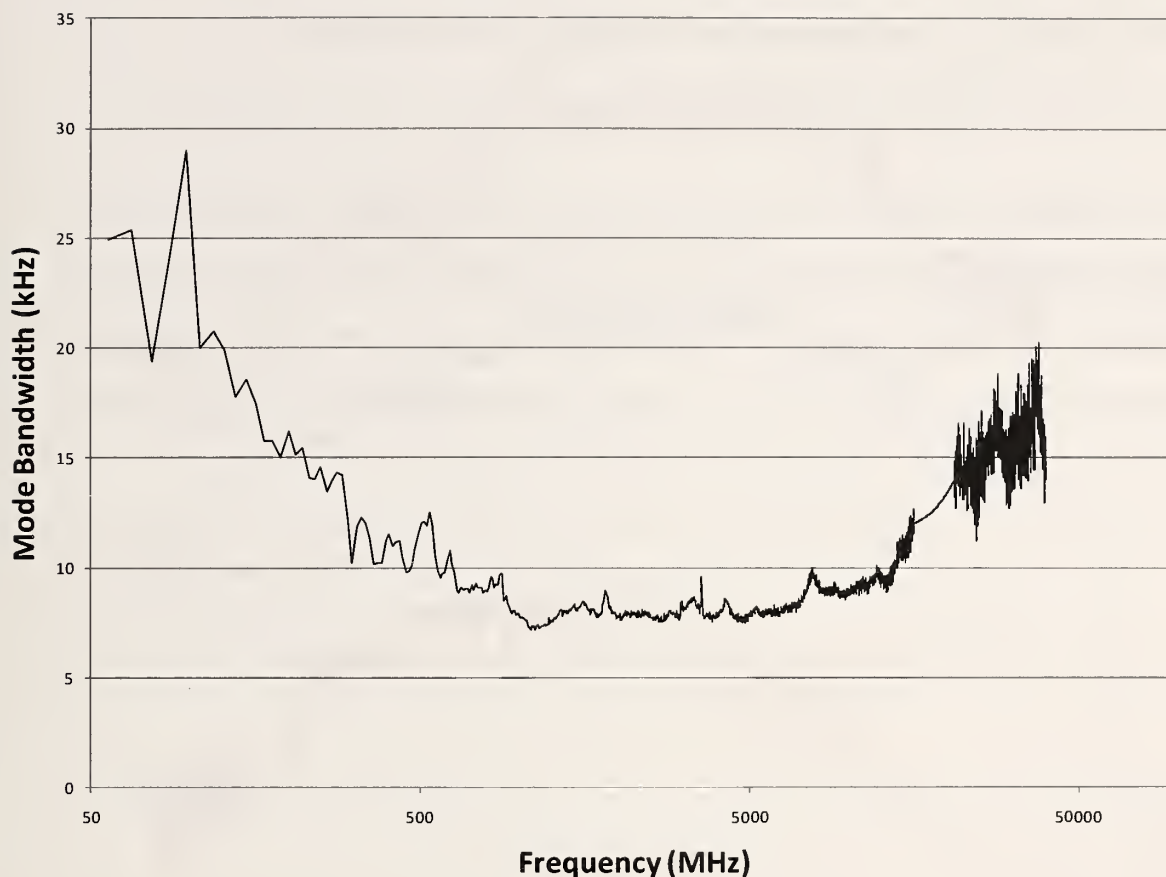


Figure 71. Estimated mode bandwidth.

6.1.6. Electric Fields

We can also use the estimates of the SPF insertion loss to predict either the fields that can be generated for a given input power or, alternatively, the power required to generate a particular field level. As mentioned in section 4.1, there can be some ambiguity here depending on whether we are referring to the total electric field or a Cartesian component of the electric field, the average field, or the expected peak field (and the expected peak field depends on the number of samples or paddle positions used during the test). For this section of the paper, we will give results for both expected peak total field and expected peak Cartesian field based on the typical minimum number of required paddle positions given in reverberation-chamber standards, or 12 samples. Note, however, that higher expected peak field levels are possible for the same input power if more samples are used or assumed.

To begin, we estimate the average fields generated assuming an incident power of 1 W and an insertion loss L . The mean Cartesian or rectangular field $\langle |E_R| \rangle$ can be estimated as

$\langle |E_R| \rangle = \frac{4\pi}{\lambda} \sqrt{5\pi L \cdot 1W}$, and the mean total field $\langle |E_T| \rangle$ can be estimated as

$\langle |E_T| \rangle = \frac{15}{8} \langle |E_R| \rangle = \frac{15\pi}{2\lambda} \sqrt{5\pi L \cdot 1W}$, [14], and our estimates are shown in Figure 72.

With 12 samples, the peak Cartesian field is a factor of approximately 1.9 higher than the average Cartesian field, and the total field is a factor of approximately 1.5 higher than the average total field; these estimated peak fields are shown in Figure 73. Given an estimate E of the peak field for an input power of 1 W, we can determine power P required to establish a desired peak field E_D as $P = \left(\frac{E_D}{E}\right)^2$, and we plot the estimated required power for a field of 30 V/m in Figure 74 and for a peak field of 200 V/m in Figure 75.

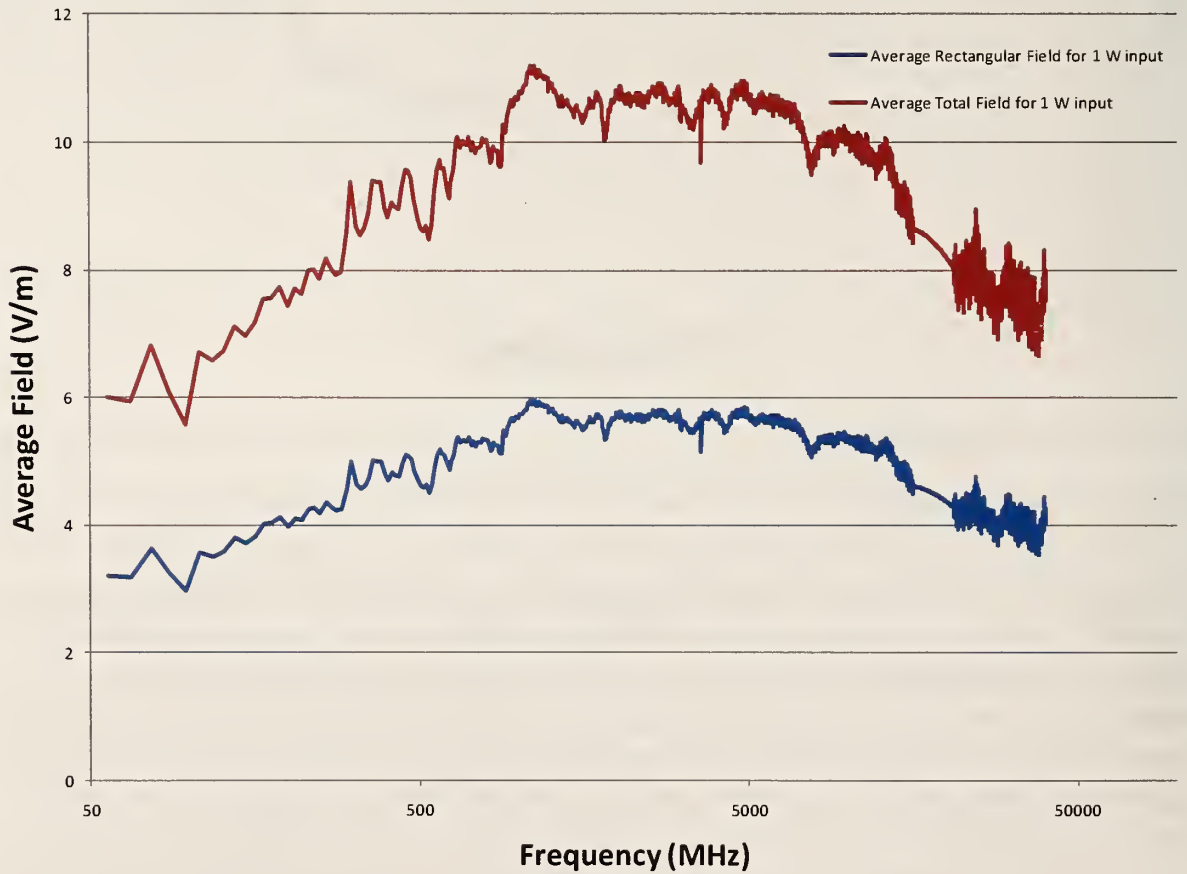


Figure 72. Estimated average field for 1 W input power.

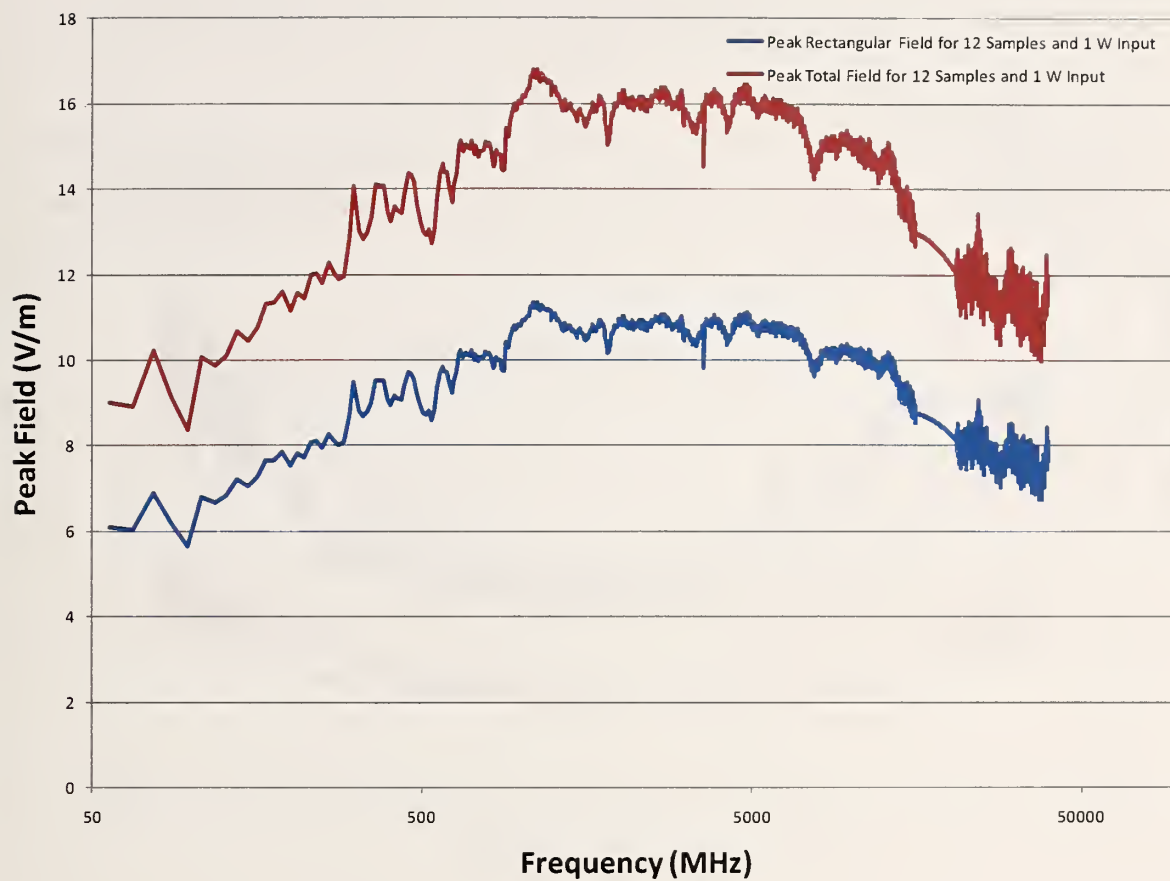


Figure 73. Estimated peak field for 12 samples and 1 W input power.

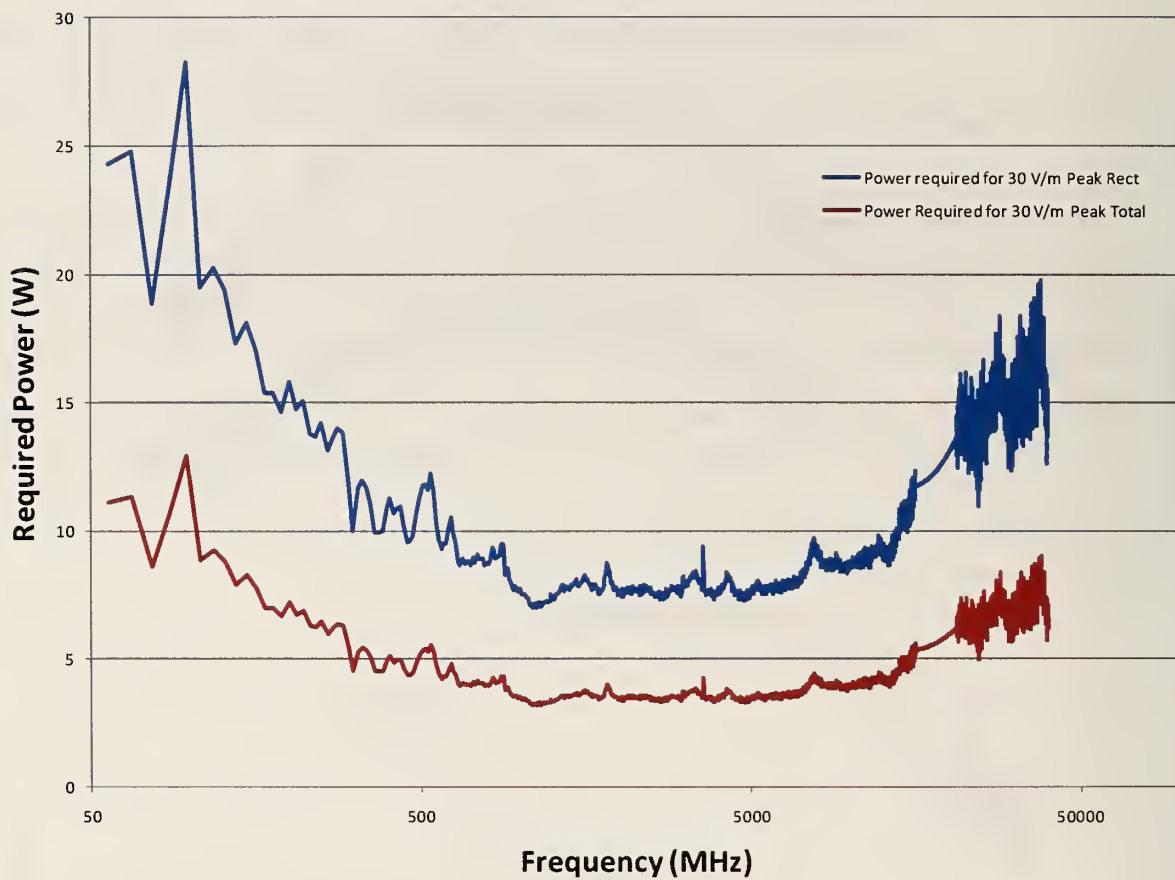


Figure 74. Estimated power required for 30 V/m field assuming 12 samples.

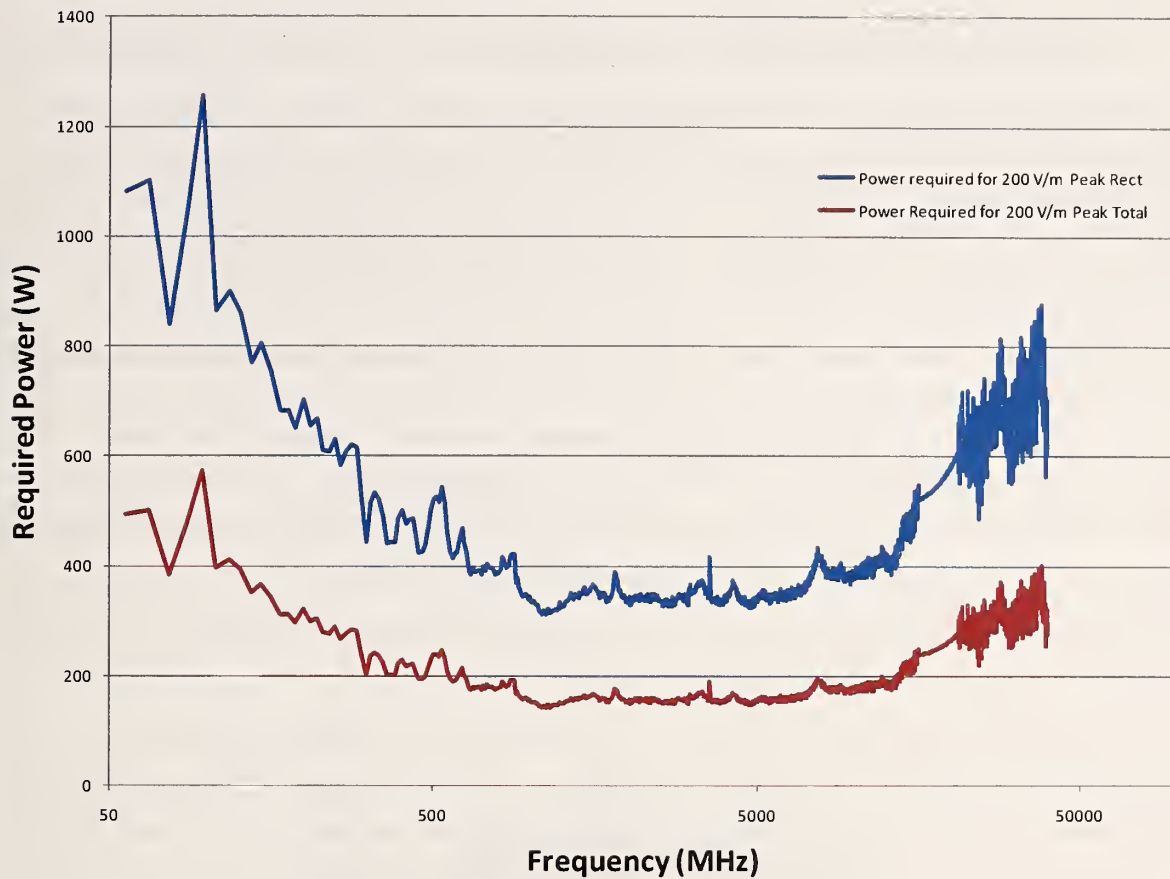


Figure 75. Estimated power required for 200 V/m field assuming 12 samples.

6.2. Basic Probe System Measurement Results

The probe system was used to evaluate the fields in and around the expected volume of possible spacecraft. The measurements were performed by placing ten probes on a circular structure, and then taking measurements with the structure placed at thirteen different elevations. The purpose of the measurements was to give an approximate evaluation of the field uniformity of the SPF, and to compare the results against those described in typical reverberation-chamber standards [4][6]. To balance out the competing goals of sampling over a large volume and reducing uncertainties by using a large number of paddle positions, we chose to perform all measurements at 12 paddle positions, which is the minimum allowed by the standards (if a chamber performs well enough, then all measurements will be performed using the minimum number of paddle positions). In general, approximate uncertainty bounds in decibels for a given number of samples

N can be estimated as $U_{dB} \approx 10 \log \left(1 \pm \frac{1}{\sqrt{N}} \right)$. For Small N , the upper and lower bounds of U_{dB}

will be asymmetric and difficult to discuss. For example, for $N = 12$, $U_{dB} \approx 10 \log \left(1 \pm \frac{1}{\sqrt{12}} \right)$ with an upper bound of 1.1 dB and a lower bound of 1.5 dB. Assuming a perfect chamber, perfect paddle, and only 12 samples, the best we can hope for is a standard deviation of approximately 1.3 dB (halfway between 1.1 dB and 1.5 dB), and we expect the results to be much worse than this given the paddle used to perturb the field. We are therefore unlikely to detect small non-uniformities. Note, however, that standards allow a standard deviation of 3 dB or greater.

During the tests, we encountered two significant problems. First, the X axis of one of our probes (probe 1) did not function, and therefore readings from probe 1X are not included in any analysis. Second, the amplifier used for measurements between 1 GHz and 2 GHz failed halfway through the evaluation. Therefore, we have measurements at only seven elevations between 1 GHz and 2 GHz, and the measurements that were taken in this range are questionable.

To illustrate the processing used to evaluate the probe data, we will examine measurements made at an elevation of 3 m in great detail, and then summarize the results obtained at each of the other elevations.

For a given elevation, and for each probe axis (of which we had 29 valid axes), we have measurements at 12 different paddle positions, and the fields can be quite different at each of those paddle positions (a factor of 10 or more). Rather than plot measured field at each paddle position for each probe axis (108 points per frequency per elevation can get a little confusing), we instead examine the average and maximum field measured on each probe axis. This still results in 29 average points and 29 maximum points per frequency, which results in charts that are less cluttered than charts showing 108 points per frequency.

Reverberation chamber standards [4][6] are focused primarily on the peak or maximum field measured of all paddle positions. These peak results tend to have higher associated uncertainties than average results, so we will instead begin our analysis with the average measured field.

Figure 76 shows the 29 measurements of average field, each normalized to a constant incident power of 1 W. The chart also shows the average (red) and standard deviation of the 29 measurements. Since the Cartesian field ideally has a Rayleigh distribution [14], the unaveraged field should have a standard deviation that is approximately half of the mean field, and averaging over 12 paddle positions should reduce this by a factor of $\sqrt{12} \approx 3.46$, for a standard deviation that is about 14 % of the average field. The observed standard deviation in the range of 30 % to 50 % is obviously much larger than we would expect from an ideal chamber, which is disappointing, given the nearly ideal results we observed using the VNA measurement system. This indicates that the small paddle we used for the evaluation was inadequate for the SPF, as expected, and does not give ideal results.

The results can be further simplified by separating them by probe axis, that is, group the nine X-axis measurements together, the ten Y-axis measurements together, and the ten Z-axis measurements together. Rather than show these individual curves, we will show the average (essentially an average over location of results that are already averaged over paddle position) and standard deviation (essentially the standard deviation over location of results that are already averaged over paddle position) of each group, as shown in Figure 77. The results are generally clustered together, but the Y-axis averages appear to have readings that are significantly higher than the rest at 250 MHz, 1.18 GHz, 1.55 GHz, and 2.4 GHz. Also, the standard deviation has a few apparently large values, especially for the X-axis data near 650 MHz and 3.4 GHz, the Y-axis data near 3 GHz, and the Z-axis data near 5 GHz.

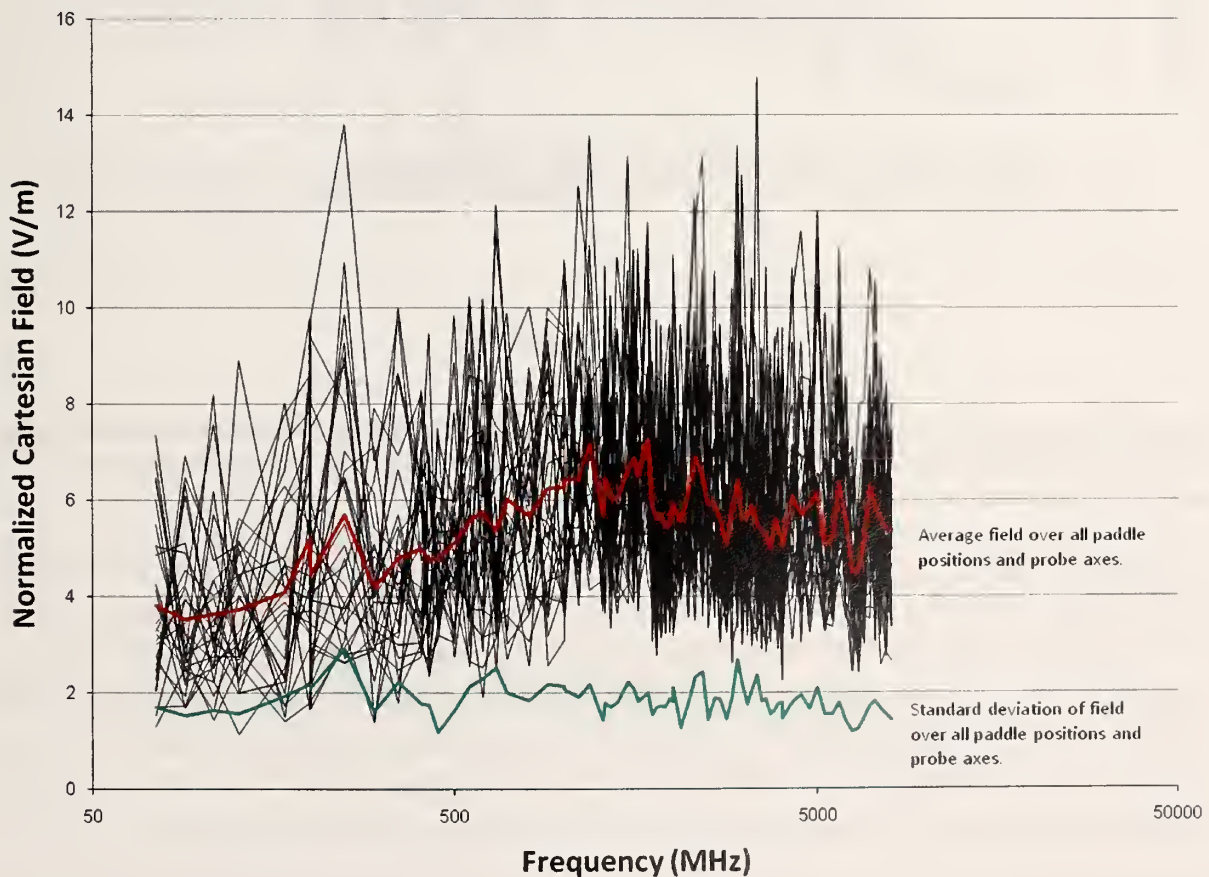


Figure 76. Average measured Cartesian field on 29 field probes for an elevation of 3 m. The red curve is the average of all 29 black curves, and the green curve is the standard deviation of all 29 black curves.

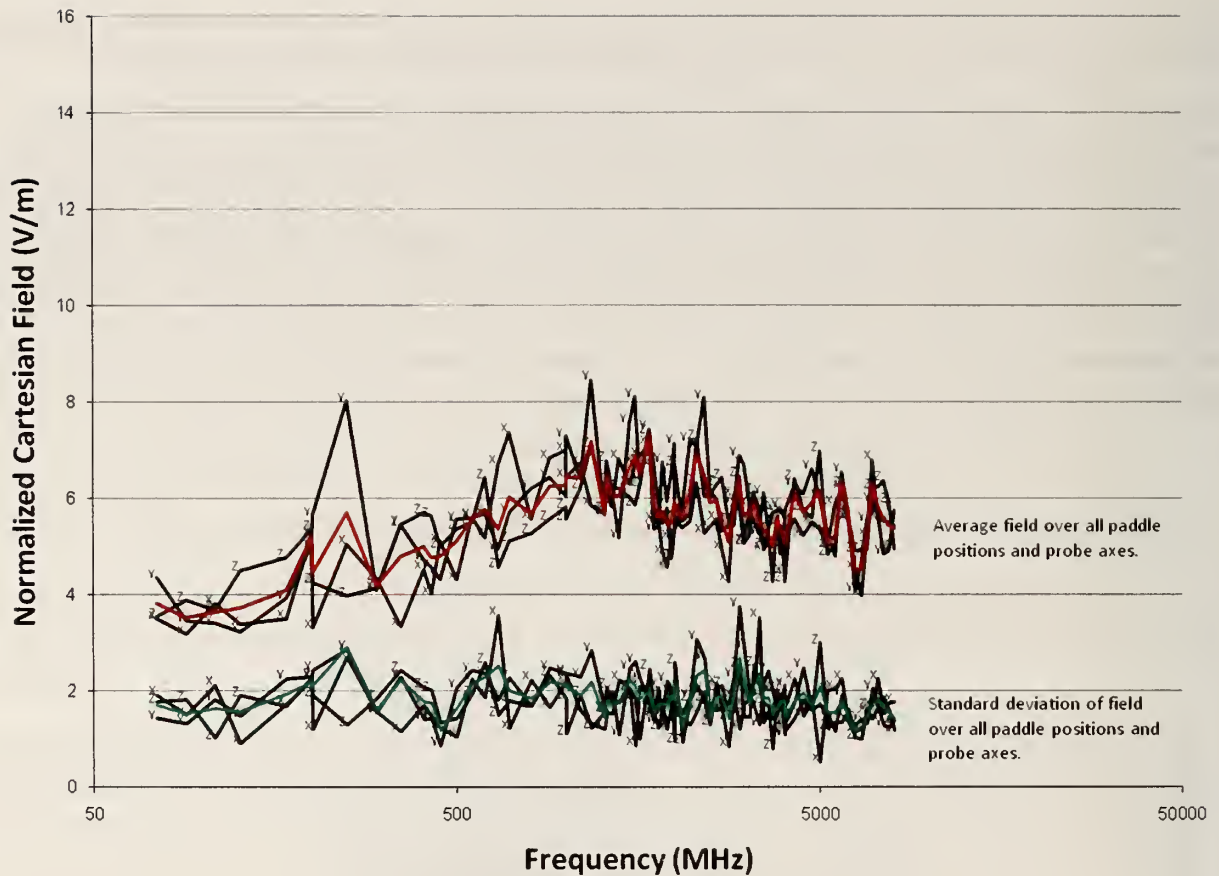


Figure 77. Average X, Y, and Z field components (upper black curves), along with the overall average (red), for an elevation of 3 m. The standard deviation of the components (lower black curves) and the overall standard deviation (green) is also shown.

Although these results do not compare favorably with those for an ideal chamber, it is interesting to compare them with limits given in the standards. To do this, we roughly follow the evaluation procedures given in the standards. We take all of our data at each frequency and create four subgroups: the X-axis data, the Y-axis data, the Z-axis data, and all of the data combined without regard to the axis. The means of these sets are denoted as μ_X , μ_Y , μ_Z , and μ_{All} , respectively. Similarly, standard deviations are denoted as σ_X , σ_Y , σ_Z , and σ_{All} , which are then used to compute a “dB standard deviation” as $\sigma_{dB} = 20 \log \left(1 + \frac{\mu}{\sigma} \right)$, where μ and σ are any matched pair of means

and standard deviations. These results are then compared to a limit specified by the standard. In general, the dB standard deviation must be below 3 dB for all frequencies above 400 MHz, below 4 dB or 6 dB (depending on the standard) from the lowest operating frequency to 100 MHz, and transitioning linearly (whatever that means on a dB scale) between 100 MHz and 400 MHz. Results for average measured field for an elevation of 3 m are shown in Figure 78.

Results are above the limit at several frequencies. This typically indicates that performance will be much worse for measures of the maximum field, which we will examine next.

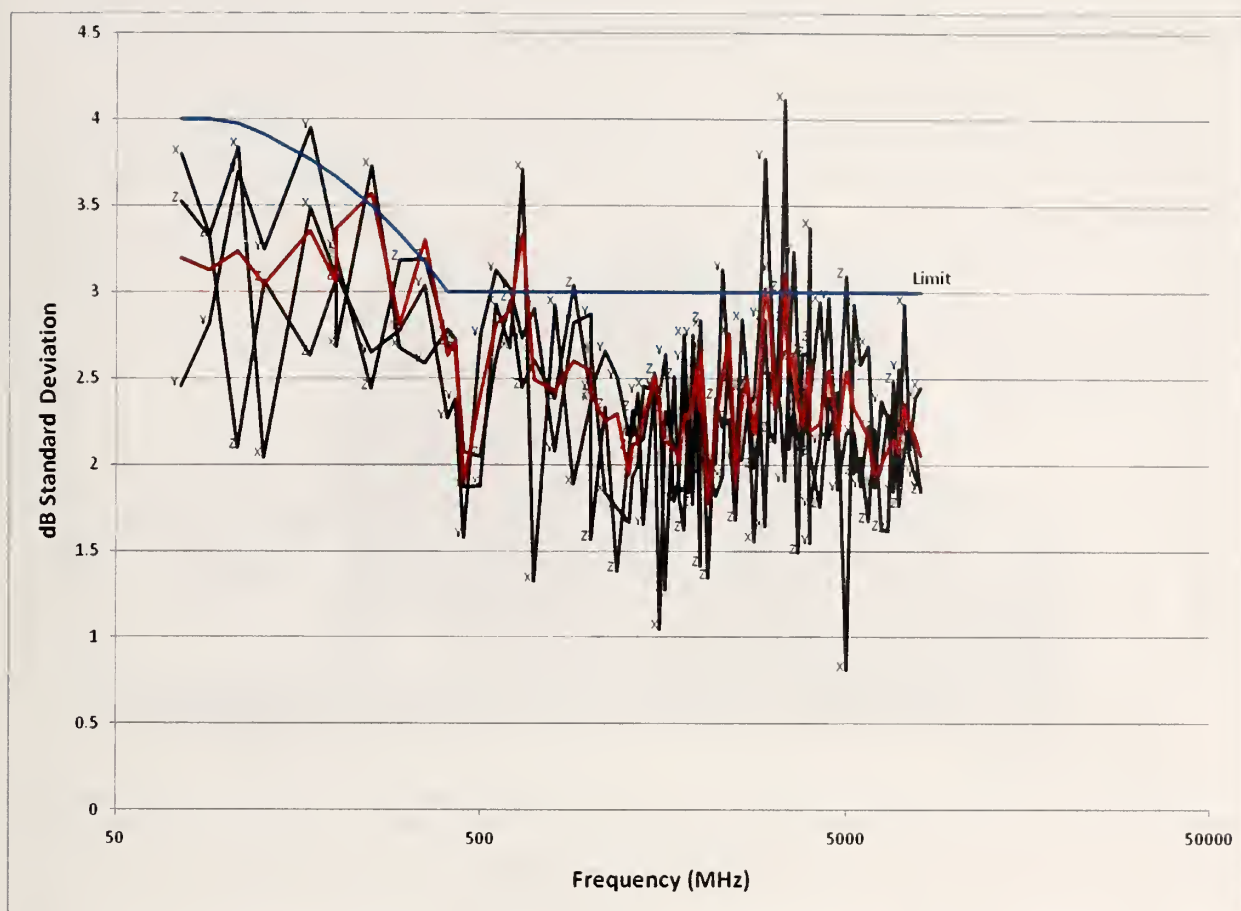


Figure 78. Standard deviation (dB) of the X, Y, and Z components, both combined (red) and separate (black) for an elevation of 3 m.

Figure 79 shows the 29 measurements of average field, each normalized to a constant incident power of 1 W. The chart also shows the average (red) and standard deviation of the 29 measurements. The standard deviation for the maxima is similar to that for the averages at around 25 % to 40 % of the peak field. For an ideal chamber we would expect variations of approximately 20 %. Refining the results somewhat, we next compute the average and standard deviation of the group of peak X components, Y components, and Z components, and all of the components combined, and the results are shown in Figure 80. Computing the dB standard deviation as was done for the average field gives us the results shown in Figure 81. Remarkably, only one point on this chart exceeds the limit: the standard deviation of the X component measured at 3.4 GHz. Since only one point exceeded the limits, and that point exceeded the limit by only a few tenths of a dB, this chamber would have passed the calibration requirements of a reverberation chamber based on both DO-160 and IEC 61000-4-21, despite our extremely small paddle and the apparently poor performance of the average field. Since the peak field in an ideal chamber always has higher uncertainty than a corresponding average field, we expected this relationship to be present for a non-ideal chamber such as this one with a small paddle. Again, we have no explanation for this result.

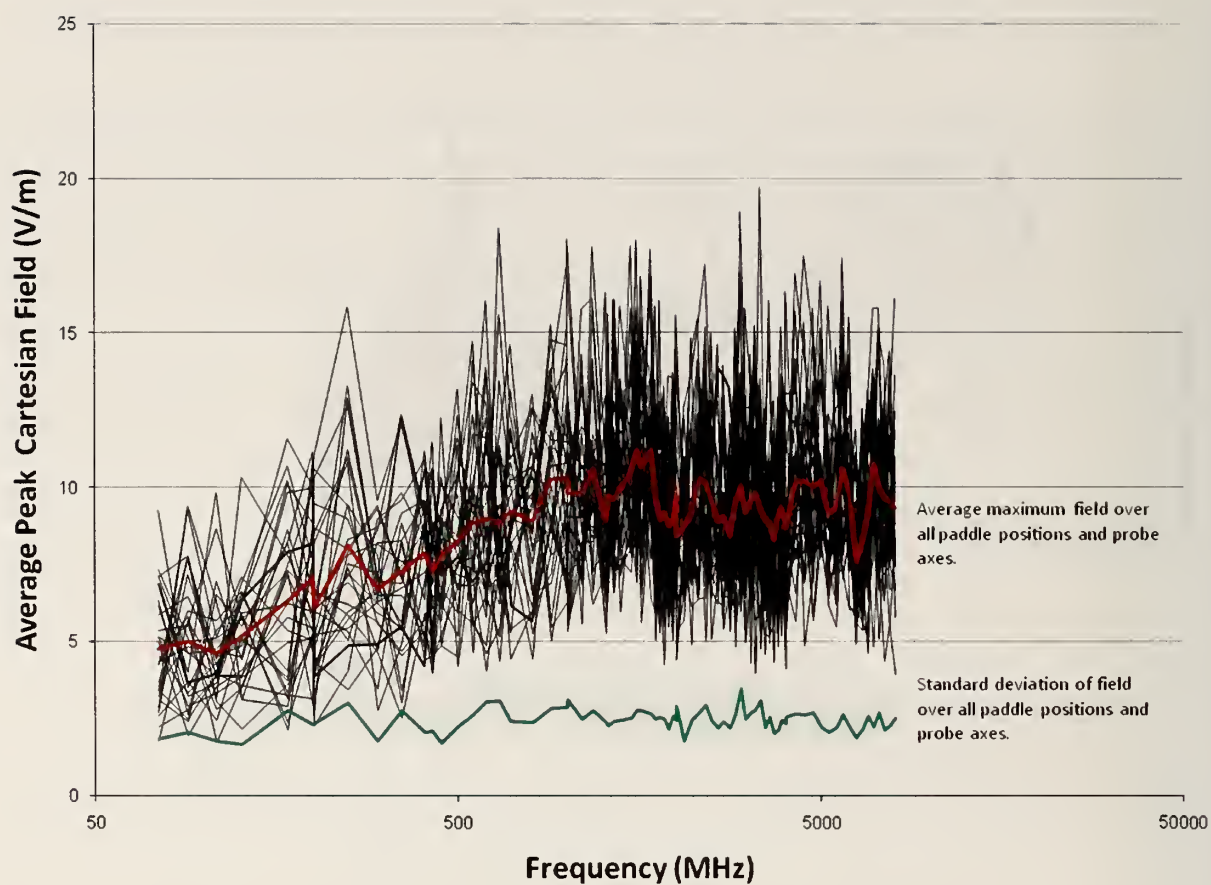


Figure 79. Average peak measured Cartesian field on 29 field probes for an elevation of 3 m. The red curve is the average of all 29 black curves, and the green curve is the standard deviation of all 29 black curves.

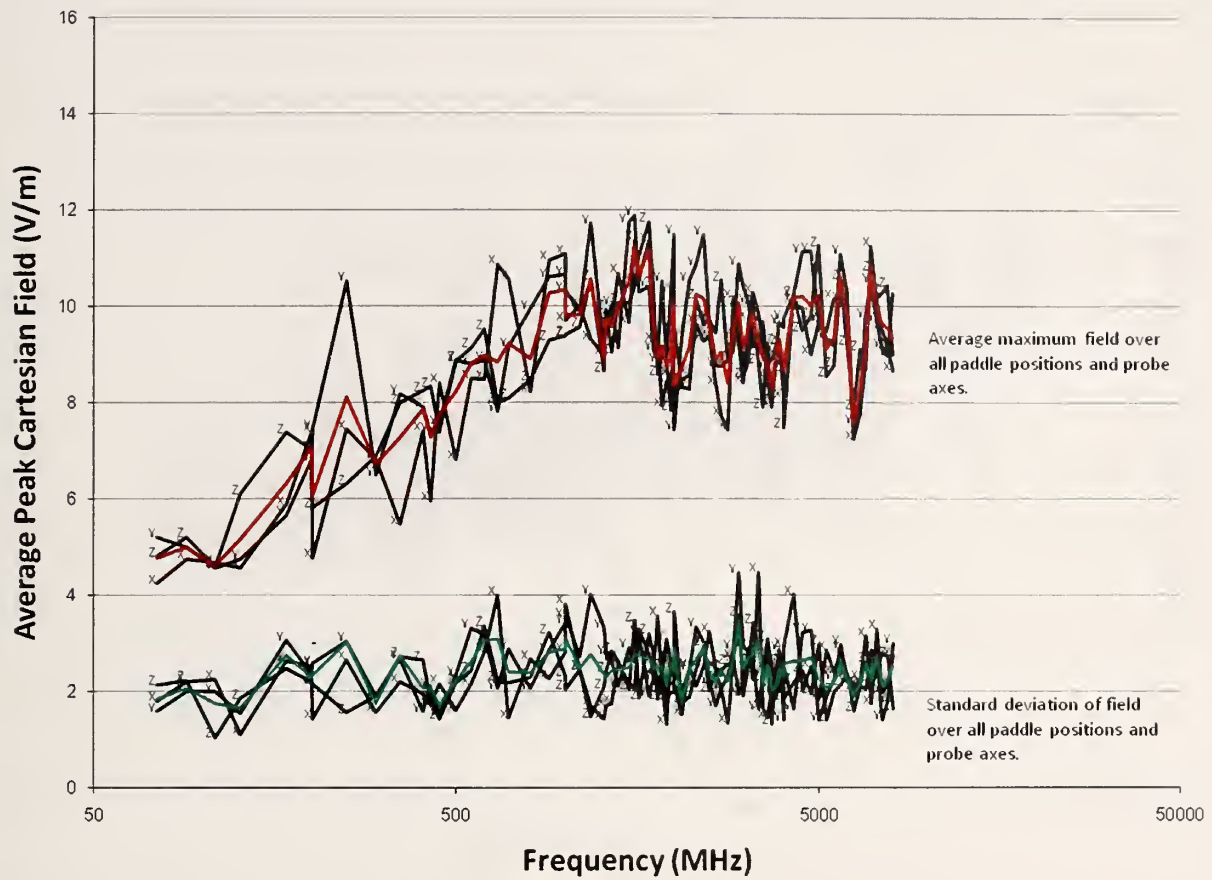


Figure 80. Average peak X, Y, and Z field components (upper black curves), along with the overall average (red), for an elevation of 3 m. The standard deviations of the components (lower black curves) and the overall standard deviation (green) are also shown.

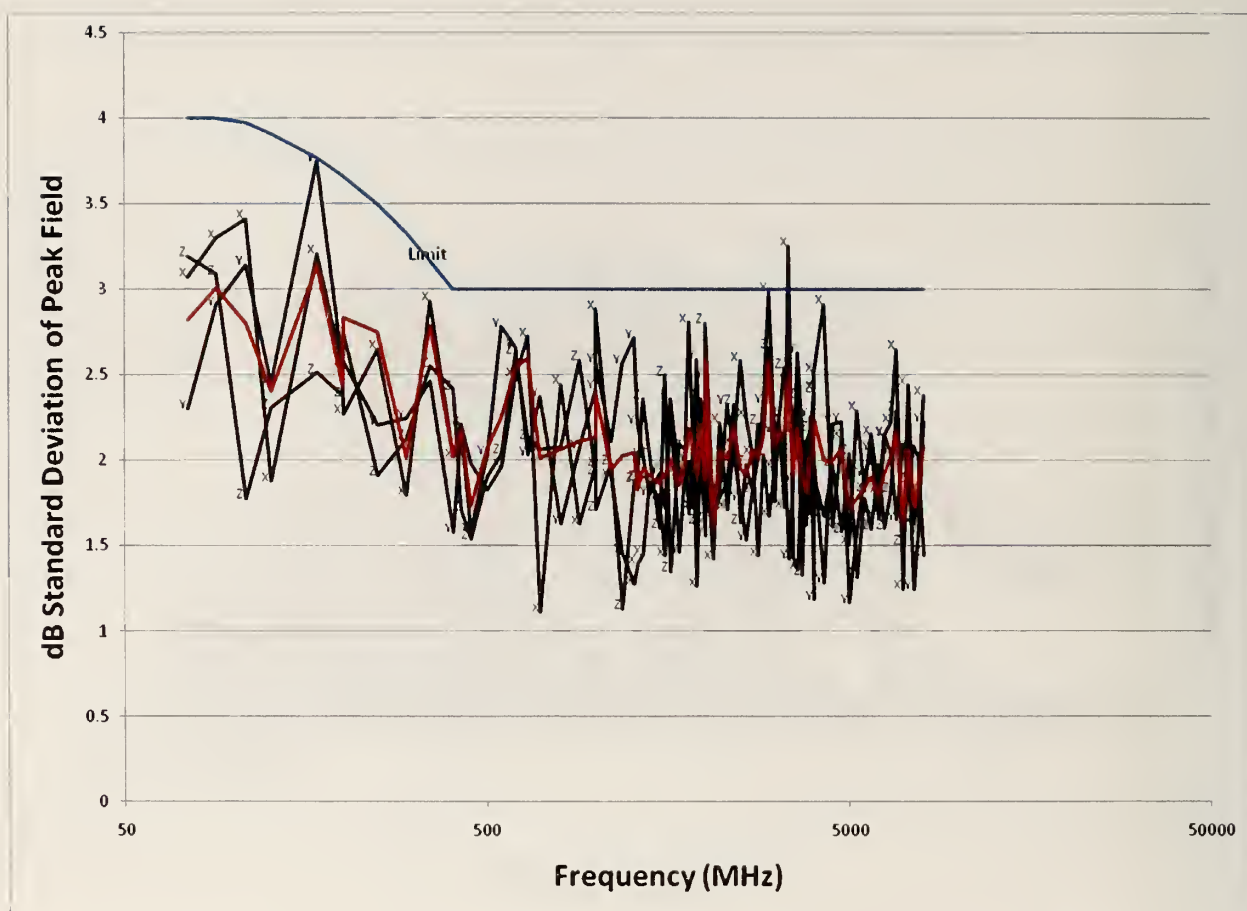


Figure 81. Standard deviation (dB) of the peak X, Y, and Z components, both combined (red) and separate (black) for an elevation of 3 m.

In addition to the Cartesian components of the field, we also evaluated the total electric field for each of the nine valid probes (excluding probe 1, which had a faulty X channel). These results are summarized in the charts below. Figure 82 shows the normalized average total field measured in the SPF, as well as the overall average, and the standard deviation over the nine locations. The dB standard deviation of the average total field is shown in Figure 83. For an ideal chamber, we would expect a dB standard deviation of approximately 0.4 dB. Figure 84 shows the normalized average total field measured in the SPF, as well as the overall average, and the standard deviation over the nine locations. Figure 85 shows the dB standard deviation of the peak total field, which can be compared to a dB standard deviation of approximately 0.5 dB. Again, the dB standard deviation of the peak total field is less than the dB standard deviation of the average field.

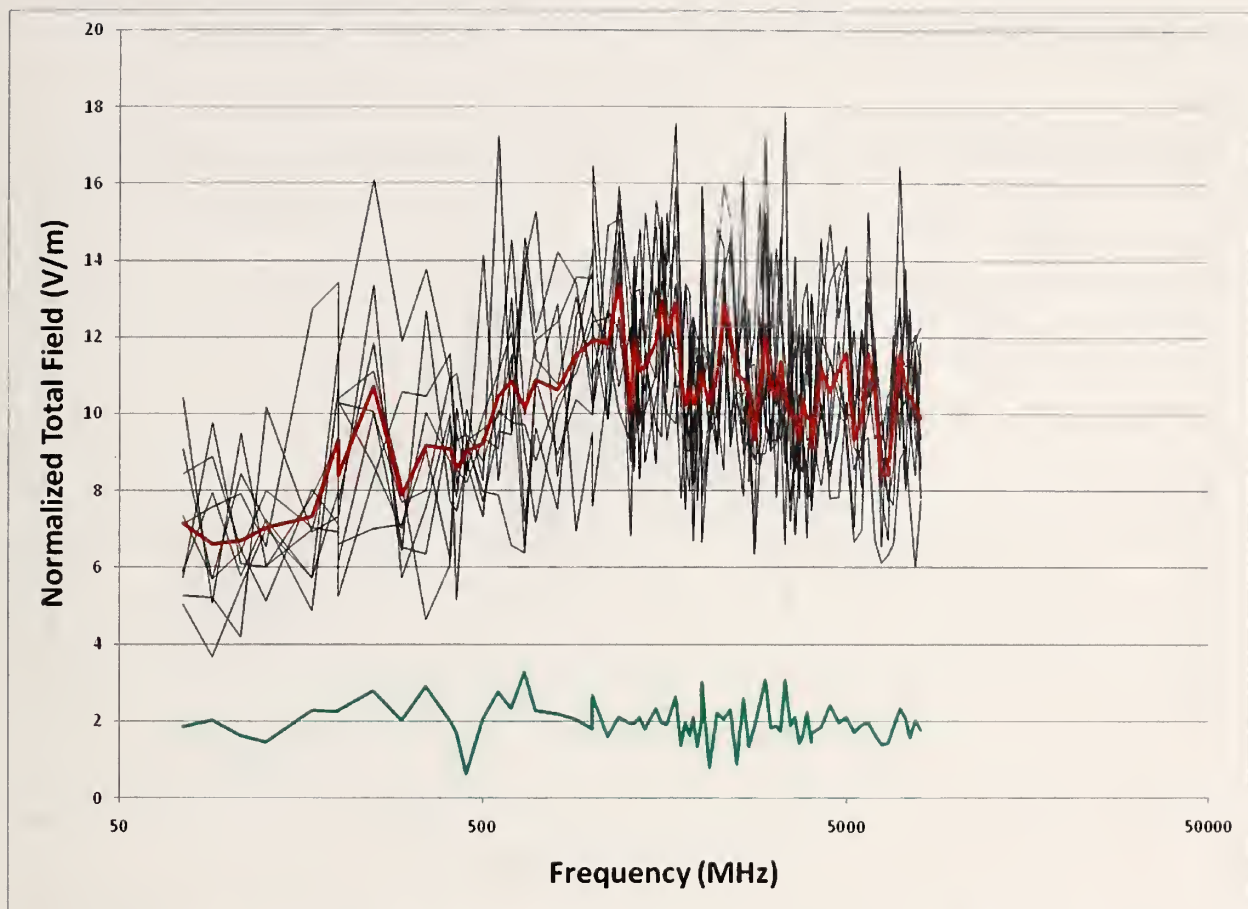


Figure 82. Average measured total field on nine field probes for an elevation of 3 m. The red curve is the average of all nine black curves, and the green curve is the standard deviation of all nine black curves.

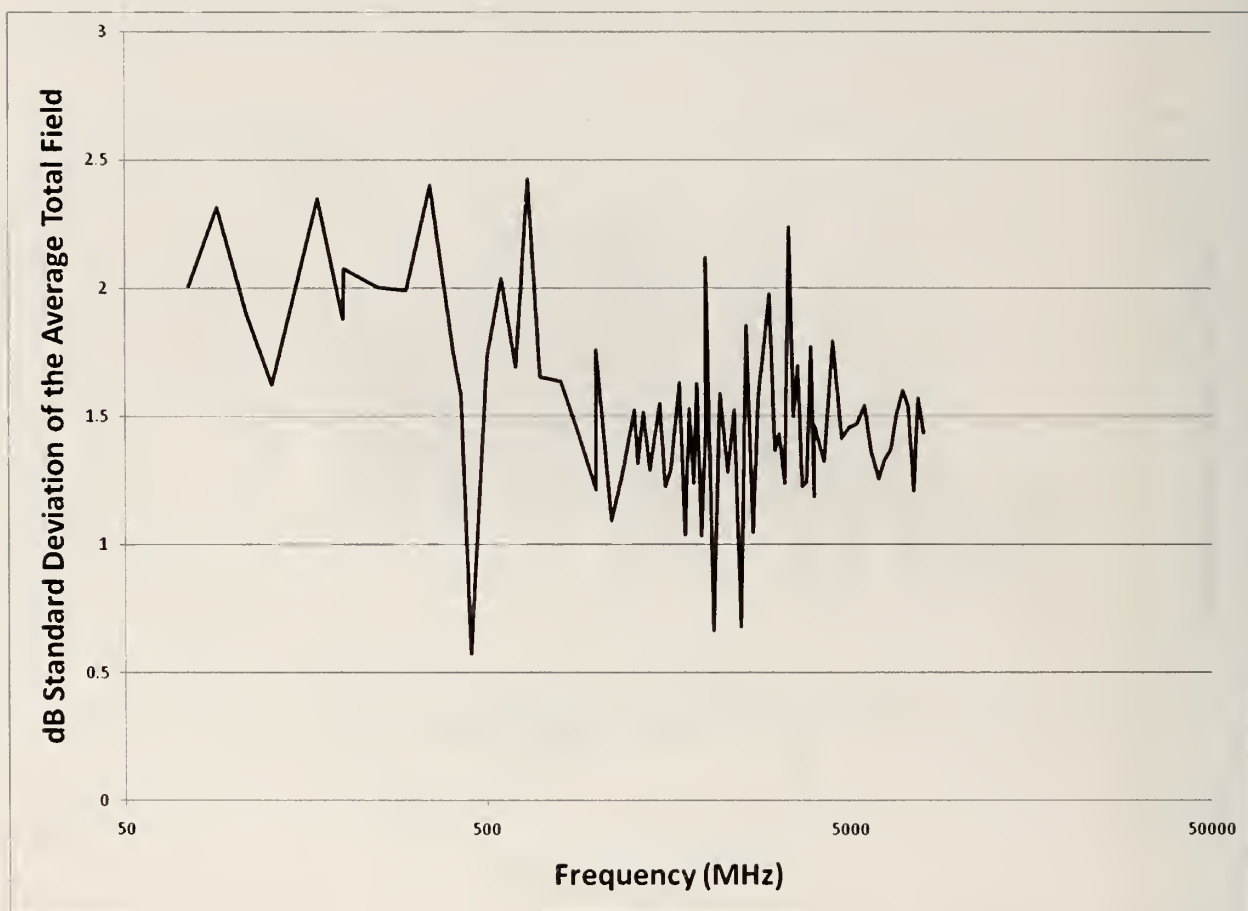


Figure 83. Standard deviation (dB) of the average total field for an elevation of 3 m.

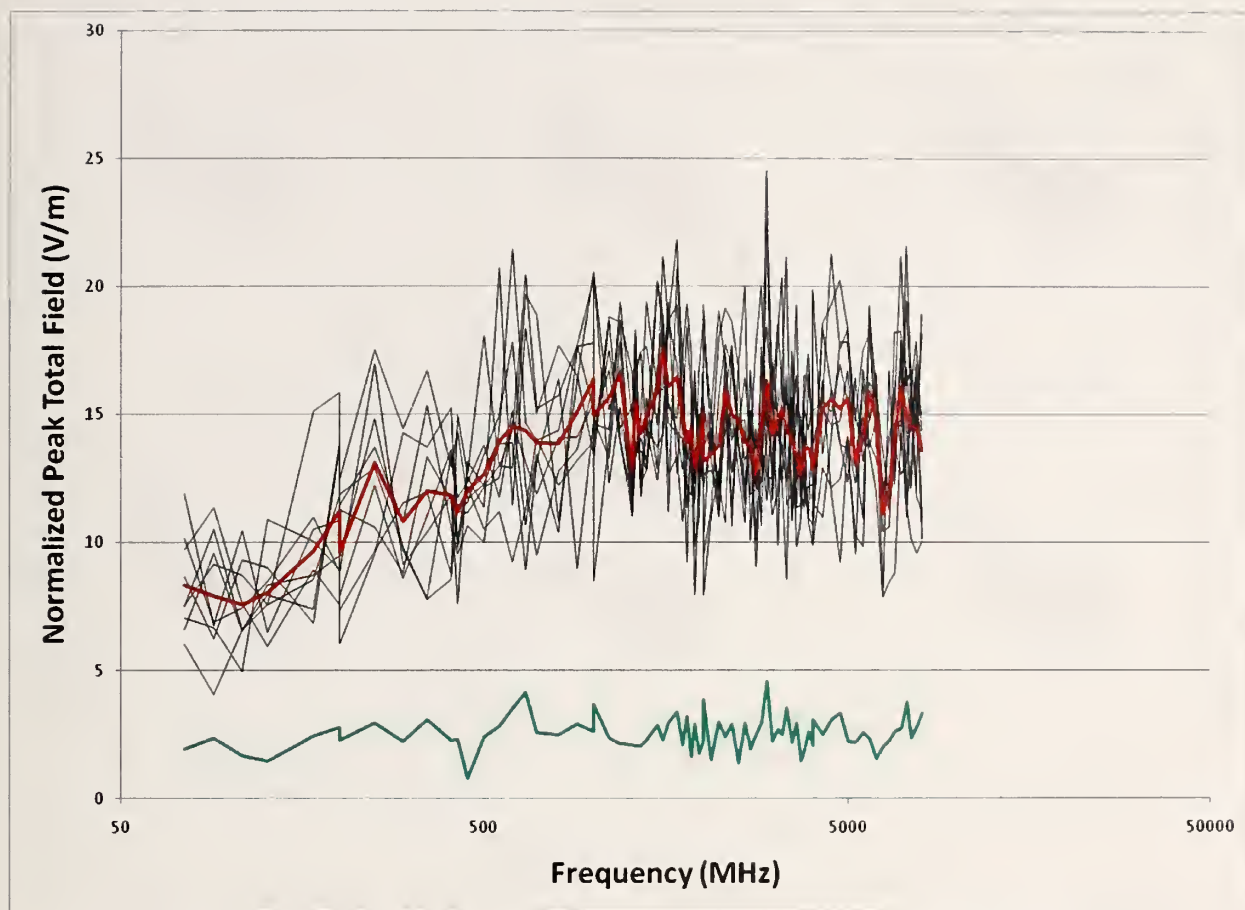


Figure 84. Peak measured total field on nine field probes for an elevation of 3 m. The red curve is the average of all nine black curves, and the green curve is the standard deviation of all nine black curves.

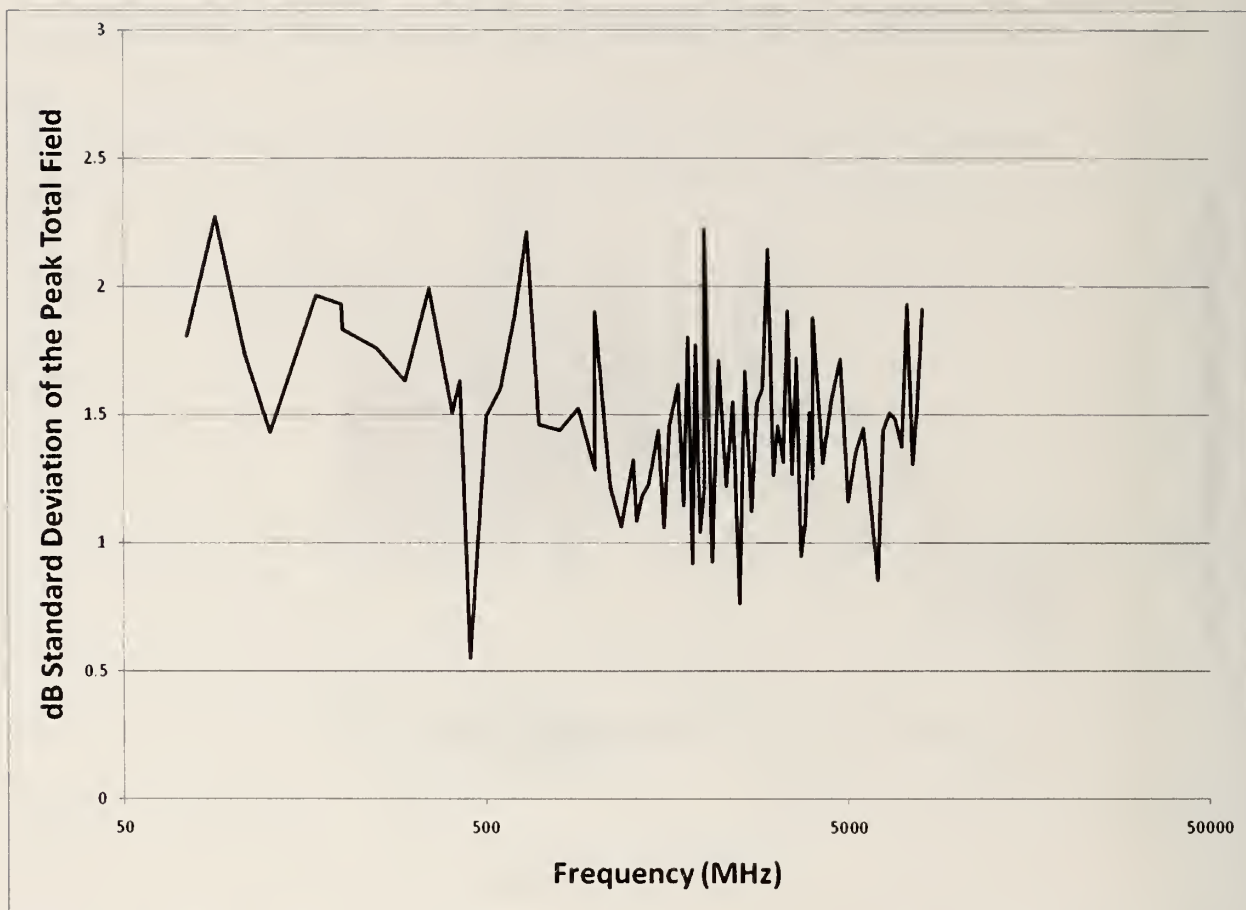


Figure 85. Standard deviation (dB) of the peak total field for an elevation of 3 m.

Similar analyses were performed at each of the 12 elevations (each elevation was roughly equivalent to performing a full chamber evaluation according to the standards). There was nothing at any of the elevations that was significantly different from what we have presented from the 3 m elevation. In all cases, the mean and peak fields showed large variability, but all results were reasonable, given our minimal paddle. We evaluated the dB standard deviation of the peak field, similar to what was done for Figure 81, for each elevation, and the results are shown in Figure 86. Given the small paddle and high variability in the mean field, we expected similarly poor performance in the peak field. However, the chamber would have passed or nearly passed the standard evaluation procedures at every elevation. Frequencies near 500 MHz seemed to be problematic, especially at higher elevations above 20 m. This might be caused by the increased distance from the paddle, or possibly by approaching the dome at the top of the SPF. Most likely, those points that exceed the limit would likely be greatly improved by using a larger paddle.

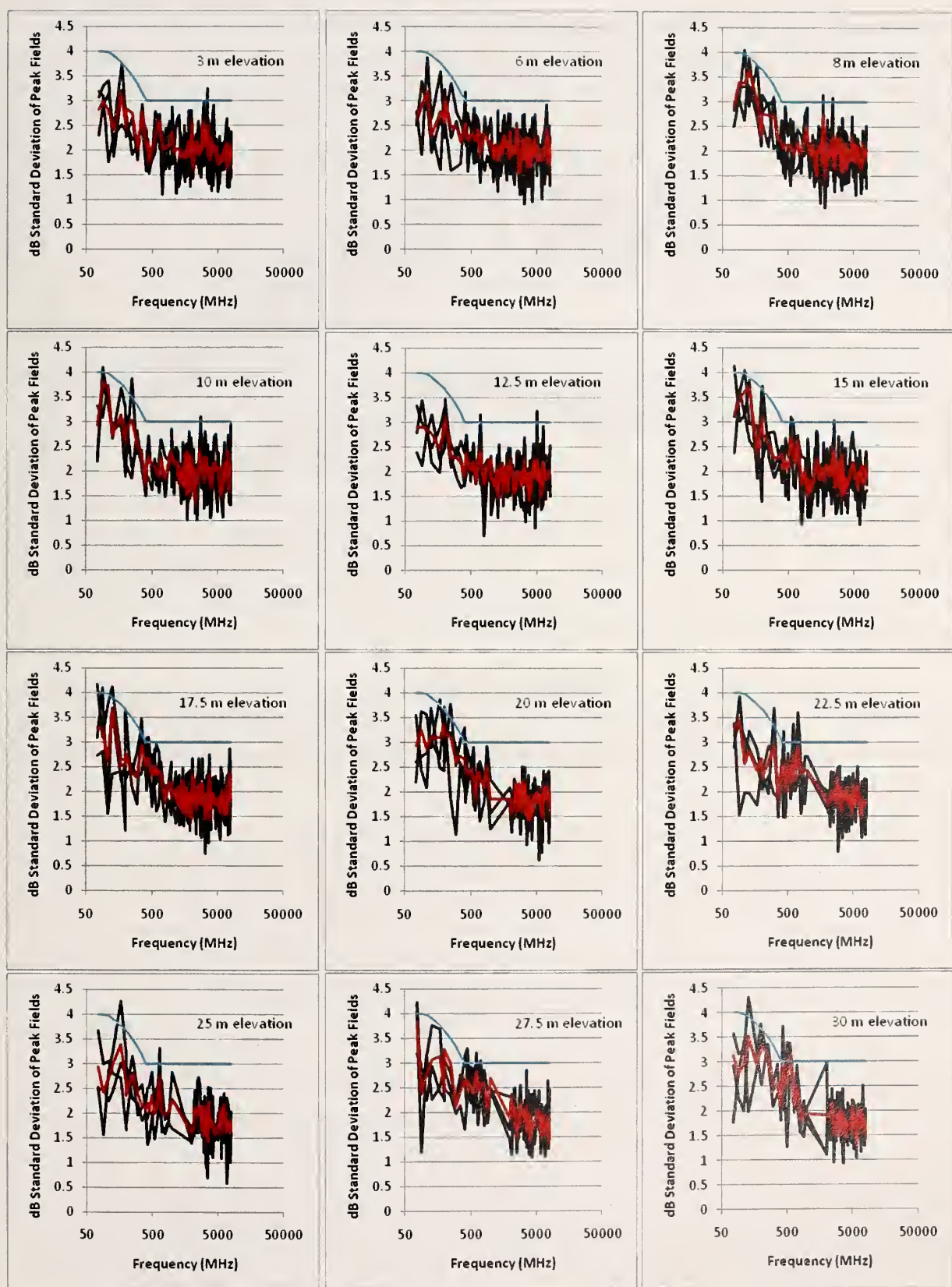


Figure 86. Standard deviation (dB) of peak field for each elevation.

We next computed some overall estimates for the average Cartesian field, average total field, peak Cartesian field, and peak total field, in the chamber. The concept is straightforward, but the explanation is unfortunately cumbersome. We begin with a description of how we computed the average Cartesian field. For each elevation, we computed the field measured on each probe axis averaged over 12 paddle positions to give us 29 measurements of average Cartesian field, as was shown in Figure 76. We then computed the average of those 29 measurements, as was done to generate the red curve in Figure 76. This gave us the field averaged over paddle position, polarization, and location on our probe suspension fixture, for each elevation. Since we performed measurements at 12 different elevations, we now have 12 curves, each representing the average field measured at that elevation. We then averaged those 12 curves (well, actually, since the 1 GHz-2 GHz amp died for elevations above 17.5 m, data between 1 GHz and 2 GHz were averaged over only seven curves). The individual elevation averages are shown as the lower black curves in Figure 87, and the overall average Cartesian field is shown in red.

A similar procedure was used to give an overall average total field. For each elevation, we measured the total field on nine probes at each of 12 paddle positions to give nine measurements of the average total field, as was shown in Figure 82. We then computed the average of those nine curves as was done to generate the red curve shown in Figure 82. This was done at each of the 12 elevations giving us the 12 upper black curves in Figure 87. The average of those 12 curves gives us the upper red curve in Figure 87.

The results shown in Figure 87 can be compared to the predictions based on VNA measurements shown in Figure 72, and the agreement is encouraging, generally agreeing within our measurement uncertainty. These results can be used to establish power requirements for any desired field levels.

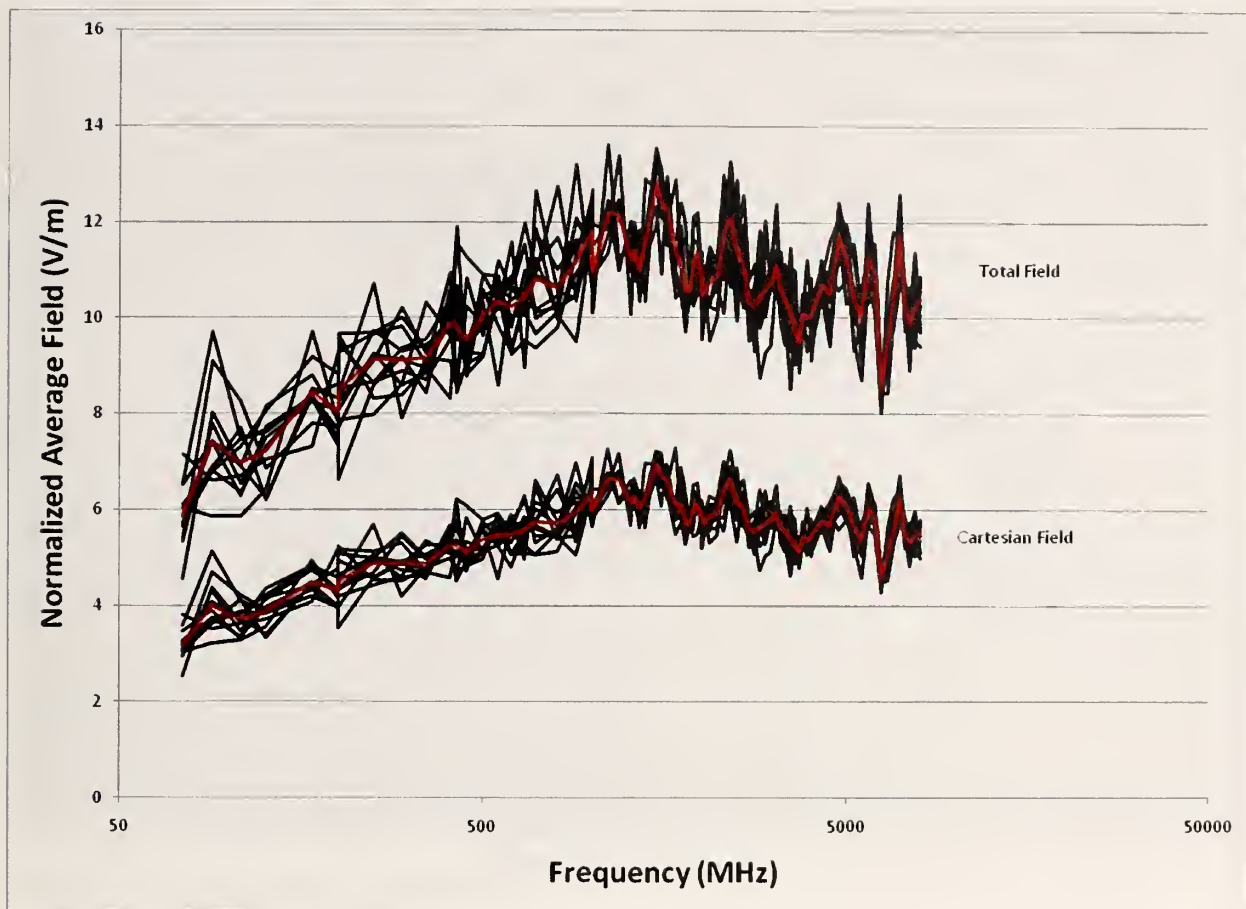


Figure 87. Average field measured at each elevation (black) and the overall average (red) for Cartesian and total field.

The procedure for the maximum fields was similar, but we first computed the peak measured field over the 12 paddle positions, and then averaged these peak measurements. Notice we did *not* determine the peak over polarization, location, or elevation...only over paddle position. Results for the average peak Cartesian field for each elevation are shown as the lower black curve in Figure 88, and the overall average peak field is shown as the lower red curve. The upper black curve shows the average peak total field, and the upper red curve shows the overall average peak total field.

Again, the results shown in Figure 88 are consistent to predictions based on VNA measurements and shown in Figure 73 to within our measurement uncertainty.

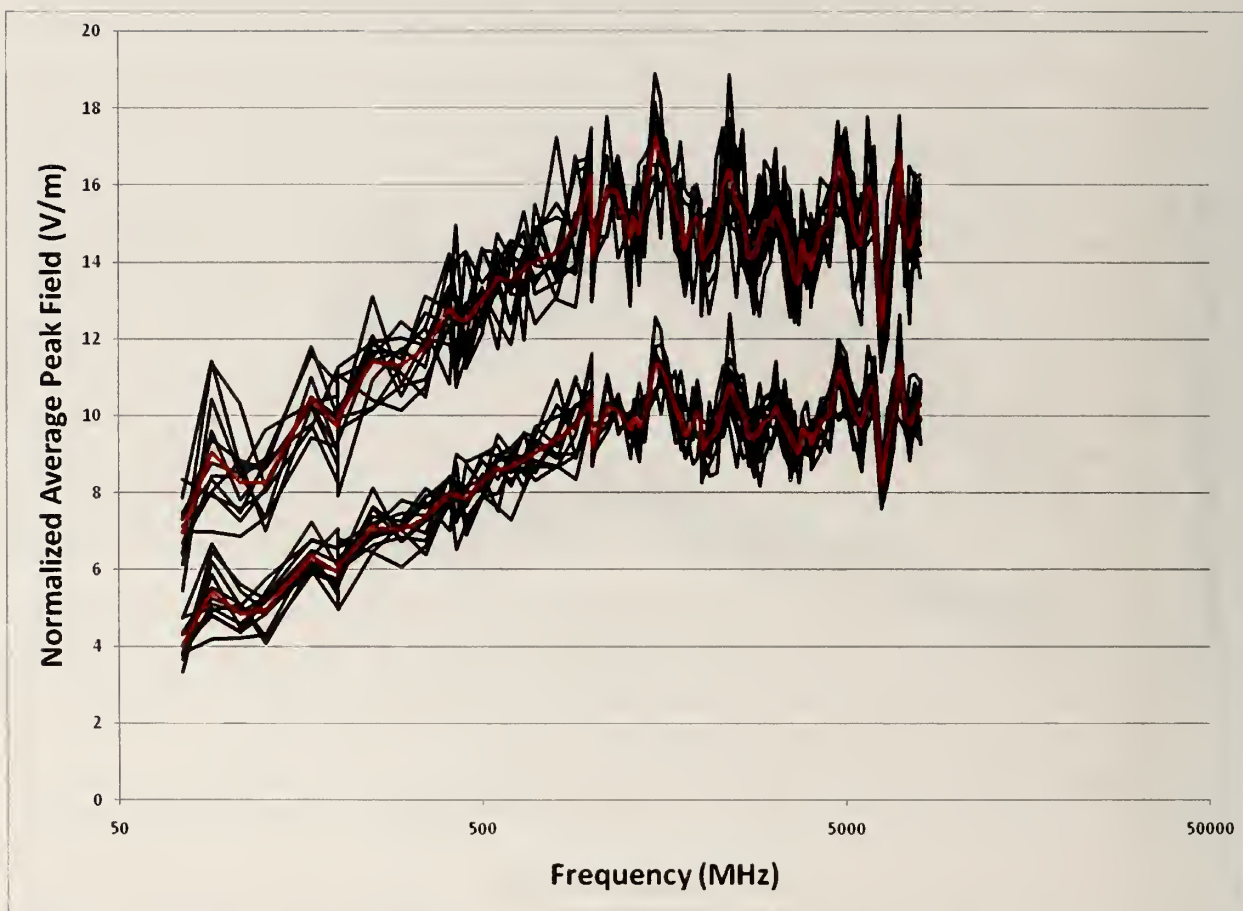


Figure 88. Average peak field measured at each elevation (black) and the overall average (red) for Cartesian and total field.

6.3. Chamber Shielding

Since the SPF was not designed to be an electromagnetic test facility, we did not expect it to demonstrate exceptional shielding. Even though most suspected leakage points were covered with conductive sheets (Figure 89), there was only so much that could be done. One of the expected weak points was the personnel door (Figure 90), which was made of wood and polystyrene foam board covered with aluminum foil.

A detailed shielding evaluation would generally be performed by placing a source inside the SPF and then moving a receiving antenna to multiple locations around the exterior of the chamber. Given the limited time we had for the full evaluation of the SPF, we chose three locations based on expected leakage paths and simplicity of setup: directly outside the personnel door, in an anteroom several feet away but directly in front of the personnel door, and directly in front of the large West door, as shown in Figure 91.



Figure 89. Covering probable leakage points.



Figure 90. Personnel door made of foil-covered polystyrene foam.

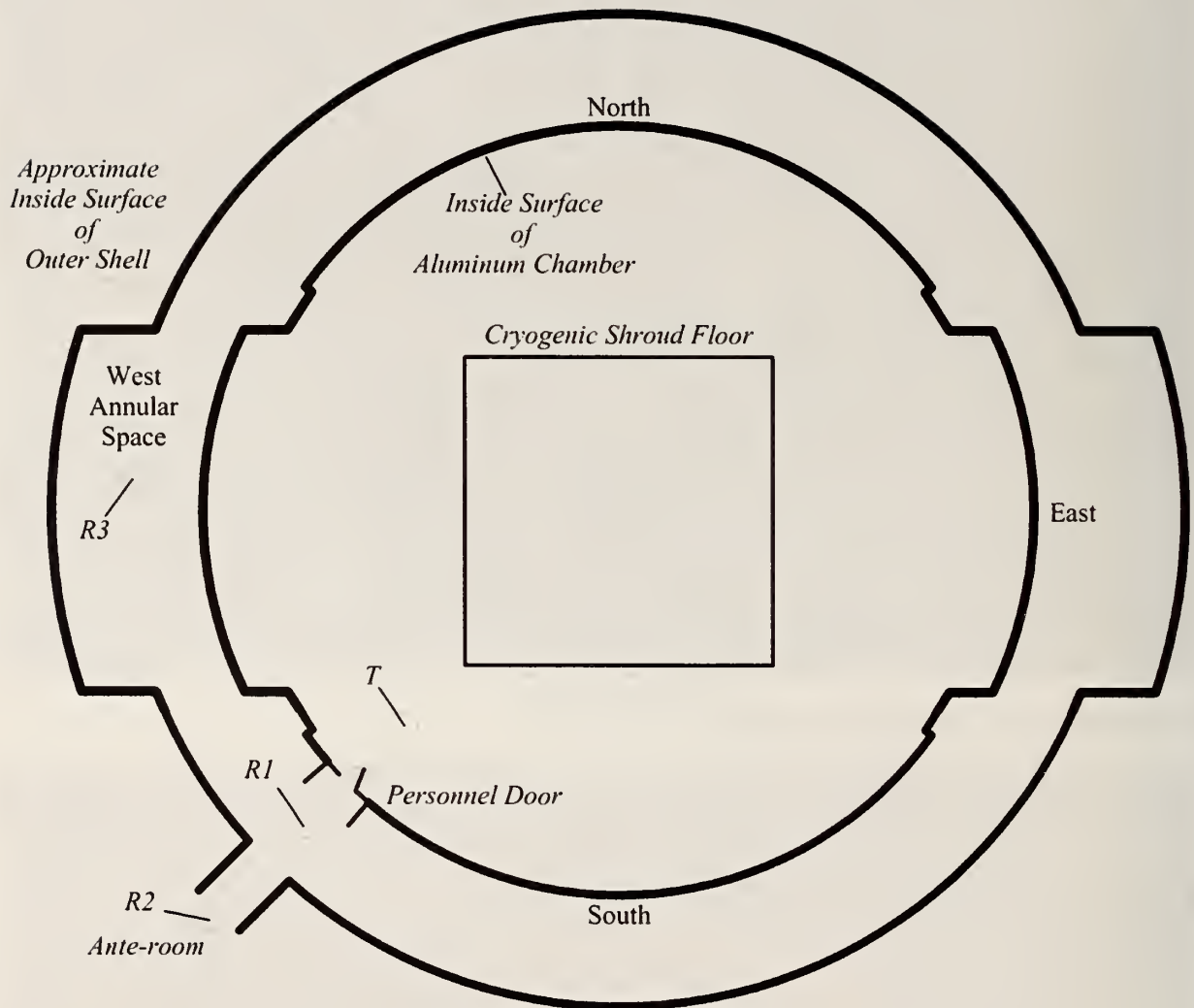


Figure 91. Measurement locations for the shielding tests.

Our measurement system was the VNA system described in section 5.1.1, but the optical cable was passed under the personnel door, and the receiving antenna system was placed at the desired test locations outside the chamber. A mechanical paddle was not used for these measurements. The frequency averaged coupling (inside to outside) was compared to the average coupling (inside to inside) between the transmitting and receiving systems. We defined the difference as the estimated shielding of the SPF. The horn of the mid-band receiving system was directed towards the SPF during the measurements outside the personnel door (R1 in figure 92) and in the

anteroom (R2 in figure 92). Near the west door (R3), we assumed that the door itself, being solid aluminum, would not radiate much, and that most of the radiation would originate from the seams. Since we could not selectively evaluate individual seams, the antenna was given some random orientation.

The estimated shielding using the low-band measurement system is shown in Figure 92. Since this shielding is plotted on a positive decibel scale, the highest red curve indicates the maximum shielding we can determine with our measurement system, and is governed by the noise floor of the system. As a result, the noise floor of our system actually corresponds to a “noise ceiling” on our ability to measure shielding. A shielding of 0 dB corresponds to the same received power measured both inside and outside of the SPF, and high shielding indicates that much less power is received outside of the SPF than inside. Directly outside the personnel door we measured shielding of approximately 35 dB from 100 MHz to 2 GHz. The anteroom showed approximately 40 to 45 dB of shielding, and the large west door showed approximately 55 dB of shielding. This was better than expected, considering that the door had no rf gasketing. These results essentially confirm intuitive practices relating to shielding: keep interfering sources well away from potential leaks, and keep sensitive equipment and personnel away from potential leaks if high-power rf is being transmitted within the chamber.

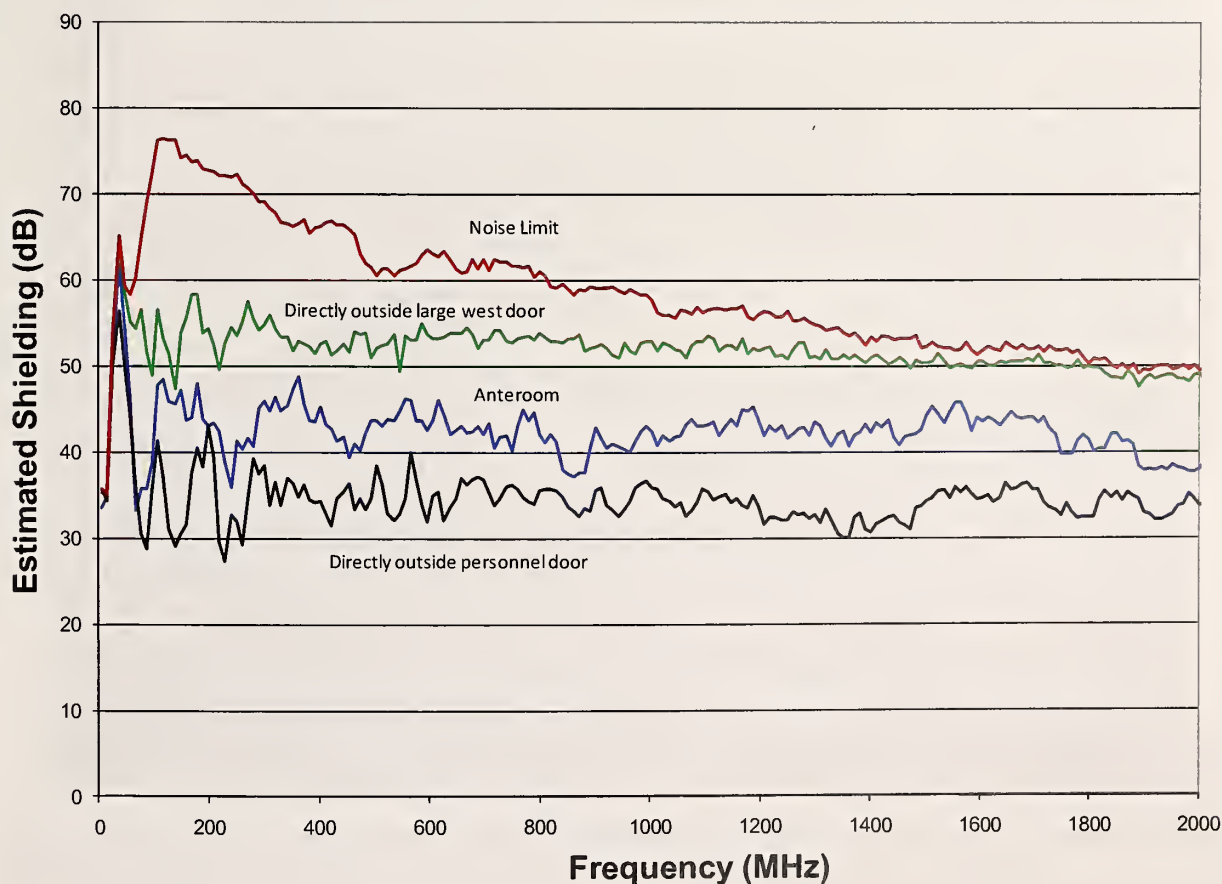


Figure 92. Estimated shielding from low-band measurements.

The estimated shielding using the mid-band system is shown in Figure 93. Here, the noise floor (mostly influenced by the insertion losses between transmitting and receiving antennas) severely limited our ability to estimate shielding above 10.5 GHz. Just outside the personnel door, we observed shielding of between 25 dB and 32 dB from 1 GHz to 14 GHz, and are unable to generate a valid estimate above 14 GHz. In the anteroom we observed shielding between 35 dB and 40 dB from 1 GHz to 10.5 GHz, and are unable to give a valid estimate above 10.5 GHz. Both of these shielding estimates are approximately 10 dB worse than those using the low-band system. This is most likely due to the fact that the horn antennas (with a gain of approximately 10 dB) were directed at the personnel door. Outside the large west door, shielding appears to be approximately 55 dB up to around 9 GHz, with two significant exceptions near 5 GHz and 7 GHz. These leakages will need further evaluation. We cannot give valid estimates of shielding above 9 GHz.

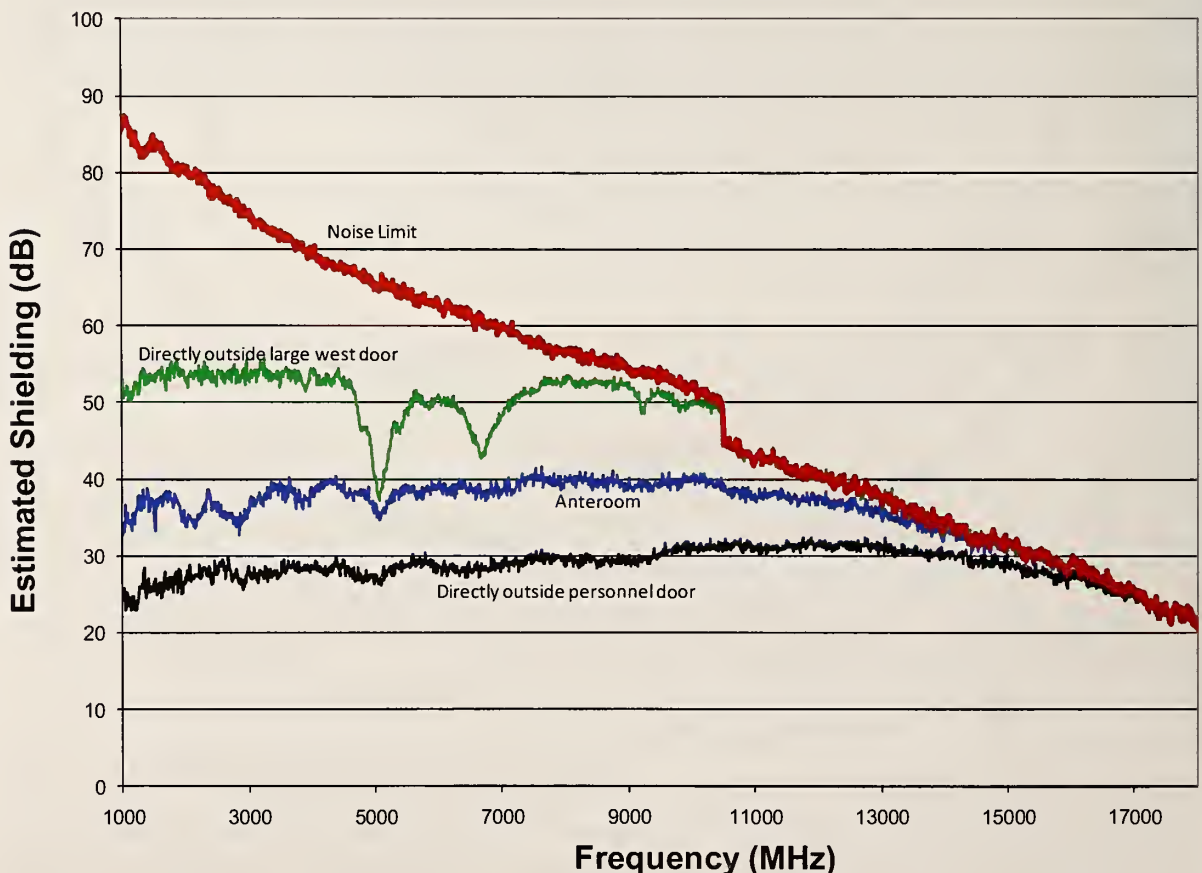


Figure 93. Estimated shielding from the mid-band measurements.

6.4. *Ambient Signals*

The first measurement conducted by NIST personnel upon arriving at the SPF facility involved measuring the ambient signals present in the main SPF chamber. This measurement was conducted by use of two spectrum analyzers each connected to a single antenna. One spectrum analyzer was equipped with a discone antenna, while the other was equipped with a dual-ridge horn antenna. Figure 94 depicts this measurement setup. The measurement was started when the main SPF door was open and ended after the door was closed. Observing this transition gave us the opportunity to see what signals might have been radiating from sources inside the chamber, and what signals might have been penetrating the chamber after all large openings were closed.

This measurement consisted of two complete and independent setups. One setup equipped with the discone antenna measured signals from 10 MHz to 1.01 GHz. The second setup – equipped with the dual-ridge horn – measured signals between 1.0 GHz and 6.0 GHz. Each of the two analyzers was connected to a laptop computer that triggered, recorded and saved data from each sweep of the spectrum. These measurements are almost identical in setup to the measurements NIST conducted at an automotive manufacturing plant [19].



Figure 94. Ambient signal measurement setup of two spectrum analyzers. One with a dual ridged horn (red in color) and the other with a discone antenna. Each connected to a laptop for recording data.

The low-band measurements began at 14:40 on April 14th and ran continuously until 09:52 on April 15th. Each data trace in the low-band was averaged over 100 sweeps and consisted of 8,192 discrete frequencies. Each sweep took approximately 12 ms. This average was saved to the laptop computer and used in all subsequent data processing. High-band measurements began at 15:20 on April 14th of 2009 and ran continuously until 09:38 on April 15th. Similar to the low-band measurements, 8,192 discrete frequency points were measured 100 times and the average saved. The sweep time for high-band measurements was approximately 670 ms. The increased sweep time is due to the increased resolution bandwidth used to help lower the noise floor of the measurement.

Early on the morning of April 15th, the large door to the SPF chamber began to close. The door closing procedure took approximately 2 hours. The spectrum analyzers continued to measure data during this event. Figure 95 gives a clear indication of when the door finished closing – around minute 900 – when measured signals are attenuated down to the noise floor.

Figure 95-Figure 99 show several specific frequency bands of interest in 3-D plot form (Frequency vs. Amplitude vs. Time). In Figure 95 and Figure 96, one can see strong signals present from the start of the measurement until the door was closed. Figure 95 shows the FM radio frequency band. We can be certain that most, if not all, of these signals came from commercial radio stations rather than from sources inside the chamber. For this reason, the signals drop off into the noise floor when the door is closed. Similarly, Figure 96 shows signals in the 900 MHz ISM (industrial, scientific and medical) frequency band are severely attenuated once the door is closed. Again, this gives some indication that these signals were originating from outside the SPF chamber.

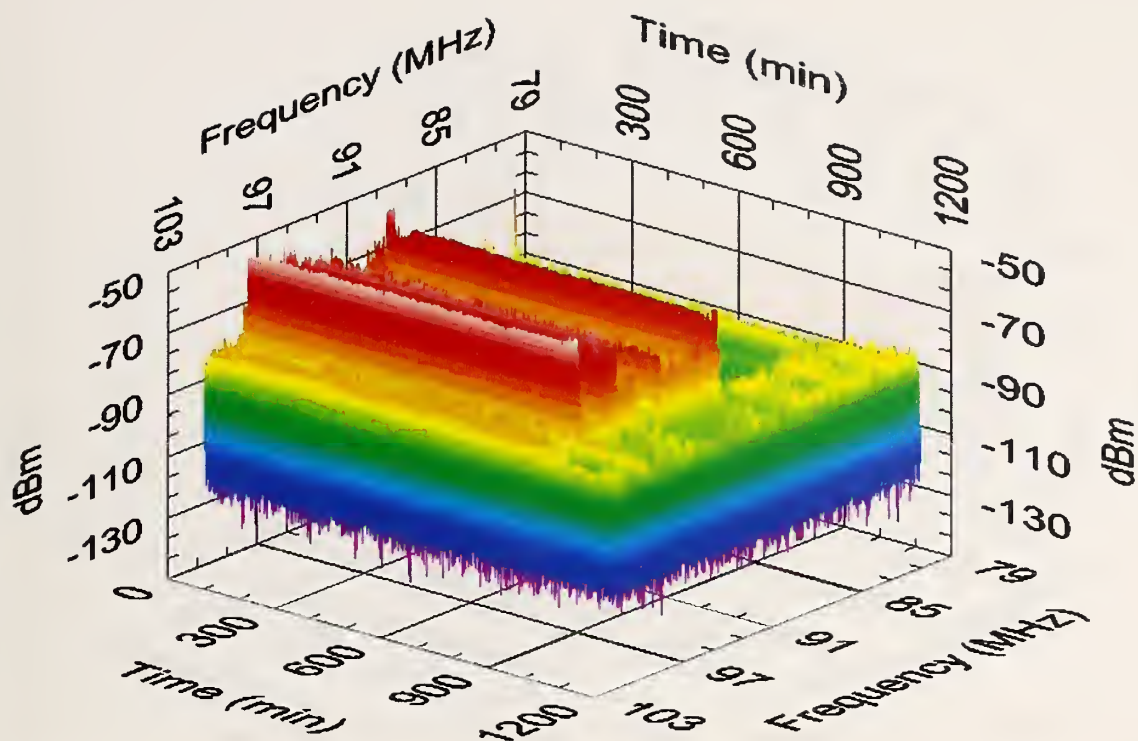


Figure 95. The FM frequency band is shown over the entire duration of the measurement (19 hours, 12 minutes).

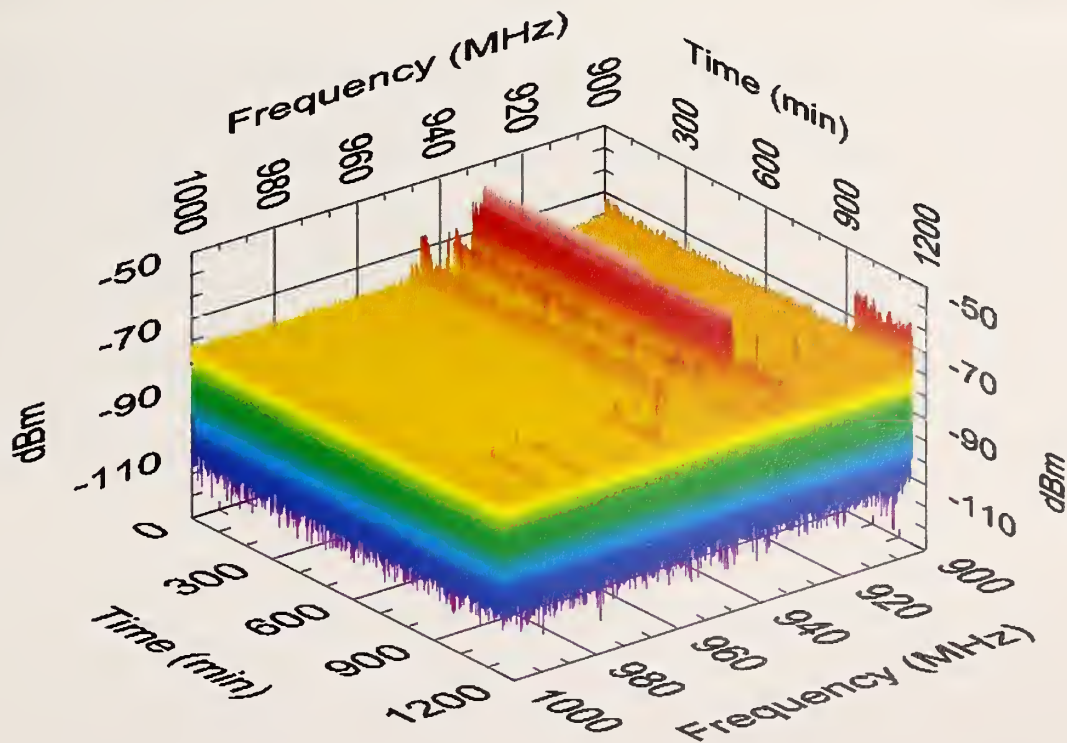


Figure 96. The 900 MHz ISM band is shown over the entire duration of the measurements (19 hours, 12 minutes). The sudden drop off around 900 minutes is a result of the door closing.

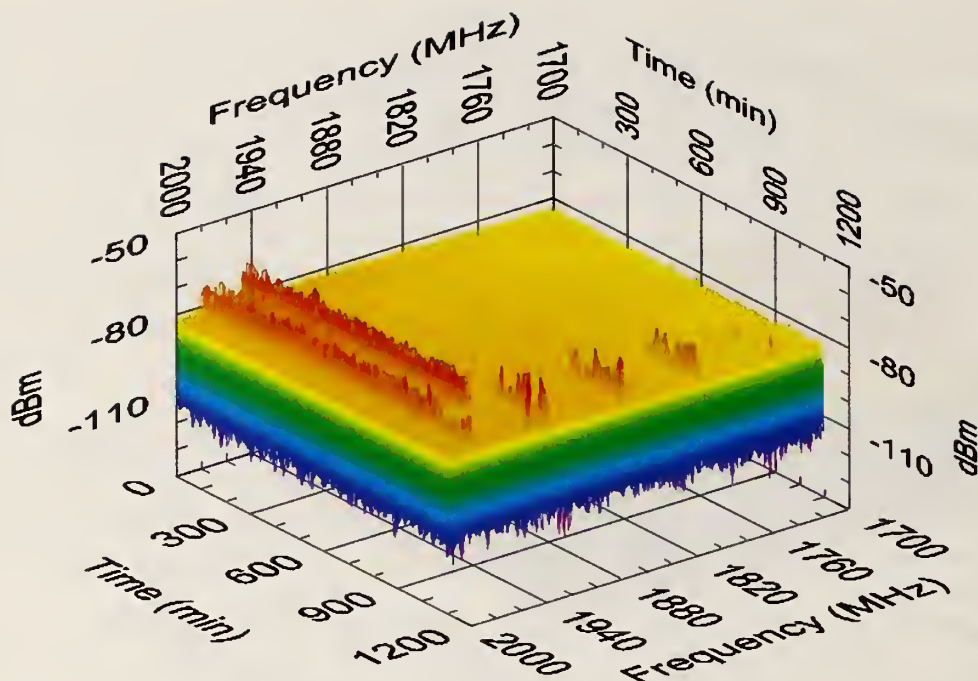


Figure 97. The 1800 MHz cellular phone band is shown for comparison to other active bands.

For comparison, we show the 1800 MHz cellular phone band in Figure 97. In this band, there appears to be little activity, both before and after the door is closed. It is possible that someone inside the chamber had an active cell phone.

While Figure 96, Figure 97, and Figure 98 show an expected decay in ambient activity, Figure 99 and Figure 100 show what appears to be a noticeable increase in ambient activity after the door closes. For these signals, it is reasonable to assume that they are emitting from within the SPF chamber. During the early part of the measurement, these signals propagated through the open door of the SPF chamber, and were not received by the spectrum analyzer. However, with the door closed these signals reverberated throughout the chamber and were received by the spectrum analyzer. The exact source of these signals is unknown. It is possible they are coming from computers or other measurement equipment being operated within the chamber (i.e., spectrum analyzer, laptop, etc.) In addition to the measurement equipment NIST was operating in the chamber, NASA operates cameras and other monitoring equipment inside the chamber that could be a potential source of electromagnetic radiation.

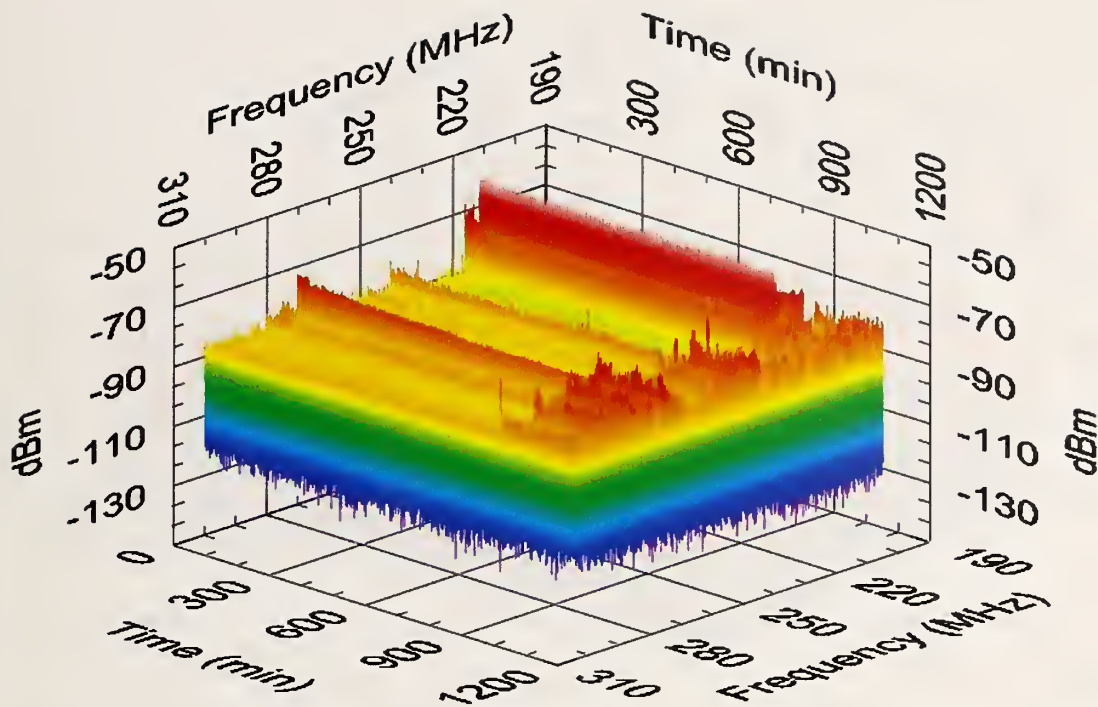


Figure 98. Data between 200 MHz and 300 MHz showing an apparent increase in signal activity after the chamber door closes.

Figure 100 and Figure 101 show an overall summary of the measurement data; both before and after the chamber door was closed. After the measurement was complete, the data were processed and the minimum, median and maximum values were extracted at each frequency. The maximum values in these figures represent the maximum value measured at any point in the measurement. Similarly, the median and minimum values are merely summaries of all of the measured data. The data plotted in this manner should be used in conjunction with the 3-D plots (based on time) to determine whether a signal frequently occurs or is a rare phenomenon. An example of this is Figure 101 where a large spike appears at approximately 3.1 GHz. Referring to Figure 102, it can be seen that the spike is a one-time phenomenon occurring late in the measurement.

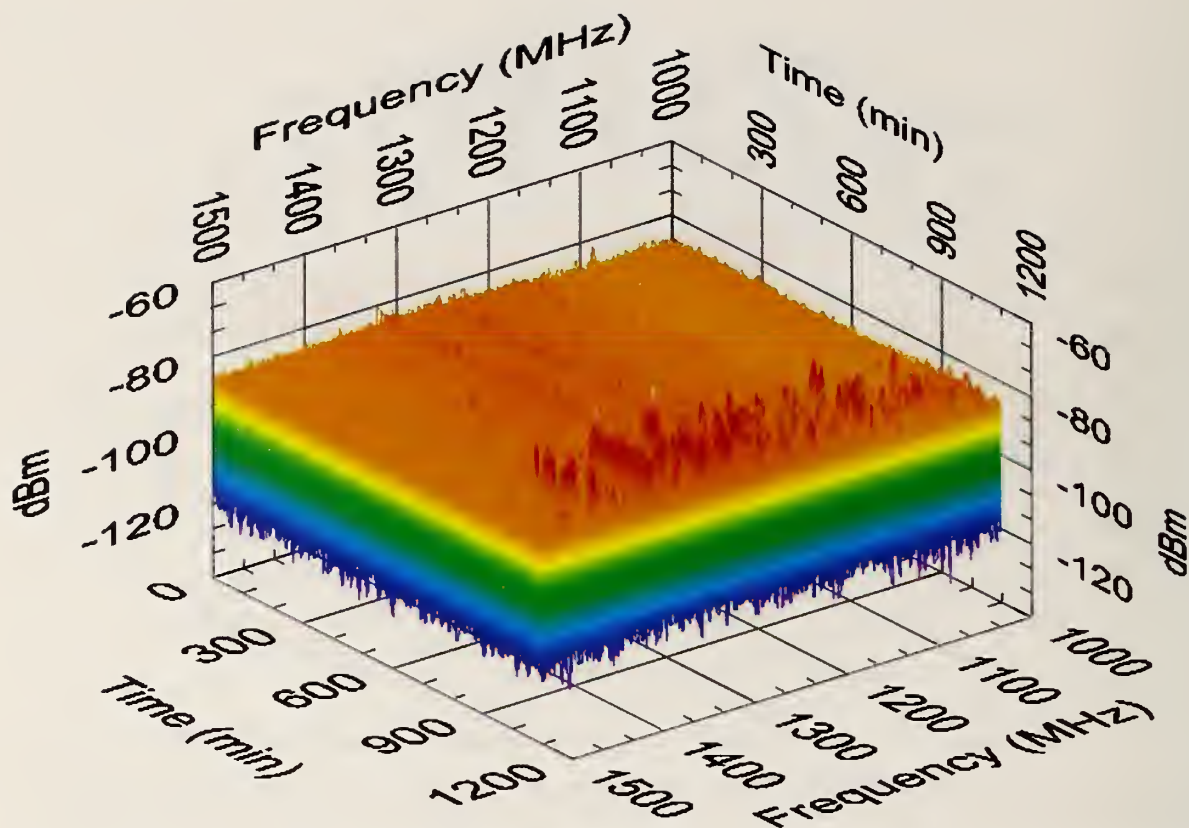


Figure 99. Data between 1.1 GHz and 1.5 GHz that shows what appears to be a distinct increase after the SPF chamber door is closed.

When these data were processed, we added a correction for antenna factor. The antenna factor is a correction that relates the incident field at the aperture of the antenna to a voltage value. After this correction is applied, the results are displayed in dB relative to 1 V/m. Prior to this set of SPF measurements, the antenna factor was measured by use of the two-identical antenna method. Figure 103 shows the antenna factor for both the high and low measurement bands. A higher antenna factor at any given frequency indicates an inability to detect weak signals.

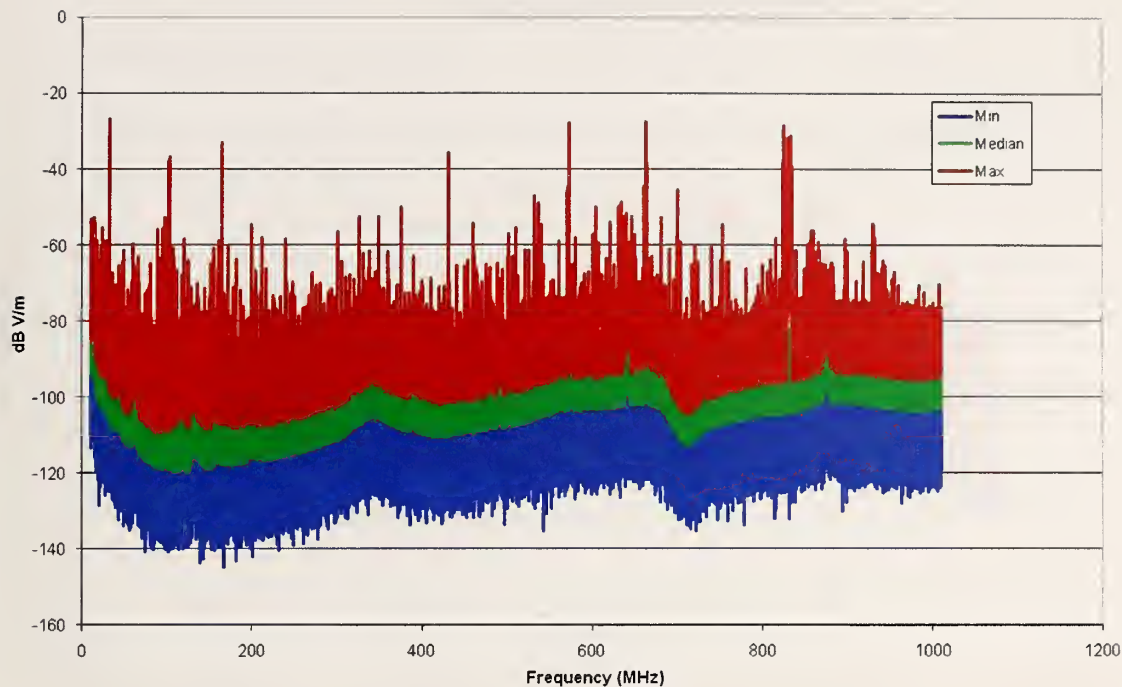


Figure 100. Minimum, median and maximum data (over the duration of the measurement) for the lower frequency band: 10 MHz to 1.01 GHz.

It should be noted that some of these measurements carry large uncertainties (10 dB-20 dB). We intentionally do not state exact uncertainties for these measurements, because their purpose is to show long-term variations and characteristics. The largest contributors to the uncertainties stem from the directional characteristics of the antennas used in the measurements along with the antenna factor correction.

Although the antenna factor is a valid correction for a particular aspect angle, it varies based on the directional gain of the antenna. If a signal arrives at the antenna from a different angle – or in this case, many angles – the correction can yield errors of several decibels. The discone antenna used in the lower band was omnidirectional, and is therefore susceptible to additional errors caused by the antenna factor. For omnidirectional antennas, antenna factor corrections are valid only in the horizontal plane (zero-degree elevation). Again, with signals arriving at the discone antenna from multiple angles, errors are introduced when the data are corrected with the antenna factor. For a complete derivation of antenna factor, refer to [20].

The antenna factor can be used as a measure of how sensitive an antenna is at any given frequency. The higher the antenna factor, the less sensitive the antenna, and the more difficult it is to detect weak signals. In this measurement, the noise floor of the spectrum analyzer is relatively flat, and the antenna factor becomes the limiting factor when ambient signals are measured. Figure 103 gives a good idea of the shape of the effective noise floor for this measurement.

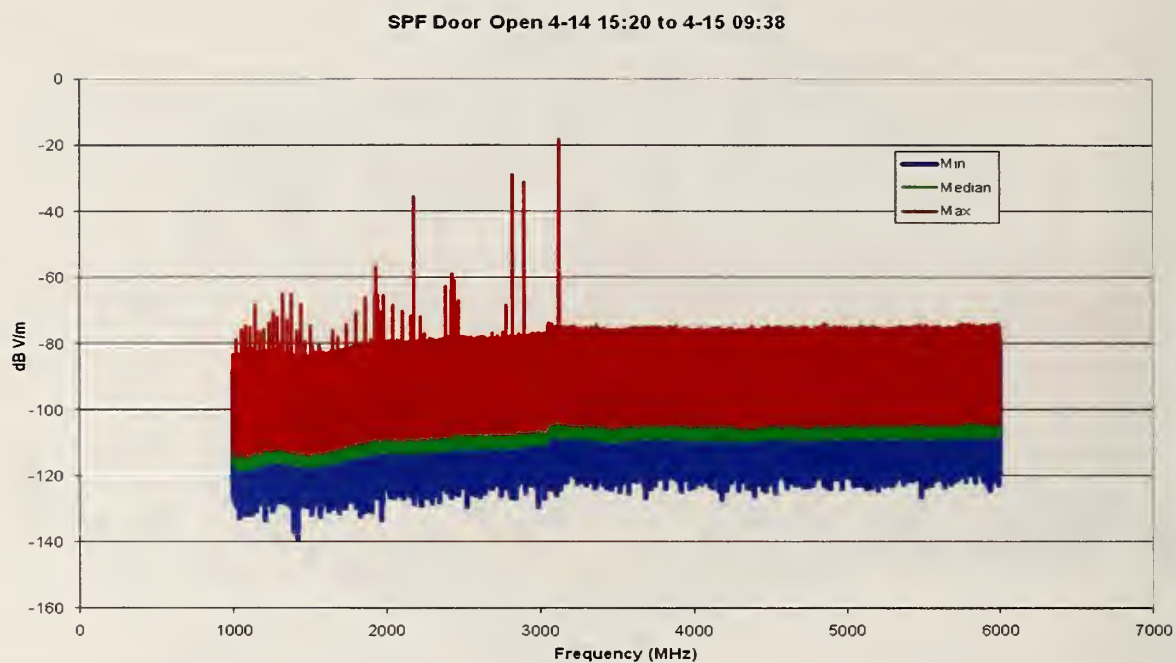


Figure 101. Minimum, median and maximum data (over the duration of the measurement) for the lower frequency band: 1GHz to 6 GHz.

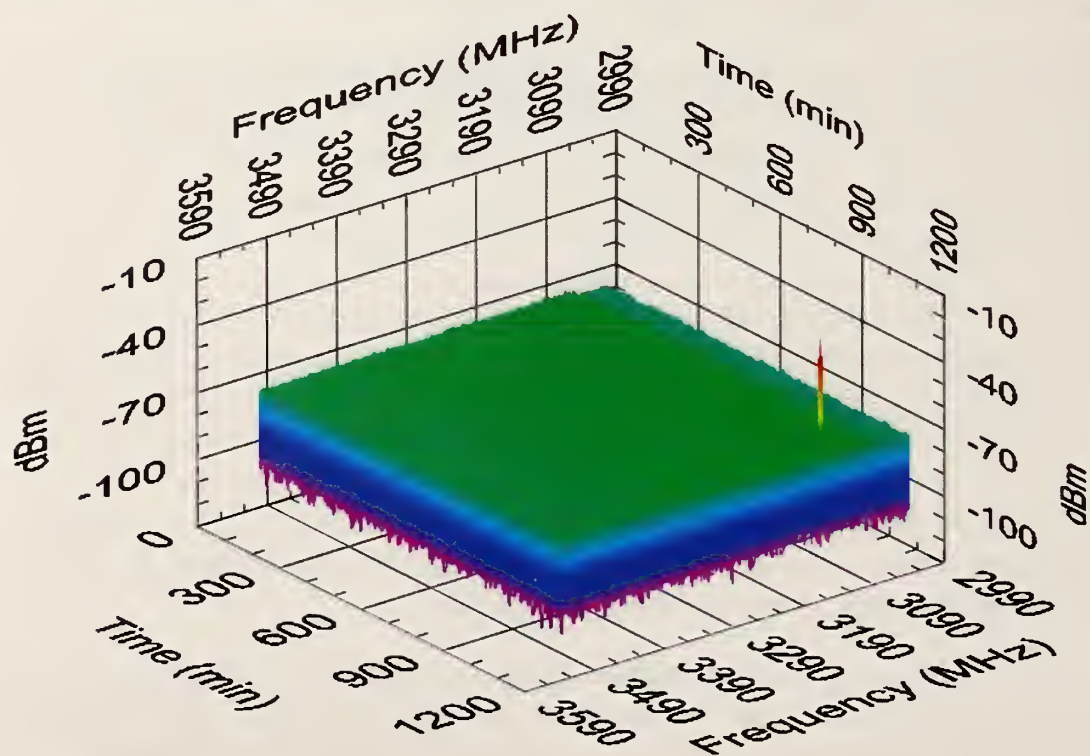


Figure 102. Data between 3 GHz and 3.5 GHz that show the single spike reflected in the percentile plot (Figure 101).

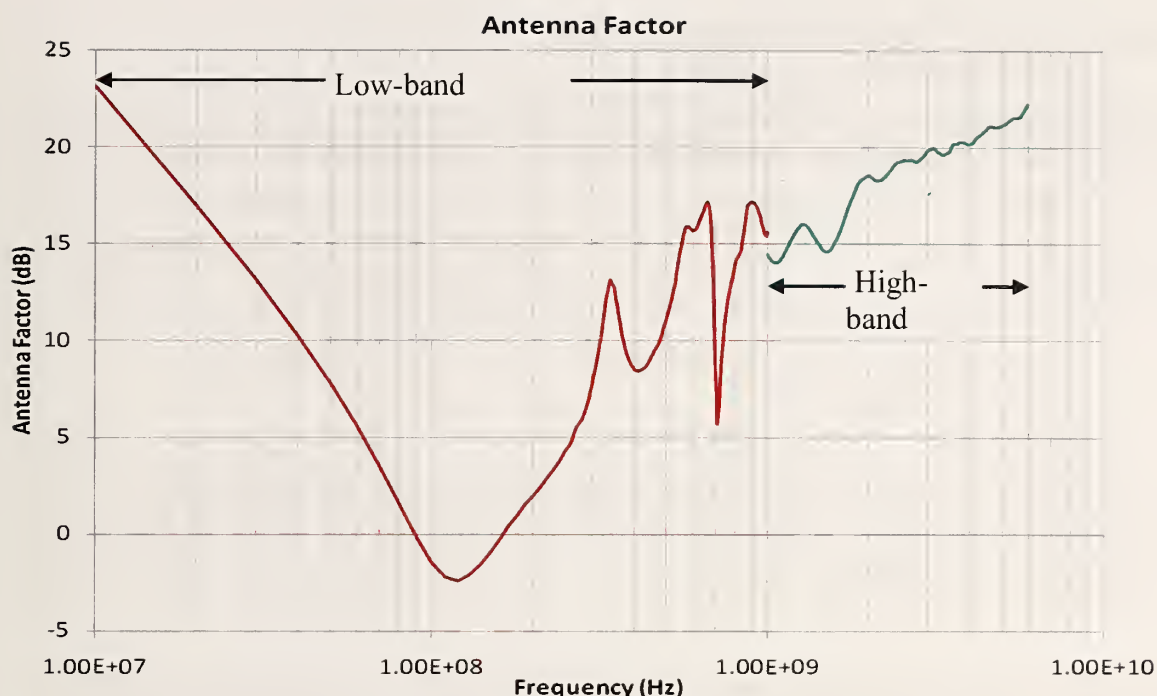


Figure 103. Antenna factor vs. Frequency (log scale) over both high and low-bands. The discontinuity at 1 GHz is a result of the switch from the discone antenna to the dual-ridged horn.

The data plotted on 3-D plots (Figure 95 - Figure 99) are given in units of dBm. These units reflect what was measured at the test port of the spectrum analyzer. Therefore the measurements, shown in dBm, have uncertainties on the order of a few dB, rather than 10+ dB, as with the measurements presented in dB V/m. The data given in dBm should be interpreted with caution. They represent what was measured at the test port, not the antenna; they have not been corrected for cable losses. Because this measurement was designed to measure ambient signals, it may not be reliably repeatable as we have little or no control over the source of the signals. The same test, with identical setup, repeated at a different location within the SPF chamber could yield different results. Although the dBm results are more accurate than those in dB V/m, they are best used to show the statistical behavior of ambient signals in and around the SPF chamber.

7. Uncertainty Considerations

The uncertainty considerations regarding the measurements performed in the NASA SPF are very similar to those associated with our evaluation of the NASA Langley Research Center Mode-Stirred Chamber Facility [14], and we will repeat some of that information here.

The uncertainty in our measurements consists of three individual components, and these three components are then combined to produce a total combined uncertainty. The three components are:

1. Uncertainty due to the random nature of mode-stirred chamber measurements,
2. Residual, unexplained uncertainty (imperfections in chamber),
3. Instrumentation uncertainty.

Uncertainty due to the random nature of mode-stirred chamber measurements will be present in any measurement performed in such a facility. This is essentially the uncertainty that would be observed if the chamber and the associated instrumentation were perfect. As explained in [14], every measurement will have an ideal distribution associated with it, and therefore an uncertainty associated with it. In general, we can characterize the distributions, and hence the uncertainty, very well. Therefore, we can estimate the uncertainty of any parameter associated with mode-stirred chamber measurements (received power, electric field (total or rectangular component), etc.) and, for each parameter, we can estimate the uncertainty associated with the average or maximum of each parameter as a function of the number of paddle positions. Unfortunately, since each parameter has a different distribution and since the distribution for the maximum of a distribution is different from the distribution for the average, the associated uncertainties must be addressed separately. These uncertainties have already been evaluated in [14], and will be tabulated for our measurements below.

No chamber is perfect, and there will be an increase in the total uncertainty due to imperfections. We will group all possible imperfections together and call them collectively non-ideal spatial uniformity (a sensor will consistently measure different values depending on where it is placed in the chamber). Non-ideal uniformity can be caused by a variety of factors, such as an electrically small paddle, direct coupling between the transmitting antenna and a sensor, or an incorrect statistical model.

The uncertainty of our measurement system will generally be small relative to the other components, and should be nearly identical to those presented in [14], since we are using very similar instrumentation.

Table 6. Uncertainty in an ideal chamber for 141 samples.

Quantity	Standard uncertainty for the	
	average (dB)	maximum (dB)
Received power	0.37	0.95
Cartesian electric field	0.38	0.95
Total electric field	0.22	0.7

Table 7. Uncertainty in an ideal chamber for 12 paddle positions.

Quantity	Standard uncertainty for the	
	average (dB)	maximum (dB)
Received power	1.3	1.8
Cartesian electric field	1.3	1.8
Total electric field	0.74	1.1

7.1 Uncertainty due to Random Nature of Mode-Stirred Chamber Measurements

The uncertainty associated with ideal measurements in an ideal mode-stirred chamber can be taken directly from the descriptions given in [14]. A summary of these uncertainties is given in Table 6 for 141 samples and Table 7 for 12 samples. All uncertainties are given in terms of decibels. All of the uncertainties listed here can be characterized as type A uncertainties: those which are evaluated by statistical methods.

7.2 Estimation of the Standard Uniformity

We estimate the standard uniformity of the SPF using the VNA system and frequency averaging based on the standard deviation shown in Figure 68. Here we see that over a large portion of the frequency range (say, from 100 MHz to 5 GHz) the observed standard deviation is very close to the ideal standard deviation of 0.37 dB. Over this frequency range we can estimate that the standard uniformity of the chamber is significantly better than 0.37 dB, and the measurements we performed were not sufficient to determine the actual level. Above 5 GHz, there is a slight increase in the standard deviation. In our opinion, most of this increase can be attributed to instrumentation uncertainty (especially repeatability of cables and connectors). Even if we assume that the entire increase in the observed standard deviation, which is approximately 0.6 dB above 18 GHz, is due to chamber imperfections, then this implies that the standard uniformity is less than 0.5 dB. Below 100 MHz, the data are insufficient to give a good estimate, but the standard uniformity appears to be approximately 2 dB near 70 MHz and rapidly drops below 0.5 dB at 100 MHz.

These estimates are based on the assumption that anomalous results are not indicative of actual nonuniformities in the SPF. If this assumption is not valid, the estimates of the standard uniformity will be worse. For example, anomalies shown in Figure 61, if included, would boost the standard uniformity estimate to approximately 0.9 dB near 1.5 GHz, and to approximately 2 dB near 10 GHz. Similarly, the anomalies shown in Figure 63 would boost the standard uniformity to approximately 1.1 dB near 19.5 GHz, and those shown in Figure 64 would boost the standard uniformity to between 1 dB and 2 dB over most of the spectrum above 18 GHz. Surprisingly, the standard uniformity is low in both sets of data near 33 GHz (the large unexplained notch). This is because, even though we have assumed that there is no such notch in the SPF response, the measurements near this notch are quite repeatable.

For measurements using the probe system, the standard uniformity is much worse than that observed with the VNA system. For average Cartesian field, we expect a standard deviation of about 1.3 dB, but the observed standard deviation, looking at all measurements combined, is about 2.2 dB for frequencies greater than 800 MHz. This implies that the standard uniformity of Cartesian field is approximately 2 dB. Below 800 MHz, the standard uniformity climbs to about 3.4 dB at around 90 MHz.

For total field, things are a little better. The expected standard deviation is about 1.1 dB, but the observed standard deviation is about 1.4 dB above 1 GHz. This implies a standard uniformity of around 1 dB. Below 1.1 GHz, the standard uniformity rises to approximately 2.1 dB

For maximum Cartesian field, we expect a variation of around 1.8 dB. Above 1.1 GHz, the observed standard deviation is about 2 dB, which implies a standard uniformity of less than 1 dB. Once again, this seems to show that the peak field is better behaved than the average field, which is unexpected because the uncertainty of the peak field in an ideal chamber is always larger than the uncertainty of the corresponding average field. Below 1.1 GHz, the standard uniformity rises to approximately 3 dB at 75 MHz.

Finally, for maximum total field, the expected variation is around 1.1 dB. Above 1.1 GHz, the observed variation is about 1.3 dB, which implies a standard uniformity of less than 1 dB. Below 1.1 GHz, the standard uniformity rises to approximately 2 dB at 75 MHz.

8. Conclusions and Recommendations

The Space Power Facility vacuum chamber is the largest highly conductive complex cavity that the NIST team has ever been challenged to evaluate as a possible electromagnetic test chamber. We anticipated that this chamber would possibly exhibit behavior peculiar to the circular and spherical geometry (i.e., energy focusing and poor uniformity) that may limit the usefulness as a

reverberation chamber. However, we were unable to find evidence of those characteristics in the measurement data. The data indicate that the chamber functions quite well as a reverberation chamber over the entire range of our tests (100 MHz – 40 GHz). After sampling over 141 closely spaced but independent frequencies, the standard deviation over the test locations varied from 0.4 dB – 0.45 dB up to 18 GHz, very close to the ideal chamber value of 0.36 dB. The standard deviation increased above 18 GHz but there were fewer test positions, some measurement anomalies and equipment limitations that may have masked the chamber characteristics. The overall conclusion from this sampling was that the chamber exhibited surprisingly good field uniformity and performed very much like an ideal reverberation chamber. In addition to field uniformity we calculated attenuation, decay time, mode bandwidth, quality factor (Q), and electric field related to input power from the insertion loss data collected by use of the network analyzer system. These results show that the chamber has a very high quality factor (Q) exceeding 10^6 at frequencies above 10 GHz. This means that impulsive signals will have a very long decay time and hence pulsed rf testing will require more investigation.

As a complement to the measurements using the network analyzer, we assembled a system of probes and sampled the electric field at a variety of locations in the chamber. The radio frequency signals were radiated into the chamber by use of a transmit antenna aimed into a small rotating paddle. While this paddle did provide a few sample points for the probe measurements, it was too small to effectively stir the large chamber, since we would prefer to have a paddle with at least one dimension that is comparable to at least one dimension of the chamber. The small paddle, and the inability to utilize frequency averaging, caused the variation in the probe measurement data to be larger than what was shown by the network analyzer tests. We conclude that the uniformity of the chamber is much better than indicated by the probe data. However, even with these measurement issues, the data show the chamber is suitable for testing based on common standards. A more effective paddle along with some frequency and spatial averaging would greatly improve the statistical quality of the field data in the chamber.

The amount of loading caused by the cryo-floor was very small (typically < 1dB) and this structure will not significantly impact the field strength in the chamber. Measurements also show that the cryo-floor did not impact the field uniformity.

A test was performed to examine the shielding of the chamber. We measured the insertion loss from inside to various points in the annulus region between the aluminum inner chamber and the larger concrete and steel outer shell. While the approximate 30 dB of attenuation (shielding) may be adequate for low power tests, we recommend that it should be improved if higher power levels are used in the chamber. A proper shielded door for personnel is the most obvious possible improvement, in addition to shielding other known apertures and cable penetrations.

9. Acknowledgements

The authors acknowledge the technical and financial support of NASA John H. Glenn Research Center and in particular, Kurt Shalkhauser, Noel Sargent, and Catherine (Cathy) Lewis. We extend special appreciation to the staff at the Plum Brook Station facility for the superb logistic and operational support during our measurements. We acknowledge the advice and helpful technical discussions with David Hill of NIST, Robert Johnk and Paul McKenna of ITS, and Mike Hatfield from NSWC. We also thank the other members of the NIST RF Fields Group for support in the preparation and execution of the measurement program. And, last but not least, we thank Michael Francis and Perry Wilson for continued support and encouragement during the project.

10. References

- [1] AECOM. Edwards Air Force Base, Benefield Anechoic Facility. *dmjmh.aecom.com*. [Online] [Cited: August 20, 2009.] <http://www.dmjmh.aecom.com/MarketsAndServices/39/54/index.html>.
- [2] Goldsmith, K.R. and Johnson, P.A. *Design, construction, computational EM modelling, and characterization of an aircraft sized reverberation chamber and stirrer*. 31 Oct. - 7 Nov 1998. Digital Avionics Systems Conference, 1998 Proceedings 17th DASC, AIAA/IEEE/SAE. pp. Volume 1, Pages(s): D55/1 - D55/8.
- [3] Hatfield, M.O., Freyer, G.J. and Slocum, M.B. *Reverberation characteristics of a large welded steel shielded enclosure.. s.l. : IEEE International Symposium on Electromagnetic Compatibility, Aug. 1997. Pages: 38-43.*
- [4] RTCA/DO-160E. *Environmental Conditions and Test Procedures for Airborne Equipment*. s.l. : RTCA, Inc., 2004. DO-160E.
- [5] MIL-STD-461F. *Requirements for the Control of Electromagnetic Interference Characteristics of Subsystems and Equipment*. s.l. : U.S. Dept. of Defense, 2007. MIL-STD-461F.
- [6] IEC-61000-4-21. *Electromagnetic compatibility (EMC) - Part 4-21: Testing and measurement techniques - Reverberation chamber test methods*. Geneva, Switzerland : International Electrotechnical Commission, 2003. IEC 61000-4-21.
- [7] Hill, David A. *Electromagnetic Theory of Reverberation Chambers*. Boulder, Colorado : US Department of Commerce, National Institute of Standards and Technology, 1998. Technical Note 1506.

- [8] Hill, D.A., Ma, M.T., Ondrejka, A.R., Riddle, B.F., Crawford, M.L., Johnk, R.T. *Aperture excitation of electrically large, lossy cavities*. s.l. : IEEE Transactions on Electromagnetic Compatibility, August, 1994, Vols. 36, pp. 169-178.
- [9] Crawford, M.L., Koepke, G.H. and Ladbury, J.M. *EMR Test Facilities Evaluation of Reverberating Chamber located at RADC, Griffiss AFB Rome, New York*. Boulder, CO : National Institute of Standards and Technology, 1987. NBSIR 87-3080.
- [10] Lunden, O. and Backstrom, M. *Pulsed Power 3 GHz Feasibility Study for a 36.7 m³ Mode Stirred Reverberation Chamber*. s.l. : IEEE International Symposium on Electromagnetic Compatibility, July, 2007. Pages(1): 1-6.
- [11] Lunden, O. and Backstrom, M. *Absorber loading study in FOI 36.7 m³ mode stirred reverberation chamber for pulsed power measurements*. s.l. : IEEE International Symposium on Electromagnetic Compatibility, Aug. 2008. Page(s): 1-5.
- [12] Ely, Nguyen, Scarce, “The influence of modulated signal risetime in flight electronic radiated immunity testing with a mode-stirred chamber”, NASA/TM-2000-209844.
- [13] Arnaut and Knight, “Observation of coherent precursors in pulsed mode-stirred reverberation fields”, Physical Review Letters, 2 Feb 2007
- [14] Ladbury, J., Koepke, G., Camell, D. *Evaluation of the NASA Langley Research Center Mode-Stirred Chamber Facility*. Boulder, CO : US Department of Commerce, National Institute of Standards and Technology, 1999. NIST TN1508.
- [15] Hill, David A. *Electromagnetic Fields in Cavities: Deterministic and Statistical Theories*. John Wiley and Sons, New York, 2009.
- [16] NDT Resource Center. *Conductivity and Resistivity Values for Aluminum & Alloys* [Online] [Cited: March , 2010.] http://www.ndt-ed.org/GeneralResources/MaterialProperties/ET/Conductivity_Al.pdf.
- [17] Hill, D.A., Ma, M.T., Ondrejka, A.R., Riddle, B.F., Crawford, M.L., Johnk, R.T. *Aperture Excitation of Electrically Large, Lossy Cavities*. Boulder, CO : US Department of Commerce, National Institute of Standards and Technology, 1993. NIST TN 1361.
- [18] Johnk, R.T., Ewan, J.D., McKenna, P., Carey, R.L., DeMinco, N., Shalkhauser, K.A. Time-Domain Pulsed Measurements of the NASA Space Power Facility; IEEE 2009 EMC symp proceedings; pgs 187-192.
- [19] K. A. Remley, G. Koepke, C. Grosvenor, et. al., “NIST Tests of the Wireless Environment in Automobile Manufacturing Facilities.” NIST Technical Note 1550, October 2008.

- [20] S.A. Schulkunoff, H.T. Friis, *Antennas: Theory and Practice*. John Wiley and Sons, New York, 1952.

NIST Technical Publications

Periodical

Journal of Research of the National Institute of Standards and Technology—Reports NIST research and development in metrology and related fields of physical science, engineering, applied mathematics, statistics, biotechnology, and information technology. Papers cover a broad range of subjects, with major emphasis on measurement methodology and the basic technology underlying standardization. Also included from time to time are survey articles on topics closely related to the Institute's technical and scientific programs. Issued six times a year.

Nonperiodicals

Monographs—Major contributions to the technical literature on various subjects related to the Institute's scientific and technical activities.

Handbooks—Recommended codes of engineering and industrial practice (including safety codes) developed in cooperation with interested industries, professional organizations, and regulatory bodies.

Special Publications—Include proceedings of conferences sponsored by NIST, NIST annual reports, and other special publications appropriate to this grouping such as wall charts, pocket cards, and bibliographies.

National Standard Reference Data Series—Provides quantitative data on the physical and chemical properties of materials, compiled from the world's literature and critically evaluated. Developed under a worldwide program coordinated by NIST under the authority of the National Standard Data Act (Public Law 90-396). NOTE: The Journal of Physical and Chemical Reference Data (JPCRD) is published bimonthly for NIST by the American Institute of Physics (AIP). Subscription orders and renewals are available from AIP, P.O. Box 503284, St. Louis, MO 63150-3284.

Building Science Series—Disseminates technical information developed at the Institute on building materials, components, systems, and whole structures. The series presents research results, test methods, and performance criteria related to the structural and environmental functions and the durability and safety characteristics of building elements and systems.

Technical Notes—Studies or reports which are complete in themselves but restrictive in their treatment of a subject. Analogous to monographs but not so comprehensive in scope or definitive in treatment of the subject area. Often serve as a vehicle for final reports of work performed at NIST under the sponsorship of other government agencies.

Voluntary Product Standards—Developed under procedures published by the Department of Commerce in Part 10, Title 15, of the Code of Federal Regulations. The standards establish nationally recognized requirements for products, and provide all concerned interests with a basis for common understanding of the characteristics of the products. NIST administers this program in support of the efforts of private-sector standardizing organizations.

Order the following NIST publications—FIPS and NISTIRs—from the National Technical Information Service, Springfield, VA 22161.

Federal Information Processing Standards Publications (FIPS PUB)—Publications in this series collectively constitute the Federal Information Processing Standards Register. The Register serves as the official source of information in the Federal Government regarding standards issued by NIST pursuant to the Federal Property and Administrative Services Act of 1949 as amended, Public Law 89-306 (79 Stat. 1127), and as implemented by Executive Order 11717 (38 FR 12315, dated May 11, 1973) and Part 6 of Title 15 CFR (Code of Federal Regulations).

NIST Interagency or Internal Reports (NISTIR)—The series includes interim or final reports on work performed by NIST for outside sponsors (both government and nongovernment). In general, initial distribution is handled by the sponsor; public distribution is handled by sales through the National Technical Information Service, Springfield, VA 22161, in hard copy, electronic media, or microfiche form. NISTIR's may also report results of NIST projects of transitory or limited interest, including those that will be published subsequently in more comprehensive form.

U.S. Department of Commerce

National Institute of Standards and Technology
325 Broadway
Boulder, CO 80305-3337

Official Business

Penalty for Private Use \$300